

AN ABSTRACT OF THE THESIS OF

Arkady S. Grudzinsky for the degree of Master of Science in Electrical and Computer Engineering presented on September 16, 1999.

Title: Electro-Optical Characterization of SrS:Ce, SrS:Cu, and SrS:Cu,Ag  
Alternating-Current Thin-Film Electroluminescent Devices  
Redacted for Privacy

Abstract approved: \_\_\_\_\_

John F. Wager

The purpose of this thesis is to contribute to the understanding of SrS-based alternating-current thin-film electroluminescent (ACTFEL) device operation. Three main accomplishments serving this purpose are presented in this thesis. First, two new methods are developed for estimation of insulator capacitance in ACTFEL devices possessing a large amount of dynamic space charge. Both insulator capacitance estimation methods employ applied voltage waveforms with long pulses (e. g. rise time, pulse width, and fall time of 200  $\mu$ s). Second, SrS:Ce ACTFEL device capacitance – voltage ( $C - V$ ) and internal charge – phosphor field ( $Q_{int} - F_p$ ) characteristics are simulated using a two-sheet space charge model which assumes that phosphor space charge is localized at two planes parallel to the ACTFEL device phosphor-insulator interfaces. The two-sheet space charge model allows for realistic simulation of most charge and field parameters in a SrS:Ce ACTFEL device. However, in its present formulation, the two-sheet space charge model fails to explain the large experimentally observed phosphor field overshoot, turn-on voltage, and capacitance overshoot in SrS:Ce ACTFEL devices. Third, electro-optic characteristics of SrS:Ce, SrS:Cu, and SrS:Cu,Ag ACTFEL devices are compared. SrS:Ce (SrS:Cu,Ag) ACTFEL devices have the highest (lowest) luminance and luminous efficiency and are also the deepest green (blue); SrS:Cu ACTFEL devices are intermediate with regard to luminance, efficiency, and chromaticity. Space charge-related effects are observed in all of the ACTFEL devices studied. These effects are asymmetrical with respect to the applied voltage polarity. This asymmetry is more pronounced

in SrS:Ce ACTFEL devices and is consistent with more space charge generation occurring near the bottom, ITO phosphor-insulator interface when electron injection occurs from here. For SrS:Cu and SrS:Cu,Ag ACTFEL devices, it is found that the emission wavelength slightly decreases with increasing maximum applied voltage.

©Copyright by Arkady S. Grudzinsky

September 16, 1999

All Rights Reserved

Electro-Optical Characterization of SrS:Ce, SrS:Cu, and SrS:Cu,Ag  
Alternating-Current Thin-Film Electroluminescent Devices

by  
Arkady S. Grudzinsky

A THESIS  
submitted to  
Oregon State University

in partial fulfillment of the  
requirements for the degree of  
Master of Science

Completed September 16, 1999  
Commencement June 2000

Master of Science thesis of Arkady S. Grudzinsky presented on September 16, 1999

APPROVED:

Redacted for Privacy

Major Professor, representing Electrical and Computer Engineering

Redacted for Privacy

Head of Department of Electrical and Computer Engineering

Redacted for Privacy

Dean of Graduate School

I understand that my thesis will become part of the permanent collection of Oregon State University libraries. My signature below authorizes release of my thesis to any reader upon request.

Redacted for Privacy

Arkady S. Grudzinsky, Author

## ACKNOWLEDGEMENTS

I would like to thank professor John Wager for his support and advice during the course of the work leading up to the writing of this thesis, Paul Keir and John Hitt for helpful discussion of the results and constructive criticism, Sey-Shing Sun, Paul Keir, and Karl Barth for providing the ACTFEL device samples for the research, and Beau Baukol for assistance in measurements.

Furthermore, I would like to thank my wife Natalia and my father Sergei for their encouragement.

This work was supported by the Defense Advanced Research Projects Agency under contract MDA 972-94-C-0023 and under the Phosphor Technology Center of Excellence contract MDA 072-93-1-0030.

# TABLE OF CONTENTS

	<u>Page</u>
1 INTRODUCTION	1
2 LITERATURE REVIEW	3
2.1 ACTFEL device structure . . . . .	3
2.2 ACTFEL device operation . . . . .	5
2.2.1 Ideal ACTFEL device operation . . . . .	7
2.2.2 Phosphor space charge . . . . .	9
2.3 SrS properties . . . . .	12
2.4 SrS:Ce ACTFEL device properties . . . . .	14
2.5 SrS:Cu ACTFEL device properties . . . . .	18
2.6 SrS:Cu,Ag ACTFEL device properties . . . . .	21
2.7 The two-sheet space charge model . . . . .	23
2.7.1 Two-sheet space charge model quasi-statics . . . . .	25
2.7.2 Two-sheet space charge model dynamics . . . . .	26
2.7.3 Electron emission . . . . .	27
3 EXPERIMENTAL TECHNIQUE	30
3.1 Experimental setup . . . . .	30
3.2 ACTFEL device characterization methods . . . . .	32
3.2.1 External charge versus external voltage ( $Q-V$ ) ACTFEL device characteristics . . . . .	32
3.2.2 Dynamic capacitance versus external voltage ( $C-V$ ) ACTFEL device characteristics . . . . .	33
3.2.3 Internal charge versus phosphor field ( $Q_{int}-F_p$ ) ACT- FEL device characteristics . . . . .	34
3.2.4 Transient current ( $i(t)$ ) and transient luminance ( $b(t)$ ) ACTFEL device characteristics . . . . .	37
3.3 ACTFEL device sample preparation . . . . .	39
3.4 Design of experiment . . . . .	40

## TABLE OF CONTENTS (CONTINUED)

		<u>Page</u>
4	EXPERIMENTAL AND SIMULATION RESULTS	42
4.1	Estimation of the insulator capacitance for an ACTFEL device with dynamic space charge . . . . .	42
4.1.1	Static capacitance $C_i$ estimation . . . . .	43
4.1.2	Dynamic capacitance $C_i$ estimation . . . . .	45
4.1.3	Comparison of the two methods of insulator capacitance estimation . . . . .	49
4.1.4	Summary . . . . .	51
4.2	Simulation of electrical characteristics of SrS:Ce ACTFEL devices using a two-sheet space charge model . . . . .	52
4.2.1	Experimental procedure . . . . .	52
4.2.2	Results and discussion . . . . .	53
4.2.3	Summary . . . . .	60
4.3	Electro-optical characterization of SrS:Ce, SrS:Cu, and SrS:Cu,Ag ACTFEL devices . . . . .	62
4.3.1	$Q_{int} - F_p$ characteristics . . . . .	63
4.3.2	$C - V$ characteristics . . . . .	67
4.3.3	$Q_{max} - V_{max}$ characteristics . . . . .	70
4.3.4	$Q_{leak} - V_{max}$ , $Q_{pol} - V_{max}$ , and $Q_{relax} - V_{max}$ characteristics . . . . .	72
4.3.5	Optical characteristics . . . . .	75
4.3.6	Summary . . . . .	80
5	CONCLUSIONS AND RECOMMENDATIONS FOR FUTURE WORK	83
5.1	Estimation of the insulator capacitance for an ACTFEL device with dynamic space charge . . . . .	83
5.2	Simulation of electrical characteristics of SrS:Ce ACTFEL devices using a two-sheet space charge model . . . . .	84
5.3	Electro-optical characterization of SrS:Ce, SrS:Cu, and SrS:Cu, Ag ACTFEL devices . . . . .	85
	BIBLIOGRAPHY	87

## LIST OF FIGURES

<u>Figure</u>	<u>Page</u>
2.1. ACTFEL device structure. . . . .	4
2.2. AC driving waveform. . . . .	6
2.3. Cycle of energy band diagrams. The letters correspond to the points of the driving waveform (Fig. 2.2). . . . .	6
2.4. Energy band diagram of an ACTFEL device with positive phosphor space charge. . . . .	11
2.5. Schematic energy levels of (a) a free $\text{Cu}^+$ ion and (b) a $\text{Cu}^+$ ion in the crystal field with $O_h$ symmetry. The higher energy levels due to $3d^94p$ electronic configuration are not shown. Arrows show the absorption (excitation) and emission transitions. [1]	19
2.6. Two-sheet space charge model of an ACTFEL device. . . . .	25
2.7. The three field-assisted emission mechanisms. [2] . . . . .	28
3.1. Experimental setup for ACTFEL device characterization. . . . .	31
3.2. ACTFEL device $Q - V$ plot. . . . .	33
3.3. ACTFEL device $C - V$ plot. . . . .	34
3.4. ACTFEL device $Q_{int} - F_p$ plot. . . . .	36
3.5. ACTFEL device $i(t)$ plot. . . . .	38
4.1. Diagram of an ACTFEL device with continuous phosphor space charge distribution. . . . .	43
4.2. (a) Long voltage pulse waveform (curve 1) and external charge transient (curve 2), (b) luminance transient plot, (c) phosphor field transient plot calculated using the $C_i^{dyn}$ estimate, and (d) current transient plot for a SrS:Ce ACTFEL device. . . . .	46
4.3. (a) Long voltage pulse waveform (curve 1) and external charge transient (curve 2), (b) luminance transient plot, (c) phosphor field transient plot calculated using the $C_i^{stat}$ estimate, and (d) current transient plot for a SrS:Cu ACTFEL device. . . . .	50
4.4. Simulated (solid line) and experimental (dashed line) $Q_{int} - F_p$ (a) and $C - V$ (b, c) curves of SrS:Ce ACTFEL device. (b) – for positive, (c) – for negative applied voltage pulse. . . . .	58

## LIST OF FIGURES (CONTINUED)

<u>Figure</u>	<u>Page</u>
4.5. Experimental (a) and simulated (b) $C - V$ curves for SrS:Ce ACTFEL device at variable applied signal magnitude measured for a positive applied voltage pulse. 1 - $V_{max} = 140$ V, 2 - $V_{max} = 150$ V, 3 - $V_{max} = 157$ V. . . . .	59
4.6. Experimental (a) and simulated (b) $Q_{int} - F_p$ curves for SrS:Ce ACTFEL device at variable applied signal magnitude. 1 - $V_{max} = 140$ V, 2 - $V_{max} = 150$ V, 3 - $V_{max} = 157$ V. . . . .	61
4.7. Internal charge versus phosphor field plots for a SrS:Ce ACTFEL device at $V_{max} = V_{th} + 40$ V. (a) - using the "long"-pulse driving waveform, (b) - using the "short"-pulse driving waveform. . . . .	64
4.8. Internal charge versus phosphor field plots for a SrS:Cu ACTFEL device at $V_{max} = V_{th} + 40$ V. (a) - using the "long"-pulse driving waveform, (b) - using the "short"-pulse driving waveform. . . . .	66
4.9. Internal charge versus phosphor field plots for a SrS:Cu,Ag ACTFEL device at $V_{max} = V_{th} + 40$ V. (a) - using the "long"-pulse driving waveform, (b) - using the "short"-pulse driving waveform. . . . .	68
4.10. Capacitance versus applied voltage plots measured using a positive pulse of the "long"-pulse driving waveform with $V_{max} = V_{th} + 40$ V. (a) - for a SrS:Ce ACTFEL device, (b) - for a SrS:Cu ACTFEL device, (c) - for a SrS:Cu,Ag ACTFEL device. . . . .	69
4.11. Capacitance versus applied voltage plots measured using a negative pulse of the "long"-pulse driving waveform with $V_{max} = V_{th} + 40$ V. (a) - for a SrS:Ce ACTFEL device, (b) - for a SrS:Cu ACTFEL device, (c) - for a SrS:Cu,Ag ACTFEL device. . . . .	70
4.12. Maximum internal charge versus maximum applied voltage for a positive pulse of the "long"-pulse driving waveform. (a) - for a SrS:Ce ACTFEL device, (b) - for a SrS:Cu ACTFEL device, (c) - for a SrS:Cu,Ag ACTFEL device. . . . .	71

## LIST OF FIGURES (CONTINUED)

<u>Figure</u>	<u>Page</u>
4.13. External leakage charge versus maximum applied voltage for a positive pulse of the “long”-pulse driving waveform. (a) – for a SrS:Ce ACTFEL device, (b) – for a SrS:Cu ACTFEL device, (c) – for a SrS:Cu,Ag ACTFEL device. . . . .	72
4.14. External polarization charge versus maximum applied voltage for a positive pulse of the “long”-pulse driving waveform. (a) – for a SrS:Ce ACTFEL device, (b) – for a SrS:Cu ACTFEL device, (c) – for a SrS:Cu,Ag ACTFEL device. . . . .	73
4.15. External relaxation charge versus maximum applied voltage for a positive pulse of the “long”-pulse driving waveform. (a) – for a SrS:Ce ACTFEL device, (b) – for a SrS:Cu ACTFEL device, (c) – for a SrS:Cu,Ag ACTFEL device. . . . .	74
4.16. Luminance versus maximum applied voltage measured using the “long”-pulse driving waveform. (a) – for a SrS:Ce ACTFEL device, (b) – for a SrS:Cu ACTFEL device from Planar, (c) – for a SrS:Cu MOCVD device from SUNY, (d) – for a SrS:Cu,Ag ACTFEL device. . . . .	76
4.17. Luminous efficiency versus maximum applied voltage measured using the “long”-pulse driving waveform. (a) – for a SrS:Ce ACTFEL device, (b) – for a SrS:Cu ACTFEL device from Planar, (c) – for a SrS:Cu MOCVD device from SUNY, (d) – for a SrS:Cu,Ag ACTFEL device. . . . .	77
4.18. Normalized $Q_{max} - V_{max}$ (a), $L - V_{max}$ (b), and luminous efficiency (c) of a SrS:Ce ACTFEL device. . . . .	78
4.19. CIE coordinates of all of the SrS ACTFEL devices studied. (a) – for SrS:Ce ACTFEL devices, (b) – for sputtered SrS:Cu ACTFEL devices, (c) – for MOCVD SrS:Cu ACTFEL devices, (d) – for SrS:Cu,Ag ACTFEL devices. . . . .	79

## LIST OF TABLES

<u>Table</u>		<u>Page</u>
2.1.	Parameters of SrS . . . . .	12
4.1.	Summary of the insulator capacitance estimation . . . . .	49
4.2.	The device specifications for two-sheet space-charge modeling.	53
4.3.	Control factors for the two-sheet space charge model screening DOE. . . . .	54
4.4.	Response variables for the two-sheet space-charge model screening DOE. . . . .	54
4.5.	Results of the screening DOE. . . . .	55
4.6.	The optimized two-sheet space-charge simulation parameters.	57
4.7.	ACTFEL devices characterized . . . . .	63
4.8.	SrS:Ce, SrS:Cu, and SrS:Cu,Ag ACTFEL device characteristics . . . . .	81

# Electro-Optical Characterization of SrS:Ce, SrS:Cu, and SrS:Cu,Ag Alternating-Current Thin-Film Electroluminescent Devices

## Chapter 1 INTRODUCTION

Cathode-ray tube (CRT) technology, which has dominated the display industry in the past few decades, has some intrinsic drawbacks making it unsuitable for many new applications. In spite of the flat nature of the two-dimensional image, CRTs are inherently bulky devices since it is difficult to achieve a wide electron deflection angle. The wide electron deflection angle, however, makes it difficult to achieve flatness of the CRT screen without significant distortion of the image. These restrictions become more severe with large or miniature displays, which are necessary or desirable for many applications. Large energy consumption, complexity of the CRT technology, flickering of the screen, and the emission of electromagnetic radiation, which is damaging to humans, are other CRT drawbacks. These are some of the reasons why CRTs need to be replaced.

Recent progress in semiconductor and display technologies has resulted in alternatives to CRTs. Several flat panel display (FPD) technologies, categorized by the physical principle by which they produce an image, have been developed. All of these FPD technologies possess unique properties which are desirable for some applications, but unsuitable for others. The ability to manufacture 12–20 inch full-color liquid crystal displays (LCDs) has led to the domination of LCDs in the portable computer market. High luminance, high contrast, and a modest resolution of 32 dots per inch [3] of the plasma display panels (PDPs) make them most suitable for large area information screens and high-definition television (HDTV) applications. Leveraging off of the mature cathodoluminescent technology, field emission displays (FEDs) are expected to replace CRTs in the 2002–2005 time frame. [3] Finally, high spatial resolution, which is very difficult to achieve with other technologies, makes

electroluminescent (EL) displays an attractive choice for medical or industrial instruments, military equipment, and virtual reality systems, where compactness is vital. Other advantages of EL displays is their emissive nature (resulting in wide viewing angle), high luminance, and high contrast.

In spite of numerous advantages of EL technology over other FPD technologies, commercial full-color EL displays are not available yet, owing to the absence of an efficient blue phosphor. SrS:Ce, SrS:Cu, and SrS:Cu, Ag are considered to be the most promising materials for this purpose. However, the physical processes causing electroluminescence in these materials are only partially understood. The dynamic space charge formed in SrS EL phosphors distorts the electrical characteristic curves, making it difficult to determine important parameters of alternating-current thin-film electroluminescent (ACTFEL) devices. The mechanisms of space charge creation and its distribution inside the phosphor are not yet clearly understood. Thus, one of the main concerns of the research presented herein involves an investigation of these space charge issues which may lead to the development of an efficient blue EL phosphor and facilitate the creation of full-color EL displays.

The central focus of this thesis is the investigation of electro-optical characteristics of SrS:Ce, SrS:Cu, and SrS:Cu, Ag ACTFEL devices in order to establish the mechanisms causing electroluminescence and positive space charge creation in the phosphor layer.

This thesis consists of five chapters. Chapter 1 is the present introduction. Chapter 2 is a review of the pertinent literature covering the basics of ACTFEL device operation and reviewing previous work. Chapter 3 describes the samples measured and the experimental techniques applied in this research. Chapter 4 contains results and a discussion of these research results. Finally, Chapter 5 provides conclusions and recommendations for future work.

## Chapter 2

# LITERATURE REVIEW

This chapter describes ACTFEL device structure and operation and presents the two-sheet space charge model used for ACTFEL simulations. This chapter also contains a review of current literature on SrS:Ce, SrS:Cu, and SrS:Cu,Ag ACTFEL devices.

### 2.1 ACTFEL device structure

The basic structure of ACTFEL devices studied in this thesis was first reported in 1967. [4] As shown in Fig. 2.1, these devices consist of five layers stacked on a glass substrate. Light is produced by the phosphor layer sandwiched between two electrodes and insulated from them by two insulator layers. The bottom electrode is made of indium tin oxide (ITO), chosen for its transparency and good conductivity. The bottom insulator is made of aluminum titanium oxide (ATO), which is also transparent and has the advantage of possessing a relatively high dielectric constant and breakdown field. The phosphor layer in the first successful ACTFEL device was made of ZnS doped with Mn (ZnS:Mn) [5], which produces yellow light. As the need of blue EL phosphors arose, SrS:Ce and, recently, SrS:Cu and SrS:Cu,Ag attracted the attention of researchers [6, 7] as phosphor materials for ACTFEL devices. In this thesis devices with SrS:Ce, SrS:Cu, and SrS:Cu,Ag phosphors are studied. The top insulator in the devices studied in this thesis is made of either ATO or BTO (barium tantalate). Finally, the top electrode of an ACTFEL device is made of a metal, most commonly aluminum. For all measurements in this thesis, the bottom ITO electrode is connected to the ground through a sense capacitor and the external bias is applied to the top aluminum electrode.

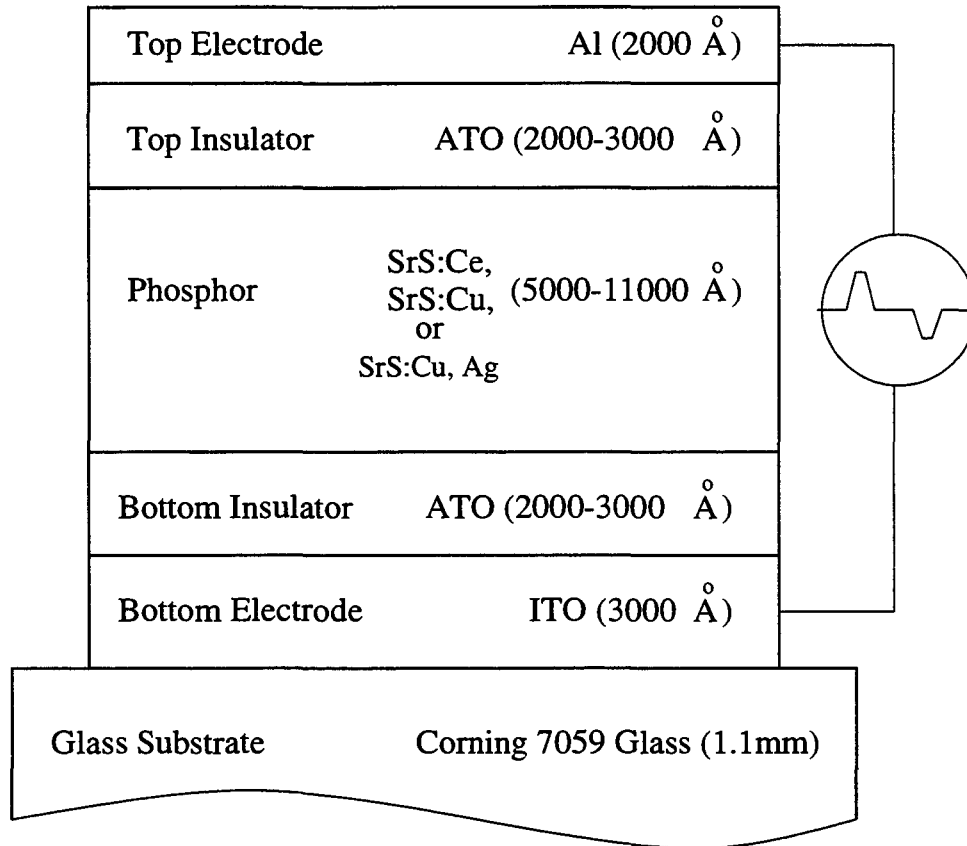


**Figure 2.1.** ACTFEL device structure.

## 2.2 ACTFEL device operation

ACTFEL device operation is based on the phenomenon of electroluminescence (EL), which transforms the energy of an electric field into light and was discovered in 1936 in ZnS powder phosphor. [8] The electric field, with a magnitude of 1–2 MV/cm, is created across the phosphor layer by an external alternating potential applied to the device electrodes. The light generated in the phosphor layer exits through the transparent bottom insulator, bottom electrode, and glass substrate.

The simplified model of ACTFEL device operation involves six primary processes. [9, 10] (Process 1) When the electric field inside the phosphor layer ( $f_p(t)$ ) is large enough, it causes injection of electrons from phosphor-insulator interface states into the conduction band of the phosphor. The mechanisms of this injection are discussed in Sec. 2.7.3. (Process 2) The injected electrons gain energy from the field and move across the phosphor layer. (Process 3) As these hot electrons move across the phosphor, a fraction of them excites centers of luminescence, transferring a part of their kinetic energy to the centers. (Process 4) The excited centers of luminescence relax to their ground states. If this relaxation is radiative, a photon is emitted by the center. Otherwise, the released potential energy of the excited center of luminescence is transferred into thermal energy of the host phosphor lattice by the emission of phonons. (Process 5) The electrons reach the anode phosphor-insulator interface and are trapped at interface states. (Process 6) Finally, the photons generated by the radiative relaxation of the excited centers of luminescence exit the phosphor layer through the transparent insulator-electrode-substrate stack and are observed by the viewer. This model of the device operation is considered to be *the ideal ACTFEL device model*.

Operation of real ACTFEL devices, however, is more complicated. Centers of luminescence can be complexes, involving luminescent impurities, charge compensators, and other defects in the phosphor crystal lattice. The excitation mechanism of these centers can involve band-to-band impact excitation of the host lattice and capture of electrons and/or holes produced by this excitation by the centers of lu-

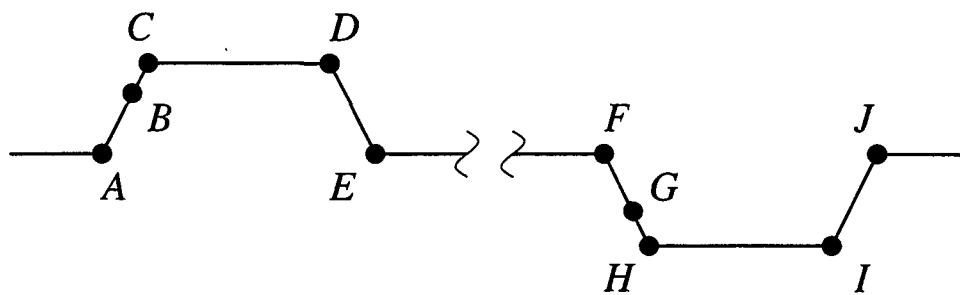


Figure 2.2. AC driving waveform.

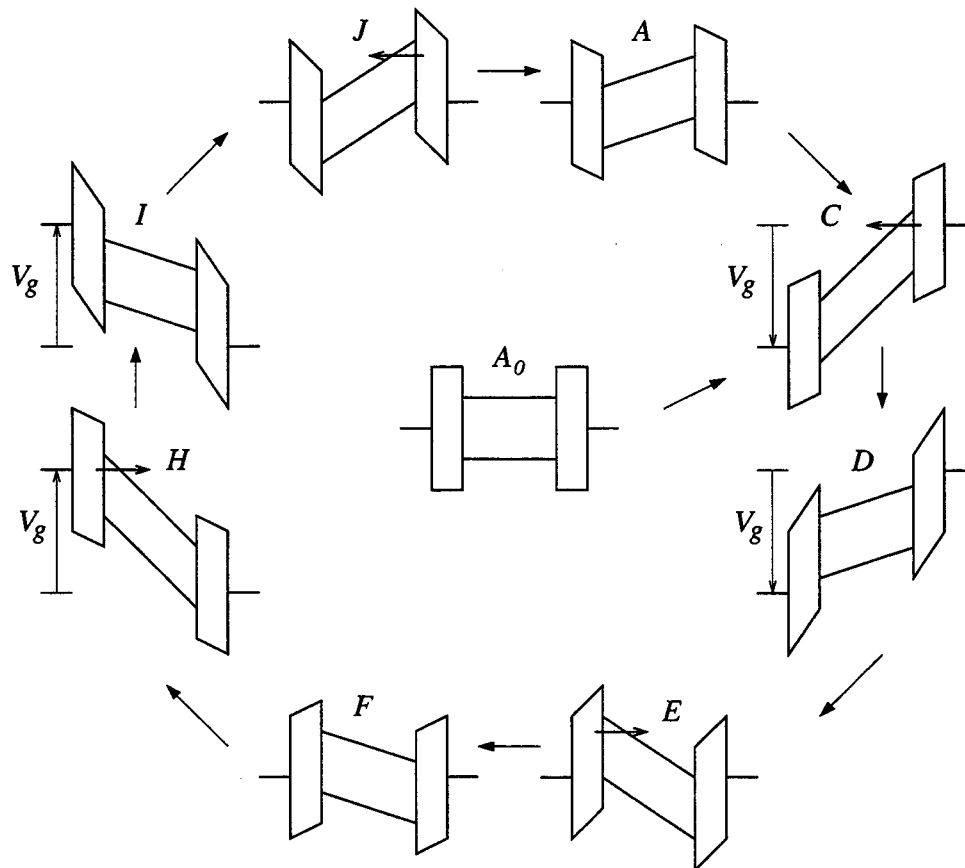


Figure 2.3. Cycle of energy band diagrams. The letters correspond to the points of the driving waveform (Fig. 2.2).

minescence. Furthermore, if an electron in an impurity center is excited to the phosphor conduction band, it can be driven by the field away from the center, leaving the center ionized. Both hole capture and impact ionization produce a positive charge distributed across the phosphor layer. Throughout this thesis, this positive charge distributed inside the phosphor layer is referred to as “*positive space charge*” or, simply, “*space charge*”. Space charge affects operation of an ACTFEL device and is discussed in more detail in Sec. 2.2.2.

### 2.2.1 Ideal ACTFEL device operation

A bipolar trapezoidal waveform (Fig. 2.2) is used in this research to drive the ACTFEL device. The bipolar trapezoidal waveform, compared to other AC waveforms, has the advantage of enhancing distinct separation of different regions of ACTFEL device operation. It consists of time portions, during which the applied voltage is either constant or changing linearly, which makes it easy to determine the dynamic device capacitance ( $dq(t)/dv(t)$ ). These time portions are marked in Fig. 2.2 by letters. Throughout this thesis the *AC* and *FH* portions are referred to as “*the rise time portions*”; *DE* and *IJ* portions are referred to as “*the fall time portions*”; *CD* and *HI* are referred to as “*the hold time portions*”; and, finally, *EF* and *JA* are called “*the interpulse pause*”. ACTFEL device operation can be visualized using energy band diagrams, which show the band gap of the insulator-phosphor-insulator sandwich and the Fermi-levels of the electrodes at different points of the driving waveform (Fig. 2.3).

Figure 2.3 *A<sub>0</sub>* shows the energy band diagram of an ideal ACTFEL device before the driving waveform is applied to the device. Figure 2.3 *C* shows the energy band diagram for the end of the rise time portion of the pulse (point *C*, Fig. 2.2), when the electric field created by the external bias is large enough to cause electron injection from the phosphor-insulator interface and the six processes described above take place in the device. Point *B* on the waveform (Fig. 2.2) marks the onset of electron injection. Two issues should be noted here. First, the field across the phosphor layer in this situation (Fig. 2.3 *C*) is larger than the field across the insulator layers,

owing to the larger dielectric constant of the insulators which causes the applied bias to drop mainly across the phosphor layer at this point. Second, the electrons transferred through the phosphor layer and trapped at the anode phosphor-insulator interface charge this interface negatively, while the cathode phosphor-insulator interface charges positively. The charge accumulated in this way at the phosphor-insulator interfaces decreases the field across the phosphor layer and increases the field across the insulator layers. Figure 2.3 *D* shows the energy band diagram at the end of the hold time portion of the pulse (point *D*, Fig. 2.2), when the transferred charge accumulated at the phosphor-insulator interfaces decreases the phosphor field so much that it is no longer sufficient to cause the electron injection. Although the applied bias is still the same as at the beginning of the hold time portion of the pulse, most of this bias now drops across the insulator layers. This situation arises for sufficiently long hold times of the driving waveform. Figure 2.3 *E* shows the energy band diagram for the end of the driving pulse (point *E*, Fig. 2.2), when the external bias is removed and the charge accumulated at the phosphor-insulator interfaces creates an electric field across the phosphor layer opposite to the field previously created by the external bias. This field may be sufficient to cause electron injection from the anode phosphor-insulator interface states back into the phosphor conduction band. Throughout this thesis such electron injection is referred to as “*the back injection of electrons*”. It should be noted, that the field sufficient to cause the back injection of electrons is smaller than the turn-on field required to cause injection of electrons from the cathode phosphor-insulator interface at the beginning of the driving pulse, since at the end of the driving pulse the anode interface states are filled with electrons transferred through the phosphor layer during the driving pulse. Finally, Fig. 2.3 *F* shows the energy band diagram for the beginning of the next driving pulse of the opposite polarity (point *F*, Fig. 2.2). If the interpulse pause is sufficiently long, the phosphor field relaxes during the interpulse pause so much that the back injection of electrons stops and by the beginning of the next driving pulse, a stable situation as shown in Fig. 2.3 *F* arises.

Several definitions are required here. The charge at the phosphor-insulator interfaces at the beginning of a driving pulse, residual from the previous driving pulse, is usually called “*the polarization charge*” ( $Q_{int}^{pol}$ ). The phosphor field created by the polarization charge assists the field created by the oncoming driving pulse, reducing the external bias sufficiently to create the turn-on phosphor field (the phosphor field, at which the injection of electrons starts). The minimum external bias sufficient for the onset of electron injection, which is achieved during the rise time portion of the driving waveform is called “*the turn-on voltage*” ( $V_{to}$ ). The turn-on voltage should be distinguished from “*the threshold voltage*” ( $V_{th}$ ), which designates the minimum magnitude of the driving waveform, at which electron injection takes place. When the device is off and the magnitude of the external bias is being increased to turn the device on, the electric field created by the external bias is not yet assisted by the field created by  $Q_{int}^{pol}$ . Thus,  $V_{th}$  is always larger than  $V_{to}$ .

Figures 2.3 *H* through *A* repeat Figs. 2.3 *C* through *F* for the driving pulse of the opposite polarity, completing the cycle. All the charges and all the fields shown in Figs. 2.3 *H* through *A* have opposite polarity to those shown in Figs. 2.3 *C* through *F*.

## 2.2.2 Phosphor space charge

Some phenomena in ACTFEL devices cannot be explained by the ideal device model. Attempts to explain luminance – voltage ( $L - V_{max}$ ) hysteresis [11, 12, 13], negative differential resistance [14], internal charge – phosphor field ( $Q_{int} - F_p$ ) overshoot [15, 16, 17], and capacitance-voltage overshoot [15, 17] in ACTFEL devices lead to a conclusion [11, 18] that the electric field inside the phosphor layer depends on both spatial coordinates and time, while the ideal ACTFEL device model assumes that the electric field is constant at any point in the phosphor layer. Phosphor field dependence on spatial coordinates implies the presence of a space charge distributed across the phosphor layer.

Different researchers [19, 15, 20, 21, 11, 18, 22, 14, 23, 24, 2] mention three main mechanisms of phosphor space charge creation in ACTFEL devices. The first

mechanism involves capturing holes generated by band-to-band impact excitation by impurity centers. [14, 23, 24] The second mechanism is impact ionization of deep-level bulk traps. It is believed to require less energy than band-to-band impact excitation. [11] The third mechanism is field emission from interface traps, similar to field emission from interface traps. It is thought to play an important role in phosphor space charge generation [2] owing to the decreased probability of hole capturing at high electric fields. [25] The involvement of a specific space charge generation mechanism in a specific ACTFEL device depends on the location of the impurity energy levels with respect to the phosphor energy bands, i. e. on the impurity and phosphor type, and on the symmetry and environment of the impurity centers in the phosphor crystal lattice. The dominant mechanisms of space charge creation are expected to be unique to specific phosphor dopants and host lattices and have not been clearly established yet.

The existence of positive space charge in the phosphor layer has a great effect on ACTFEL device operation. In energy band diagrams, the presence of positive phosphor space charge is indicated by “bent” energy bands of the phosphor (Fig. 2.4). As indicated by the slope of the energy bands, the phosphor field near the cathode phosphor-insulator interface is increased and strongly decreased near the anode phosphor-insulator interface (Fig. 2.4). An enhanced phosphor field near the cathode phosphor-insulator interface facilitates electron injection from cathode interface traps into the phosphor conduction band and gives them more kinetic energy, making space charge generation even more efficient. A decreased phosphor field near the anode phosphor-insulator interface slows down hot electrons, reduces damage of the anode phosphor-insulator interface and improves the aging characteristics of the device. These effects show themselves in  $C - V$ ,  $i(t)$ ,  $Q - V$ ,  $Q_{int} - F_p$  and  $Q_{max} - V_{max}$  curves of an ACTFEL device.

Depending on the way the phosphor space charge manifests itself in the measurements, it can be called “*static*” or “*dynamic*”. Static space charge is the steady-state space charge present during the application of a periodic applied voltage waveform and has a spatial distribution which depends on  $V_{max}$ . Thus, the static space charge

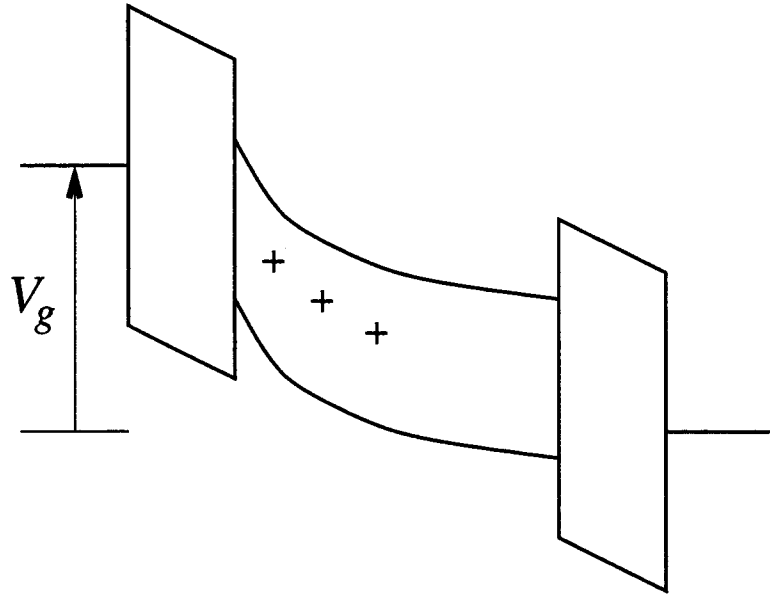


**Figure 2.4.** Energy band diagram of an ACTFEL device with positive phosphor space charge.

can be detected by measurements involving  $V_{max}$  variation (e. g.  $Q_{max} - V_{max}$  and  $dQ_{max}/dV_{max}$ ) and is not readily evident in measurements carried out at fixed  $V_{max}$  (e. g.  $C - V$ ,  $Q - V$ ,  $Q_{int} - F_p$ ,  $i(t)$ , and  $b(t)$ ). Dynamic space charge is created near the cathode phosphor-insulator interface and annihilated near the anode phosphor-insulator interface every time the polarity of the externally applied bias switches.

It should be noted that the terms “static space charge” and “dynamic space charge” may refer to space charge of the same origin and physical nature. These terms refer to the way the space charge affects the ACTFEL device operation rather than to the physical nature of the space charge. Some devices exhibiting static space charge exhibit no dynamic space charge effects, but devices exhibiting dynamic space charge effects usually exhibit static space charge as well.

**Table 2.1.** Parameters of SrS

Lattice constant	Å	5.68	[26]
Radial sum	Å	2.84	[26]
Average anionic ( $S^{2-}$ ) radius	Å	1.02	[26]
Average cationic ( $Sr^{2+}$ ) radius	Å	1.18	[26]
Density of cations or anions	$cm^{-3}$	$2.18 \times 10^{22}$	
Ionicity		0.8 – 0.9	[26]
Dielectric constant		9.4	[26]
Band gap	eV	4.32	[27]

### 2.3 SrS properties

Strontium sulfide (SrS) belongs to the family of alkaline earth sulfides (AES) comprising sulfides of the group IIa alkaline earth metals, Mg, Ca, Sr, and Ba. All alkaline earth sulfides have the rocksalt structure [26], the same as the structure of NaCl. The unit cell of the NaCl structure is face-centered cubic with each ion coordinated by six equidistant nearest-neighbor ions of opposite polarity. Since these neighbor ions are at the corners of a regular octahedron, this crystal structure is said to involve octahedral coordination. Table 2.1 gives some crystal and ionic parameters of SrS. The ionic radii of certain rare earth ions (1.11 Å for  $Ce^{3+}$  and 1.12 Å for  $Eu^{2+}$  [26]) are very close to those of SrS cations (Table 2.1). Therefore, rare earth luminescent centers are considered to be effectively incorporated into the SrS lattice.

The SrS band structure has been studied by many researchers. [28, 27, 29] There has been discussion in the literature as to whether the SrS band gap is direct or indirect. Kaneko et al. [27] have interpreted their experimental reflectivity measurements on the basis of a self-consistent augmented-plane-wave (APW) band-structure calculation, [28] concluding that SrS is an indirect-band-gap material. Pandey et al. [29] argues against this interpretation, saying that SrS is a direct-band-gap material,

as follows from calculations using the Hartree-Fock method. Ghosh [26] supports the conclusion of Pandey et al. [29] noticing that the Hartree-Fock method is more appropriate than the APW method for the calculation of band structure of ionic materials, such as SrS. More recent exact exchange-local density approximation calculations [30] show SrS to have an indirect bandgap. Thus, the latest analysis shows that SrS is, most probably, an indirect-band-gap material.

The process of ionic impurity incorporation and charge compensation in predominantly ionic bonded AES lattices [26] is significantly different from that in covalently bonded group IV semiconductors. For example, when a neutral group V dopant is added into silicon or germanium (group IV), charge neutrality is maintained by promotion of an electron to the conduction band, leaving behind a positively charged dopant atom. However, in a predominantly ionic lattice, such as SrS, Sr cations and S anions are held together by Coulomb attraction. When the valence of a substitutional dopant ion is different from the valence of the ion being substituted, the simultaneous incorporation of a counterbalancing defect is required to maintain charge neutrality. For example, a  $\text{Ce}^{3+}$  ion substituting for  $\text{Sr}^{2+}$  in SrS lattice which has a net positive charge,  $[\text{Ce}_{\text{Sr}}^{3+}]^+$ , will need another defect having a net negative charge. This compensator defect can be formed, for example, by a  $\text{Na}^+$  ion on a Sr site,  $[\text{Na}_{\text{Sr}}^+]^-$ , or by a strontium vacancy,  $[\text{V}_{\text{Sr}}]^{2-}$ , and another  $[\text{Ce}_{\text{Sr}}^{3+}]^+$  or a  $[\text{Cl}_{\text{S}}^-]^+$  ion combined in a  $[\text{Ce}_{\text{Sr}}^{3+}\text{V}_{\text{Sr}}]^-$  or a  $[\text{Cl}_{\text{S}}^-\text{V}_{\text{Sr}}]^-$  defect complex, respectively. Similarly, group I elements, such as Ag and Cu, forming respectively  $[\text{Cu}_{\text{Sr}}^+]^-$  and  $[\text{Ag}_{\text{Sr}}^+]^-$  centers in SrS, can be compensated, for example, by a  $[\text{Cu}_{\text{Sr}}^+\text{V}_{\text{S}}]^+$ ,  $[\text{Cl}_{\text{S}}^-]^+$ , or  $[\text{Y}_{\text{Sr}}^{3+}]^+$  defect. Charge compensation in SrS and other AES is similar to that in conventional II-VI compounds, such as ZnS. However, since AES are more ionic than conventional II-VI compounds, intrinsic point defects to compensate for the charges of the incorporated impurities are more readily created in AES than in conventional II-VI compounds. [26] This may be one of the reasons why SrS-based ACTFEL devices exhibit much more phosphor space charge than ZnS:Mn ACTFEL devices.

Electron and hole traps play an important role in ACTFEL device operation. Density and energy depth of interface traps affects injection of electrons into the

phosphor conduction band; and presence of bulk traps in the phosphor affects both the space charge creation and the electron injection. A study of trapping states in CaS and SrS single crystals, films, and powders was reported by Rennie et al. [31] using the technique of transient thermoluminescence (TTL). To obtain a TTL curve, the sample is irradiated with a UV light chopped using a shutter. The photoluminescence transient is monitored using an oscilloscope. The normalized transient intensity,  $I_s/I_0$  (where  $I_s$  is the luminous intensity at a sampling time  $t_s$ , and  $I_0$  is the luminous intensity at time  $t_0$  when the exciting UV light is shut off by the shutter), is recorded as a function of temperature. Rennie et al. [31] have found in SrS traps  $< 0.2$  and  $0.56$  eV deep possibly produced by surface defects, traps  $0.71$  eV deep possibly produced by natural bulk defects, and traps  $0.48$  eV deep possibly produced by  $\text{Ce}^{3+}$  impurities. It is noted in [31] that in SrS and CaS thin films, the low-temperature peaks dominate in TTL spectra which implies that the traps prevailing in SrS thin films are shallow. The mid and high temperature peaks observed in TTL spectra of crystals and powders are completely masked by these low-temperature peaks in SrS and CaS thin-film TTL spectra. These low-temperature TTL peaks are not due to any impurity-related defects. Most probably, these low-temperature TTL peaks are caused by surface defects, in which the thin films are expected to be particularly rich.

Now consider the properties SrS doped with Ce, Cu, and Ag impurities.

## 2.4 SrS:Ce ACTFEL device properties

SrS:Ce has proven to be a promising blue phosphor for full-color ACTFEL displays. [6] The blue-green luminescence is caused by electron transitions from the lowest excited state  $^2T_{2g}(5d)$  to the  $4f$  ground state of  $\text{Ce}^{3+}$ . [32, 33] Two emission bands with maxima at approximately  $525$  and  $480$  nm are observed in the luminescence spectrum, originating from a splitting of the  $4f$  ground state into  $^2F_{7/2}$  and  $^2F_{5/2}$ . The transitions in  $\text{Ce}^{3+}$  are parity allowed, which aids in the attainment of high radiative efficiency. Both in SrS:Ce powders and thin films, the wavelength of

$\text{Ce}^{3+}$  luminescence can increase when the symmetry of  $\text{Ce}^{3+}$  centers is lowered. A lower symmetry crystal field lowers the energy of the lowest  $\text{Ce}^{3+}$  excited state ( $5d$ ) component from which the emission originates. [34]

To understand the reasons for the lowering of the symmetry of  $\text{Ce}^{3+}$  centers in SrS:Ce, consider the environment of  $\text{Ce}^{3+}$  ions in a SrS lattice. It has been found by electron paramagnetic resonance (EPR) measurements [35] that in SrS:Ce powders,  $\text{Ce}^{3+}$  ions substitute for  $\text{Sr}^{2+}$  ions in the SrS host lattice, forming  $[\text{Ce}_{\text{Sr}}^{3+}]^+$  centers on the cation site with cubic symmetry.  $[\text{Ce}_{\text{Sr}}^{3+}]^+$  centers are singly positively charged with respect to the Sr cation host site, which is consistent with Ce acting as a donor in SrS. To maintain charge neutrality, a charge compensator needs to be present to compensate  $[\text{Ce}_{\text{Sr}}^{3+}]^+$ . The most likely intrinsic charge compensator for  $[\text{Ce}_{\text{Sr}}^{3+}]^+$  is a Sr vacancy. A Sr vacancy in the SrS lattice is a double acceptor when fully ionized and is denoted as  $[\text{V}_{\text{Sr}}]^{2-}$ . It is shown by EPR in [34] that in SrS:Ce powders and thin films half of the  $[\text{Ce}_{\text{Sr}}^{3+}]^+$  centers are associated with a nearby Sr vacancy to form a  $[\text{Ce}_{\text{Sr}}^{3+}\text{V}_{\text{Sr}}]^-$  defect complex and the other half of the  $[\text{Ce}_{\text{Sr}}^{3+}]^+$  centers remain isolated; thus, one  $[\text{V}_{\text{Sr}}]^{2-}$  compensates two  $[\text{Ce}_{\text{Sr}}^{3+}]^+$ 's. When a Sr vacancy complexes with a  $[\text{Ce}_{\text{Sr}}^{3+}]^+$  center, the symmetry of the  $[\text{Ce}_{\text{Sr}}^{3+}]^+$  center in the complex is lowered to axial symmetry. The presence of these  $[\text{Ce}_{\text{Sr}}^{3+}]^+$  centers with axial symmetry in SrS:Ce powders and thin films is detected by EPR. [34] Thus, charge compensation is responsible for the formation of  $[\text{Ce}_{\text{Sr}}^{3+}\text{V}_{\text{Sr}}]^-$  complexes of lower symmetry and longer luminescence wavelength compared to isolated  $[\text{Ce}_{\text{Sr}}^{3+}]^+$  centers in SrS:Ce powders and thin films. In SrS:Ce thin films, the cubic symmetry of isolated  $[\text{Ce}_{\text{Sr}}^{3+}]^+$  centers can be also lowered by deformation of the film crystal lattice, which depends on the film growth conditions and the material of the substrate. [35] In general, the blue chromaticity of a SrS:Ce thin film phosphor can be improved by increasing the number of  $[\text{Ce}_{\text{Sr}}^{3+}]^+$  centers with cubic symmetry. This can be achieved by improving the crystallinity of the film or by introducing alternative charge compensators by co-doping to avoid the formation of  $[\text{V}_{\text{Sr}}]^{2-}$ .

Energy transfer between  $[\text{Ce}_{\text{Sr}}^{3+}]^+$  centers and the SrS lattice appears to play a significant role in SrS:Ce ACTFEL device operation. This conclusion is reached in

[32] by analysis of photoluminescence excitation (PLE) spectra of SrS:Ce thin films. To obtain a PLE spectrum of a SrS:Ce thin film, the luminance monitored at one of the  $\text{Ce}^{3+}$  emission maxima (e. g. 480 nm) is plotted against the wavelength of the exciting light which is varied during the PLE experiment. The PLE experiment shows that  $\text{Ce}^{3+}$  photoluminescence (PL) in SrS:Ce thin films is mostly produced by band-to-band excitation (250 nm) of the SrS host lattice and only a small fraction of the  $\text{Ce}^{3+}$  luminescence is produced by direct excitation of  $[\text{Ce}_{\text{Sr}}^{3+}]^+$  centers (430 nm). This result implies that the energy of the electron-hole pairs excited by band-to-band excitation is transferred to Ce centers, resulting in luminescence. It is assumed [32] that the energy transfer between  $[\text{Ce}_{\text{Sr}}^{3+}]^+$  and the host lattice involves interaction of  $[\text{Ce}_{\text{Sr}}^{3+}]^+$  centers with Sr vacancies and other lattice imperfections. The centers formed by lattice imperfections can store part of the energy released from recombining electron-hole pairs and then slowly transfer the stored energy to  $\text{Ce}^{3+}$  centers, resulting in a long-time-constant PL decay (afterglow) which is observed experimentally. [32]

Consider the effect of the electric field on electronic processes in SrS:Ce. The electric field can affect the SrS:Ce ACTFEL device operation in several ways. First, as electron-hole pairs are created by band-to-band impact ionization, the electric field can drive the electrons to the interfaces while holes are efficiently trapped, creating space charge. Second, the electric field assists electron tunneling from excited  $\text{Ce}^{3+}$  centers into the SrS conduction band, leaving the Ce center ionized. Ce ionization has a two-fold effect of creating space charge and reducing the probability of radiative relaxation of the excited  $[\text{Ce}_{\text{Sr}}^{3+}]^+$  center. This conclusion is supported by measurement of the internal charge in a SrS:Ce ACTFEL device at subthreshold applied voltages under irradiation with 430 nm light, corresponding to the  $\text{Ce}^{3+}$  excitation maximum. [32] This measurement shows that as the applied voltage increases, the charge transferred across the phosphor increases and the device photoluminescence decreases, implying that even a small field carries electrons away from excited  $\text{Ce}^{3+}$  centers. Third, the electric field reduces the probability of electron capture by an ionized Ce center and subsequent radiative relaxation of the center. Thus, two main

effects of the electric field on SrS:Ce ACTFEL device operation are the reduction of the probability of radiative relaxation of  $\text{Ce}^{3+}$  centers and the creation of the space charge.

Space charge enhances the phosphor field near the cathode phosphor-insulator interface and decreases the phosphor field near the anode phosphor-insulator interface (Sec. 2.2.2). Many researchers [36, 37, 38, 39] consider the anode phosphor field to be close to zero. Taking into account the conclusion of the previous paragraph, it is expected that most of the radiative recombination takes place in the low-field anode phosphor region and most of the space charge creation takes place in the high-field cathode phosphor region. This conclusion is supported by transient luminance measurements of an ACTFEL device with SrS:Ce–SrS:Eu double phosphor layer. [40] When the applied voltage polarity is such that SrS:Ce layer is on the anode side of the phosphor, the blue-green SrS:Ce emission dominates over the red emission of SrS:Eu. For the opposite polarity voltage pulse, when the SrS:Eu layer is the anode, the red emission of SrS:Eu dominates over SrS:Ce blue-green emission.

It is still unclear, which centers are responsible for space charge creation in SrS:Ce ACTFEL devices. Results of [39] and [41] suggest that about half of the space charge originates from  $\text{Ce}^{3+}$  ionization. The remaining half of the space charge is attributed to the ionization of other SrS lattice imperfections. It is suggested in [41] that only a small fraction ( $\sim 0.01\%$ ) of the Ce centers in SrS:Ce are ionized during the ACTFEL device operation. The average space charge density across the phosphor layer is estimated to be  $9.0 \text{ mC/cm}^3$ . [37] This charge density corresponds to the trap density of  $5.6 \times 10^{16} \text{ cm}^{-3}$ . Note that the local space charge density may exceed that of the average since the space charge distribution is expected to vary across the phosphor layer.

Other effects of space charge on SrS:Ce ACTFEL device operation include current transient, capacitance, and phosphor field overshoot, and trailing-edge emission. The current transient and capacitance overshoots are observed during the leading edge of the applied voltage pulse right after the applied voltage,  $v_g(t)$ , becomes larger than the turn-on voltage,  $V_{to}$ . The current transient and capacitance overshoots are

caused by multiplication of free carriers in the SrS:Ce phosphor due to band-to-band impact ionization and hole trapping or trap-to-band impact ionization, which are accompanied by space charge creation. [37] This carrier multiplication increases the charge transferred across the phosphor layer and drops the average phosphor field from 1.3 MV/cm to 0.7 MV/cm [36] leading to phosphor field overshoot. The trailing-edge emission observed in SrS:Ce ACTFEL devices during the applied voltage fall time [42, 43, 39] is also suggested to be a space-charge effect. Since the anode phosphor field is assumed to be small in SrS:Ce ACTFEL devices [36, 37, 38, 39], when the applied voltage decreases from its maximum value, the local field at the anode phosphor-insulator interface may reverse its polarity, causing injection of electrons from shallow traps followed by radiative recombination with ionized Ce centers. This process is invoked to explain trailing-edge emission in SrS:Ce ACTFEL devices.

Although the efficiency of the SrS:Ce phosphor is very good, the chromaticity of SrS:Ce emission is not pure enough for use of SrS:Ce as a blue phosphor in full-color displays. To achieve a true blue color with SrS:Ce, a filter must be used, and the filtered efficiency of SrS:Ce is greatly reduced. This has motivated researchers to look for efficient EL phosphors with better blue color purity.

## 2.5 SrS:Cu ACTFEL device properties

The first blue-emitting SrS:Cu ACTFEL device was reported by Kane et al. in 1985. [44] However, the luminance of Kane's SrS:Cu ACTFEL device was very poor. After Sun et al. reported the development of a much improved SrS:Cu ACTFEL device [45], with a luminance 30 times higher than that of Kane's device, many researchers have focused their efforts on fabricating and characterizing SrS:Cu ACTFEL devices.

SrS:Cu luminescence has better chromaticity for a blue phosphor in EL applications compared to SrS:Ce luminescence. The PL spectrum of SrS:Cu powders with small Cu concentration has a peak at  $\sim 480$  nm at room temperature. [1, 46] This PL peak is caused by a  $3d^94s(^3E_g) - 3d^{10}(^1A_{1g})$  transition (Fig. 2.5) of the  $\text{Cu}^+$  isolated ions in  $O_h$  symmetry crystal environment.

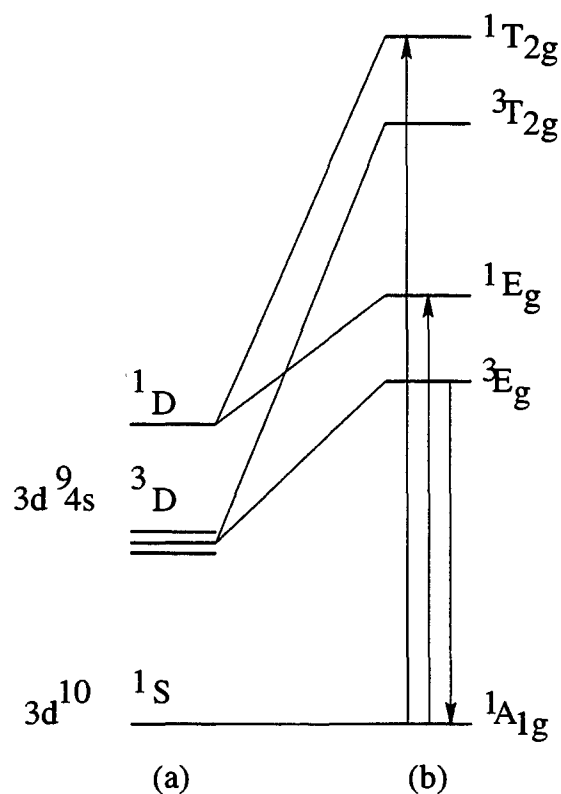


**Figure 2.5.** Schematic energy levels of (a) a free Cu<sup>+</sup> ion and (b) a Cu<sup>+</sup> ion in the crystal field with  $O_h$  symmetry. The higher energy levels due to  $3d^9 4p$  electronic configuration are not shown. Arrows show the absorption (excitation) and emission transitions. [1]

The  $3d^{10} - 3d^9 4s$  electronic transitions are parity- and J-forbidden in the free Cu<sup>+</sup> ion. In a SrS lattice, the selection rules forbidding the transitions are relaxed by several factors. The first factor is electron-lattice interactions which make the  $3d^{10} - 3d^9 4s$  transition in Cu<sup>+</sup> ions partially allowed. The second factor is the off-center position of Cu<sup>+</sup> ions which relaxes the forbidding selection rules of the inversion symmetry by lowering the symmetry of the Cu<sup>+</sup> centers. The “off-center” position of Cu<sup>+</sup> ions refers to the shift of Cu<sup>+</sup> ions substituting for Sr in SrS lattice from the exact Sr position. The off-center position of Cu<sup>+</sup> in SrS lattice is possible because Cu<sup>+</sup> ions (ionic radius 0.77 Å [1]) are significantly smaller than Sr<sup>2+</sup> ions (ionic radius 1.18 Å [1]) and have space available to be loosely bound on the cation site. The third factor relaxing the parity selection rules is the presence of charge

compensating sulfur vacancies,  $[V_S]^{2+}$ , in SrS:Cu which are Coulombically attracted to the  $[\text{Cu}_{\text{Sr}}^+]^-$  centers. Sulfur vacancies facilitate the off-center  $\text{Cu}^+$  position and completely relax the parity selection rules by eliminating the inversion symmetry of the  $[\text{Cu}_{\text{Sr}}^+]^-$  center.

The wavelength of  $\text{Cu}^+$  luminescence in SrS:Cu depends on the Cu concentration, co-dopants, and temperature. [46, 47] Li suggests that blue luminescence in SrS:Cu (480 nm at room temperature) is produced by  $[\text{Cu}_{\text{Sr}}^+]^-$  centers with coordination number 6, and green luminescence ( $> 500$  nm) is produced by  $[\text{Cu}_{\text{Sr}}^+]^-$  centers with coordination number 5. [47] The coordination number refers to the number of  $\text{S}^{2-}$  ions closest to the  $\text{Cu}^+$  ion. Coordination number 5 implies that there is a sulfur vacancy near the  $[\text{Cu}_{\text{Sr}}^+]^-$  center, which lowers the symmetry of the  $\text{Cu}^+$  center and increases the wavelength of  $\text{Cu}^+$  luminescence. Increasing the Cu concentration and co-doping with monovalent alkali ions (e. g.  $\text{Na}^+$ ) promote creation of  $[V_S]^{2+}$  in SrS, thus increasing the wavelength of  $\text{Cu}^+$  luminescence. Co-doping of SrS:Cu with trivalent rare-earth ions (e. g.  $\text{Y}^{3+}$ ) reduces the number of  $[V_S]^{2+}$  in SrS, because the trivalent donor co-dopants compensate  $[\text{Cu}_{\text{Sr}}^+]^-$  charge, thus decreasing the wavelength of  $\text{Cu}^+$  luminescence. This is the reason why SrS:Cu phosphors with large Cu concentrations or co-doped with monovalent ions emit green light, while SrS:Cu phosphors with small Cu concentrations or co-doped with trivalent donor ions emit blue light. [46, 47] In order to improve the blue chromaticity of the SrS:Cu phosphor, the number of  $[\text{Cu}_{\text{Sr}}^+]^-$  centers with coordination number 6 should be increased compared to the number of  $[\text{Cu}_{\text{Sr}}^+]^-$  centers with coordination number 5. This can be achieved by co-doping SrS:Cu with trivalent donors (e. g.  $\text{Y}^{3+}$ ) which eliminate  $[V_S]^{2+}$  as charge compensators for  $[\text{Cu}_{\text{Sr}}^+]^-$  centers. [47]

As the temperature decreases from room temperature to 80 K, the wavelength of SrS:Cu luminescence increases from 480 nm to 513 nm. The temperature dependence of the SrS:Cu luminescence wavelength can be explained as follows. SrS:Cu luminescence is a superposition of emission from  $[\text{Cu}_{\text{Sr}}^+]^-$  centers with coordination number 5 and 6. At low temperature, the electron-lattice interaction, relaxing the parity selection rules for blue  $\text{Cu}^+$  emission, is weak. This is the reason why at low

temperatures, the blue component of the SrS:Cu luminescence is small. The green component of the SrS:Cu luminescence is not affected by the temperature. Therefore, at low temperatures, the SrS:Cu luminescence spectrum is dominated by the green component.

PLE spectra for SrS:Cu powders contain two main peaks at 283 nm (4.36 eV) and 310 nm (3.98 eV). [46] These PLE spectra are obtained by monitoring the 513 nm PL at 80 K as a function of the exciting light variable wavelength. The 283 nm excitation maximum is ascribed to the  $^1A_{1g} - ^1T_{2g}$  transition and the 310 nm excitation maximum is ascribed to the  $^1A_{1g} - ^1E_g$  transition in  $\text{Cu}^+$  centers (Fig. 2.5). Note that the excitation energy for these transitions in  $\text{Cu}^+$  ions is comparable to the SrS band gap (4.3 eV). The mechanism of  $\text{Cu}^+$  excitation in SrS:Cu ACTFEL devices deserves a detailed study. PLE spectra of SrS:Cu powders with large Cu concentrations, obtained by monitoring the PL at 540–570 nm, contain three additional long-wavelength bands, not observed in the PLE spectrum of SrS:Cu powders with small Cu concentrations. [46] It has been suggested that these long-wave excitation bands correspond to the excitation energy of complex defects involving  $\text{Cu}^+$  aggregates [46] and  $\text{Cu}^+$  centers associated with other lattice defects. [47]

## 2.6 SrS:Cu,Ag ACTFEL device properties

Silver impurity centers are known to create blue luminescence in alkali halide crystals. [48, 49] Recently, silver has attracted the attention of many researchers as an impurity that may produce efficient blue luminescence in SrS. [50, 51, 52, 53]

$\text{Ag}^+$  ions have a  $5d^{10}$  electronic configuration which makes them similar to  $\text{Cu}^+$  ions having a  $4d^{10}$  electronic configuration. PL and EL spectra of SrS:Ag thin films have two peaks at  $T < 200$  K. [51] The first emission peak is in the UV spectral region at  $\lambda = 360$  nm. The second emission peak is in the blue spectral region at  $\lambda = 420 - 430$  nm. Most probably, the UV emission peak is caused by isolated  $\text{Ag}^+$  ions, while the blue emission maximum is caused by complexes involving  $\text{Ag}^+$  ions and other lattice imperfections. There are several reasons for this interpretation. First,

similar two emission bands are observed in PL spectra of silver-doped alkali halides. [48, 49] It is shown in [48] that in alkali halides, the shorter-wavelength emission band is due to isolated silver ions, while the longer-wavelength emission band is due to pairs of silver ions. Second, the intensity of the SrS:Ag blue emission band increases with increasing the Ag concentration. [51] Increasing Ag concentration in SrS:Ag would promote the creation of complexes involving  $\text{Ag}^+$  ions and other lattice defects. The intensity of the blue emission peak in SrS:Ag thin films also depends on co-dopants. The blue emission peak increases and the UV emission peak decreases in intensity when SrS:Ag is co-doped with Cu. This dependence implies that Ag ions create  $\text{Cu}^+$  complexes, and the number of UV-emitting, isolated Ag centers decreases as SrS:Ag is co-doped with Cu. The dependence of the blue emission peak of SrS:Ag thin films on the Ag and co-dopant concentration is another reason to associate this peak with complex defects involving  $\text{Ag}^+$  and other lattice imperfections.

The nature of the defect complexes causing the blue emission peak in the SrS:Ag emission spectrum is uncertain. Silver ions are known to create a variety of defect complexes in alkali halides. [48] After x-ray irradiation, six different absorption bands arise in Ag-doped NaCl, NaBr, KCl, and KBr crystals. [48] These absorption bands are ascribed to different types of defect complexes involving Ag ions associated with anion or cation vacancies and captured electron or hole. [48] Because cations and anions are doubly charged in SrS, the nature of defect complexes involving Ag ions in SrS:Ag and SrS:Cu,Ag thin films may be even more complicated than in alkali halide crystals.

As the temperature increases to room temperature, the UV emission of SrS:Ag thin films disappears and the blue emission maximum becomes very small. [51] Therefore, SrS doped with just silver cannot be used in EL applications.

Sun et al. [50] have shown that blue-emitting Ag centers in SrS can be activated and greatly enhanced by Cu co-doping. When a SrS thin film is co-doped by Cu and Ag, emission bands from both Cu and Ag centers are observed in PL and EL spectra at 90 K. [51] The blue emission peak corresponding to  $\text{Ag}^+$  complexes is much larger in PL and EL spectra of SrS:Ag,Cu than in the spectra of SrS:Ag thin films. This blue

emission peak also dominates the emission peaks caused by isolated  $\text{Ag}^+$  centers and  $\text{Cu}^+$  centers. At room temperature, in PL and EL spectra of SrS:Ag,Cu ACTFEL devices, only one broad band with peak at approximately 430 nm is observed. This emission maximum has a shorter wavelength than that of SrS:Cu emission and is more intense than SrS:Ag blue emission at room temperature. [51] These results imply that  $\text{Ag}^+$  ions create complexes with  $\text{Cu}^+$  ions. Formation of such complexes results in the increased intensity of the  $\text{Ag}^+$  blue emission.

Formation of the complex centers involving  $\text{Ag}^+$  ions and other lattice defects may provide additional excitation pathways for  $\text{Ag}^+$  centers through energy transfer between the components of the complex centers. This assumption is supported by Park et al. [52], who compared the PLE spectra of SrS:Ag and SrS:Ag,Cu thin films measured by monitoring the  $\text{Ag}^+$  blue emission peak ( $\lambda = 430$  nm) at 10 K. SrS:Ag exhibits two excitation bands at about 4.46 and 4.10 eV. In the SrS:Ag,Cu PLE spectrum, the 4.46 eV excitation band is significantly enhanced and exhibits an additional shoulder at 4.29 eV. The SrS:Ag,Cu PLE spectrum also contains small maxima at 3.96 and 3.60 eV not observed in the SrS:Ag PLE spectrum. By studying of the luminescent decay time, Park et al. has concluded that when  $\text{Ag}^+$  blue emission is excited by 4.46 eV light, there is an energy transfer between  $\text{Cu}^+$  and  $\text{Ag}^+$  ions. When  $\text{Ag}^+$  blue emission is excited using smaller energy photoexcitation, there is no efficient energy transfer between  $\text{Cu}^+$  and  $\text{Ag}^+$  ions.

The electrical properties of SrS:Cu and SrS:Cu,Ag ACTFEL devices have not yet been reported. Also, the nature of space charge and its effect on the ACTFEL device operation has yet to be determined in SrS:Cu and SrS:Ag,Cu ACTFEL devices.

## 2.7 The two-sheet space charge model

To establish the mechanism of phosphor space charge creation in ACTFEL devices, various ACTFEL device models have been developed by numerous researchers. In one of the most successful approaches to simulate space charge effects in ACTFEL devices, developed by Paul Keir [2], the space charge is assumed to be located along

flat, parallel “sheets” discretely distributed inside the ACTFEL device phosphor layer.

The single-sheet space charge model has proven effective in the simulation of overshoot in the electrical characteristics of ZnS:Mn ACTFEL devices. [2, 54] Within the framework of the single-sheet space charge model, positive dynamic space charge arises from the ionization of traps existing at the single sheet of the bulk portion of the phosphor layer, as opposed to arising from the ionization of traps at the phosphor-insulator interface. The position of the single-sheet represents the charge centroid from which trap ionization occurs. Trap ionization is modeled either as field-assisted emission or as trap-to-band impact ionization.

Although the single-sheet space charge model works well for the simulation of ZnS:Mn ACTFEL devices exhibiting overshoot in their electrical characteristics, it is not appropriate for modeling SrS:Ce ACTFEL devices since one must concomitantly model space charge annihilation via electron recombination with bulk traps, as well as space charge creation. The two-sheet space charge model makes it possible to generate positive space charge near the cathodic interface while simultaneously annihilating space charge near the anodic interface that remains from the previous half-cycle of the driving waveform. This is the likely scenario inside SrS-based ACTFEL devices because experimental evidence indicates that a large amount of dynamic phosphor space charge is present in these devices. This positive space charge leads to an enhanced cathode field, and hence, a greater probability of space charge creation near the cathodic phosphor-insulator interface. Likewise, the presence of large amounts of positive space charge in the phosphor layer leads to a reduced field near the anodic phosphor-insulator interface, which should significantly increase the likelihood for electron capture. [25] For these reasons, the two-sheet space charge model is expected to give better results for SrS-based ACTFEL devices than the single-sheet space charge model.

The two-sheet space charge model [2] assumes that the space charge has a discrete distribution inside the phosphor layer along two flat sheets at the arbitrary distances of  $d_{sc1}$  and  $d_{sc2}$  from one of the phosphor-insulator interfaces (Fig. 2.6). In Figure 2.6,

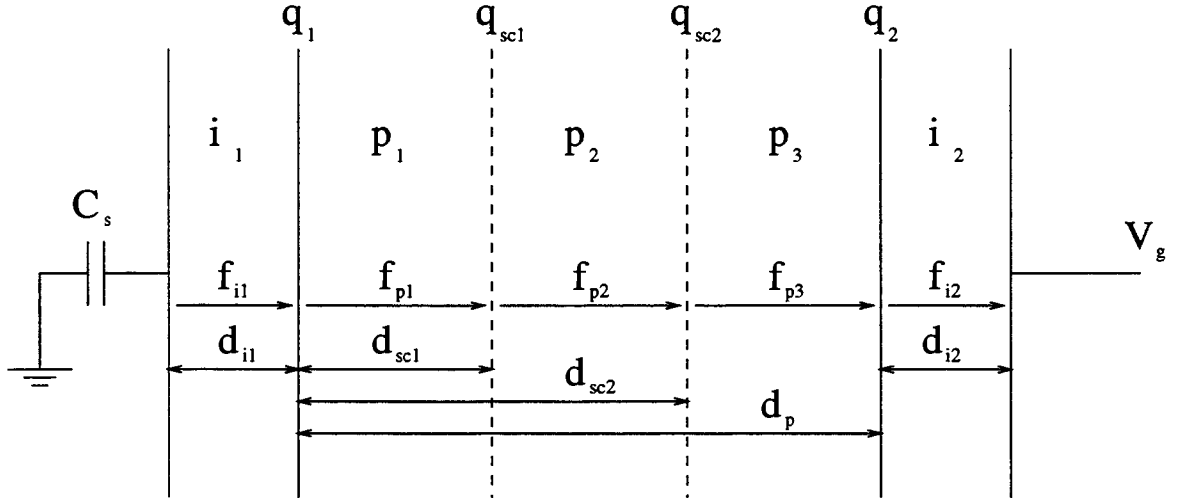


**Figure 2.6.** Two-sheet space charge model of an ACTFEL device.

$q$ ,  $f$  and  $d$  refer to the charge density, electric field, and thickness of the subscripted layers, respectively. Subscripts  $i_1$  and  $i_2$  refer to the insulator layers. Subscripts  $sc_1$  and  $sc_2$  refer to the space charge sheets. Subscripts  $p_1$ ,  $p_2$ , and  $p_3$  refer to the three regions of the phosphor layer separated by the two space charge sheets.  $v_g$  is the applied voltage and  $C_s$  is a sense capacitor.

In Sections 2.7.1 and 2.7.2, analytical expressions are developed for electric field in the three phosphor regions separated by the two space charge sheets.

### 2.7.1 Two-sheet space charge model quasi-statics

Quantitative development of the two-sheet space charge model starts with electrostatic equations written using Kirchhoff's voltage law, Gauss' law, and the principle of charge balance applied to the structure shown in Fig. 2.6 [2]:

$$d_{i1}f_{i1}(t) + d_{sc1}f_{p1}(t) + (d_{sc2} - d_{sc1})f_{p2}(t) + (d_p - d_{sc2})f_{p3}(t) + d_{i2}f_{i2}(t) = -v_g(t) \quad (2.1)$$

$$C_{i1}d_{i1}f_{i1}(t) - C_p d_p f_{p1}(t) = -q_1(t) \quad (2.2)$$

$$C_p d_p [f_{p1}(t) - f_{p2}(t)] = -q_{sc1}(t) \quad (2.3)$$

$$C_p d_p [f_{p2}(t) - f_{p3}(t)] = -q_{sc2}(t) \quad (2.4)$$

$$C_p d_p f_{p3}(t) - C_{i2} d_{i2} f_{i2}(t) = -q_2(t) \quad (2.5)$$

$$C_{i1} d_{i1} f_{i1}(t) = -q_e(t) \quad (2.6)$$

$$q_1 + q_2 + q_{sc1} + q_{sc2} = 0 \quad (2.7)$$

Solving Eqs. (2.1) through (2.7) for the three field components completes the quasistatic analysis of the model:

$$f_{p1}(t) = \frac{1}{C_p d_p} [q_1(t) - q_e(t)] \quad (2.8)$$

$$f_{p2}(t) = \frac{1}{C_p d_p} [q_1(t) + q_{sc1}(t) - q_e(t)] \quad (2.9)$$

$$f_{p3}(t) = -\frac{1}{C_p d_p} [q_2(t) + q_e(t)]. \quad (2.10)$$

### 2.7.2 Two-sheet space charge model dynamics

To obtain the dynamic equations for the three field components, Eqs. (2.8) through (2.10) are differentiated with respect to time [2]:

$$\frac{\partial f_{p1}}{\partial t} = \frac{1}{C_p d_p} \left[ \frac{\partial q_1}{\partial t} - \frac{\partial q_e}{\partial t} \right] \quad (2.11)$$

$$\frac{\partial f_{p2}}{\partial t} = \frac{1}{C_p d_p} \left[ \frac{\partial q_1}{\partial t} + \frac{\partial q_{sc1}}{\partial t} - \frac{\partial q_e}{\partial t} \right] \quad (2.12)$$

$$\frac{\partial f_{p3}}{\partial t} = -\frac{1}{C_p d_p} \left[ \frac{\partial q_2}{\partial t} + \frac{\partial q_e}{\partial t} \right]. \quad (2.13)$$

Next, Eqs. (2.1) through (2.7) are solved for  $q_e$ , the result is differentiated with respect to time, and

$$\frac{\partial q_e}{\partial t} = \frac{C_i}{C_i + C_p} \left[ \frac{\partial q_1}{\partial t} + \left(1 - \frac{d_{sc1}}{d_p}\right) \frac{\partial q_{sc1}}{\partial t} - \left(1 - \frac{d_{sc2}}{d_p}\right) \frac{\partial q_{sc2}}{\partial t} \right] + C_t \frac{dv_g(t)}{dt} \quad (2.14)$$

is obtained. Substitution of Eq. (2.14) into Eqs. (2.11) through (2.13) yields expressions for  $\frac{\partial f_{p1}}{\partial t}$ ,  $\frac{\partial f_{p2}}{\partial t}$ , and  $\frac{\partial f_{p3}}{\partial t}$  in terms of the four internal current densities  $\frac{\partial q_1}{\partial t}$ ,  $\frac{\partial q_2}{\partial t}$ ,  $\frac{\partial q_{sc1}}{\partial t}$ , and  $\frac{\partial q_{sc2}}{\partial t}$ .

### 2.7.3 Electron emission

To obtain expressions for  $\frac{\partial q_1}{\partial t}$ ,  $\frac{\partial q_2}{\partial t}$ ,  $\frac{\partial q_{sc1}}{\partial t}$ , and  $\frac{\partial q_{sc2}}{\partial t}$ , necessary to complete the model, two main sources of conduction electrons in the phosphor layer are considered. The first source, described in detail below, is field-assisted emission of electrons from phosphor-insulator interface traps into the phosphor conduction band. The second source is injection of electrons into the phosphor conduction band from phosphor bulk traps, which creates the space charge. Electron injection from bulk traps can occur in two different ways: by impact ionization of bulk traps after collisions with hot electrons, or by field-assisted emission of electrons from bulk traps. For the simulations presented in this thesis, field-assisted emission from bulk traps is the only mechanism employed as a source of space charge.

The field-assisted emission rate from phosphor-insulator interface traps is described by an expression consisting of three terms illustrated in Fig. 2.7 [2]:

$$e_n = e_n^{PT} + e_n^{thermal} + e_n^{PAT}, \quad (2.15)$$

where  $e_n^{PT}$  is the emission rate due to pure tunneling of electrons from phosphor-insulator interface traps into the phosphor conduction band,  $e_n^{thermal}$  is the thermal emission rate, and  $e_n^{PAT}$  is the emission rate due to phonon-assisted tunneling. Analytical expressions for these three terms, as reported in [55, 56], are:

$$e_n^{PT}(f_p) = \frac{q f_p}{4(2m^* E_{it})^{1/2}} \exp \left[ \left( -\frac{4(2m^*)^{1/2} E_{it}^{3/2}}{3 q \hbar f_p} \right) \left( 1 - \left( \frac{\Delta E_{it}}{E_{it}} \right)^{5/3} \right) \right] \quad (2.16)$$

$$e_n^{thermal}(f_p) = \sigma v_{th} N_c \exp \left( -\frac{E_{it} - \Delta E_{it}}{kT} \right) \quad (2.17)$$

$$e_n^{PAT} = e_n^{thermal} \int_{\Delta E_{it}/kT}^{E_{it}/kT} \exp \left[ z - z^{3/2} \left( \frac{4(2m^*)^{1/2} (kT)^{3/2}}{3 q \hbar f_p} \right) \times \dots \right. \\ \left. \times \left( 1 - \left( \frac{\Delta E_{it}}{z kT} \right)^{5/3} \right) \right] dz, \quad (2.18)$$

where  $f_p$  is the phosphor field,  $q$  is the electronic charge,  $m^*$  is the electron effective mass,  $E_{it}$  is the depth of the discrete interfacial trap,  $\hbar$  is Planck's constant,  $k$  is Boltzmann's constant,  $T$  is the absolute temperature,  $\sigma$  is the capture cross-section for thermal emission,  $N_c$  is the effective density of states,  $v_{th}$  is the thermal velocity

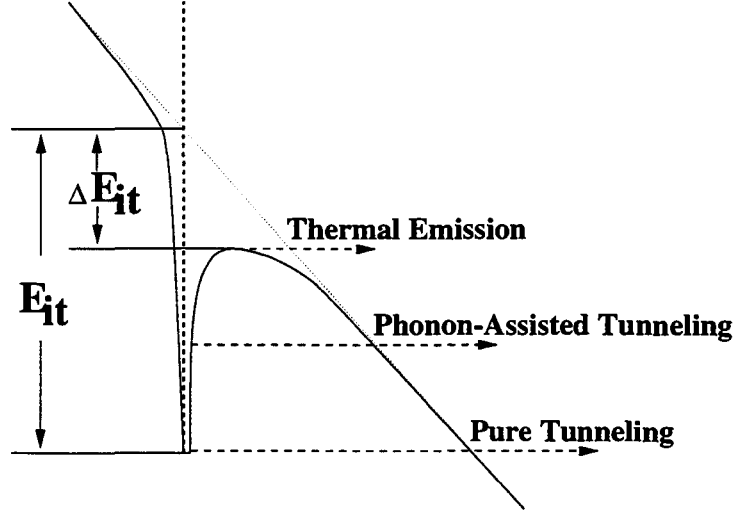


**Figure 2.7.** The three field-assisted emission mechanisms. [2]

of electrons, and  $\Delta E_{it}$  is given by:

$$\Delta E_{it} = q \left( \frac{q f_p}{\pi \epsilon_p} \right)^{1/2}, \quad (2.19)$$

where  $\epsilon_p$  is the phosphor dielectric permittivity. Equations (2.16) through (2.18) substituted into Eq. (2.15) yield the total field-assisted emission rate.

The sought time rate of change of  $q_x(t)$ , the charge on interface  $x$  at time  $t$ , is

$$\frac{\partial q_x}{\partial t} = -q e_n n_x(t), \quad (2.20)$$

where  $n_x(t)$  is the number of electrons present at interface  $x$  at time  $t$ .  $n_x(t)$  can be obtained from an expression for  $q_x(t)$  in terms of  $n_x(t)$ , given by [57]

$$q_x(t) = q[N_0 f_0 - n_x(t)], \quad (2.21)$$

where  $N_0 f_0$  is the no-field occupancy of the interface in question. Solving the above equation for  $n_x(t)$  and substituting  $n_x(t)$  into Eq. (2.20) yields

$$\frac{\partial q_x}{\partial t} = -e_n [q N_0 f_0 - q_x(t)] \quad (2.22)$$

where  $q_x(t)$  can be found in terms of the phosphor fields using Eqs. (2.1) through (2.7). Finally, substitution of  $e_n$  from Eq. (2.15) into Eq. (2.22) yields expressions for both  $\frac{\partial q_1}{\partial t}$  and  $\frac{\partial q_2}{\partial t}$ .

$\frac{\partial q_{sc1}}{\partial t}$  and  $\frac{\partial q_{sc2}}{\partial t}$  are given by the same expressions, with the trap depth and no-field occupancy substituted by the values for phosphor bulk. This completes the derivation of dynamic equations for electric field in the three phosphor regions separated by the two space charge sheets, used for simulations presented in Sec. (4.2) of this thesis.

## Chapter 3

### EXPERIMENTAL TECHNIQUE

This chapter presents the experimental setup for ACTFEL device characterization, ACTFEL device characterization methods, and ACTFEL device sample preparation used in this thesis.

#### 3.1 Experimental setup

The circuit commonly used for ACTFEL device characterization is shown in Fig. 3.1. A Wavetek model 395 arbitrary waveform generator creates a driving waveform with a maximum magnitude of 5 volts. A custom-built amplifier amplifies the driving waveform to a maximum magnitude of about 320 volts.

A series resistor  $R_s$  shown in Fig. 3.1 is used for two purposes. The first purpose is to limit the current that the amplifier would have to source under short-circuit conditions in case of ACTFEL device breakdown. The second purpose is to protect the ACTFEL device from a breakdown by limiting the current through the ACTFEL device. The value for  $R_s$  is chosen depending on the application. Small  $R_s$  values (0 – 500  $\Omega$ ) are used for measurements, when ideal waveforms are desired, since  $R_s$  distorts the driving waveform. Large  $R_s$  values ( $\sim 3000 \Omega$ ) are used for ACTFEL device aging, when ideal driving waveforms are unnecessary, but it is important to prevent the ACTFEL device from breaking down during aging (Sec. 3.3).

A sense capacitor  $C_s$  shown in Fig. 3.1 is used to measure the external charge,  $q_e(t)$ , across the ACTFEL device (Eq. (3.1)). The value of the sense capacitor ( $\sim 100$  nF) is usually at least 100 times greater than the total capacitance of the ACTFEL device ( $\sim 1$  nF), so that the voltage drop across the sense capacitor is negligible compared to the voltage drop across the ACTFEL device. This experimental

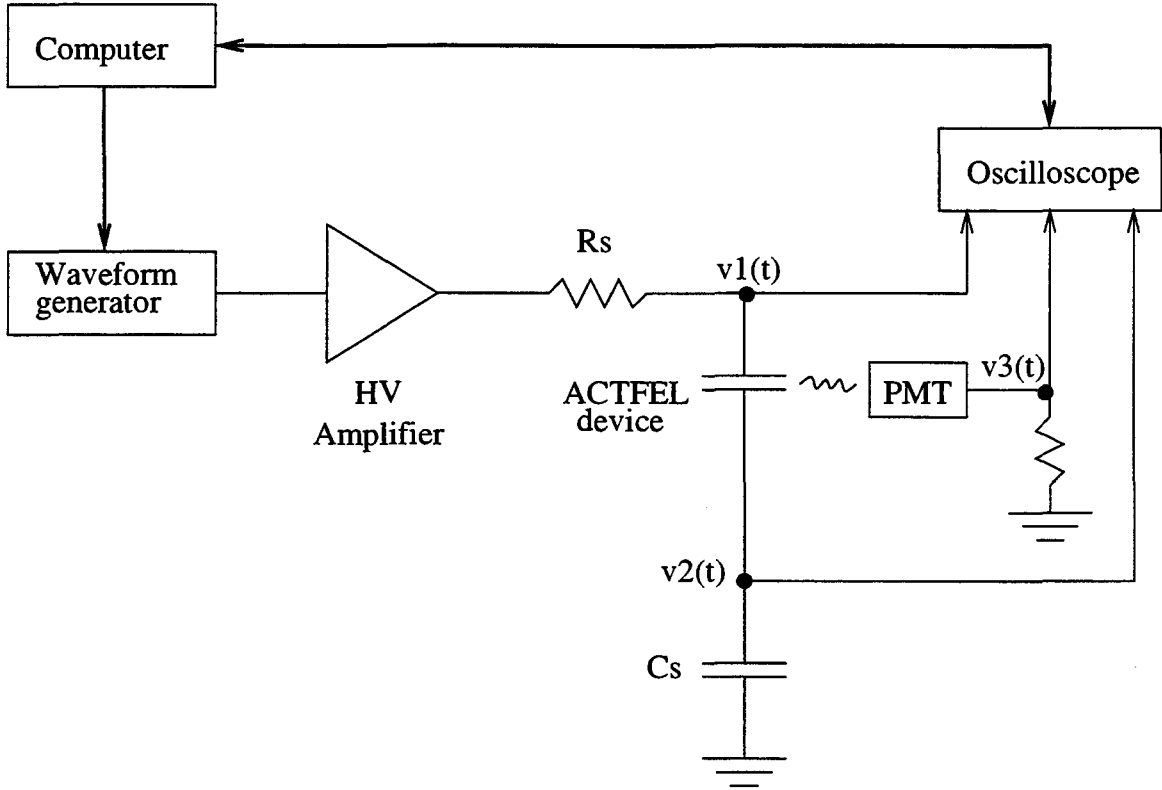


**Figure 3.1.** Experimental setup for ACTFEL device characterization.

configuration, using a sense capacitor to measure the charge across a capacitive sample, was initially employed by C. B. Sawyer and C. H. Tower [58] and is referred to as the “Sawyer-Tower configuration”.

The photo-multiplier tube (PMT) shown in Fig. 3.1 is used to measure the light output from the ACTFEL device. Current generated by the PMT is measured using a small sense resistor.

A Tektronix TDS 420 digital oscilloscope is used to monitor the voltage at the ACTFEL device top ( $v_1(t)$ ) and bottom ( $v_2(t)$ ) electrodes and the light output from the device, which is proportional to  $v_3(t)$ .  $v_2(t)$  is also used to calculate  $q_e(t)$ . A personal computer controls the waveform generator and the oscilloscope using a GPIB interface and is used to process the data retrieved from the oscilloscope.

## 3.2 ACTFEL device characterization methods

### 3.2.1 External charge versus external voltage ( $Q-V$ ) ACTFEL device characteristics

A  $Q - V$  curve is obtained by plotting the external charge per unit area across the ACTFEL device ( $q_e(t)$ ) versus the external voltage across the ACTFEL device ( $v_g(t)$ ).  $q_e(t)$  and  $v_g(t)$  are given by

$$q_e(t) = \frac{C_s}{A} v_2(t) \quad (3.1)$$

$$v_g(t) = v_1(t) - v_2(t), \quad (3.2)$$

where  $C_s$  is the capacitance of the sense capacitor,  $A$  is the ACTFEL device active area (area of the top aluminum electrode),  $v_2(t)$  is the voltage drop across the sense capacitor and the potential at the ACTFEL device bottom electrode at the same time, and  $v_1(t)$  is the potential at the ACTFEL device top electrode (Fig. 3.1). A typical  $Q - V$  plot for an ideal ACTFEL device is shown in Fig. 3.2. The labels  $A$  through  $J$  in Fig. 3.2 correspond to the reference points of the driving waveform shown in Fig. 2.2.

A  $Q - V$  curve provides several quantities of interest. The total ACTFEL device capacitance  $C_t$  can be determined as the slope of a  $Q - V$  plot ( $dq_e(t)/dv_g(t)$ ) at  $v_g(t) < V_{to}$ , where  $V_{to}$  is the ACTFEL device turn-on voltage. (curve sections  $AB$  and  $FG$ , Fig. 3.2). The ideal ACTFEL device insulator capacitance  $C_i$  is equal to the slope of a  $Q - V$  plot at  $v_g(t) > V_{to}$  (curve sections  $BC$  and  $GH$ , Fig. 3.2). The reason why  $C_t$  and  $C_i$  are equal to the slope of the respective sections of an ideal ACTFEL device  $Q - V$  plot is given in Sec. 3.2.3.

Other quantities of interest provided by a  $Q - V$  plot are external polarization charge  $Q_{pol}^e$  determined as the charge across the ACTFEL device at the beginning of each pulse ( $|Q(A)|$  and  $|Q(F)|$ ), external leakage charge  $Q_{leak}^e$  determined as the charge that “leaks” from phosphor-insulator interfaces during the interpulse pause ( $|Q(E) - Q(F)|$  and  $|Q(J) - Q(A)|$ ), relaxation charge  $Q_{relax}^e$  determined as the charge that “relaxes” the phosphor field during the hold time portion of the pulse ( $|Q(D) -$

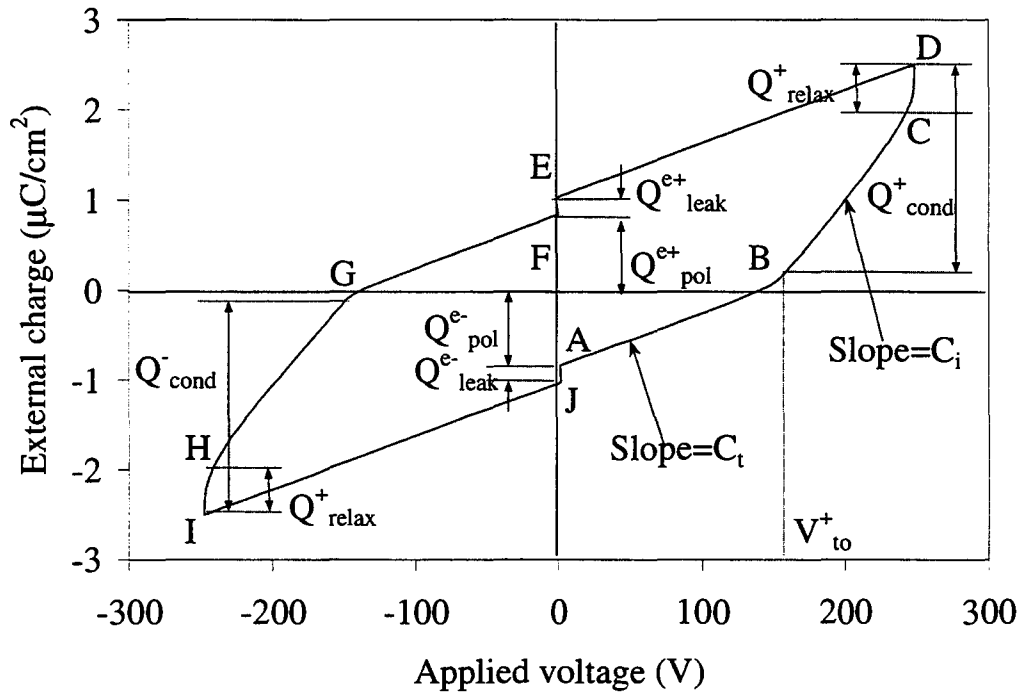


**Figure 3.2.** ACTFEL device  $Q - V$  plot.

$Q(C)$  and  $|Q(I) - Q(H)|$ , and the maximum external charge  $Q_{max}^e$  determined as  $|Q(D)|$  and  $|Q(I)|$ .

### 3.2.2 Dynamic capacitance versus external voltage ( $C - V$ ) ACTFEL device characteristics

A  $C - V$  curve is obtained by plotting the ACTFEL device dynamic capacitance  $C(t)$  versus the external voltage across the ACTFEL device  $v_g(t)$ . In this thesis,  $C(t)$  is measured as

$$C(t) = \frac{dq_e(t)}{dv_g(t)}. \quad (3.3)$$

$q_e(t)$  and  $v_g(t)$  are given by Eqs. (3.1) and (3.2).

A typical  $C - V$  curve for an ideal ACTFEL device is shown in Fig. 3.3.  $C - V$  curves are usually plotted only for the rise time portion of the driving waveform. A  $C - V$  plot of an ideal ACTFEL device has two sections where the capacitance is

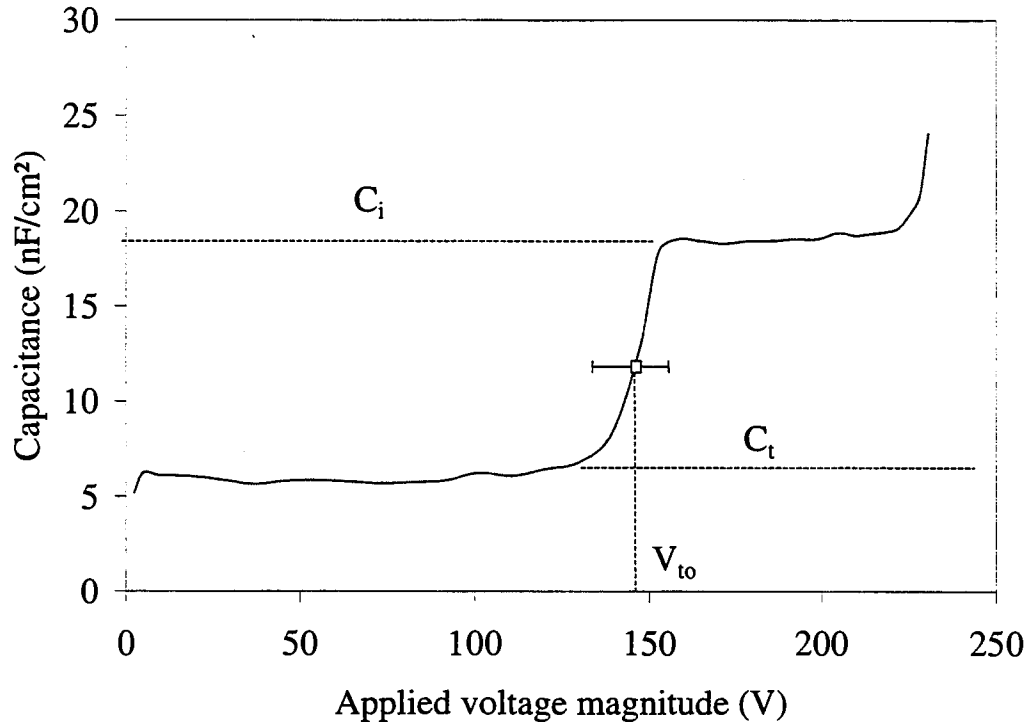


**Figure 3.3.** ACTFEL device  $C - V$  plot.

constant. The capacitance in the low-voltage constant section of the  $C - V$  curve represents the slope of the  $AB$  section of the  $Q - V$  plot (Fig. 3.2) and is equal to  $C_t$ . The capacitance in the high-voltage constant section of the  $C - V$  curve represents the slope of the  $BC$  section of the  $Q - V$  plot (Fig. 3.2) and is equal to  $C_i$ . The ACTFEL device turn-on voltage,  $V_{to}$ , is easily estimated from a  $C - V$  plot as the voltage at which the ACTFEL device dynamic capacitance reaches a specific value (e. g.  $(C_t + C_i)/2$ ) between  $C_t$  and  $C_i$ .

### 3.2.3 Internal charge versus phosphor field ( $Q_{int} - F_p$ ) ACTFEL device characteristics

A  $Q_{int} - F_p$  curve is obtained by plotting internal charge,  $q_{int}(t)$ , versus average electric field across the phosphor layer (phosphor field,  $f_p(t)$ ). In ideal ACTFEL devices, the internal charge represents the charge accumulated at phosphor-insulator

interfaces of an operating ACTFEL device.  $q_{int}(t)$  and  $f_p(t)$  are given by [57]

$$q_{int}(t) = \frac{C_i + C_p}{C_i} q_e(t) - C_p v_g(t), \quad (3.4)$$

$$f_p(t) = \frac{1}{d_p} \left[ \frac{q_e(t)}{C_i} - v_g(t) \right], \quad (3.5)$$

where  $C_i$  is the total capacitance of the two insulator layers,  $C_p$  is the phosphor capacitance,  $d_p$  is the phosphor thickness,  $q_e(t)$  is the charge measured at the sense capacitor (Eq. (3.1)), and  $v_g(t)$  is the voltage applied to the ACTFEL device (Eq. (3.2)).

For derivation of Eqs. (3.4) and (3.5), the phosphor space charge is assumed to be zero and the field — constant across the phosphor layer.

Equations (3.4) and (3.5) provide conditions at which the slope of an ACTFEL device  $Q - V$  plot (Fig. 3.2) is equal to  $C_t$  or  $C_i$ . Differentiating Eqs. (3.4) and (3.5) with respect to  $v_g(t)$  yields

$$\frac{1}{C_p} \frac{dq_{int}(t)}{dv_g(t)} = \frac{C_i + C_p}{C_i C_p} \frac{dq_e(t)}{dv_g(t)} - 1 \quad (3.6)$$

$$\frac{df_p(t)}{dv_g(t)} = \frac{1}{d_p} \left[ \frac{1}{C_i} \frac{dq_e(t)}{dv_g(t)} - 1 \right] \quad (3.7)$$

As follows from Eq. (3.6), ACTFEL device dynamic capacitance  $\frac{dq_e(t)}{dv_g(t)}$  equals to  $C_t \equiv \frac{C_i C_p}{C_i + C_p}$  when

$$\frac{dq_{int}(t)}{dv_g(t)} = 0, \quad (3.8)$$

i. e. when there is no current through the ACTFEL device phosphor layer. Condition (3.8) is true in an ACTFEL device at  $v_g(t) < V_{to}$ , when no electrons are injected into the phosphor conduction band and phosphor operates as an insulator. This is the reason why the slope of sections  $AB$  and  $FG$  of an ACTFEL device  $Q - V$  plot (Fig. 3.2) is equal to  $C_t$ . As follows from Eq. (3.7), ACTFEL device dynamic capacitance  $\frac{dq_e(t)}{dv_g(t)}$  is equal to  $C_i$  when

$$\frac{df_p(t)}{dv_g(t)} = 0, \quad (3.9)$$

i. e. when the phosphor field remains constant as the external voltage increases. Condition (3.9) is equivalent to the condition

$$\frac{dq_{int}(t)}{dt} = \frac{dq_e(t)}{dt}, \quad (3.10)$$

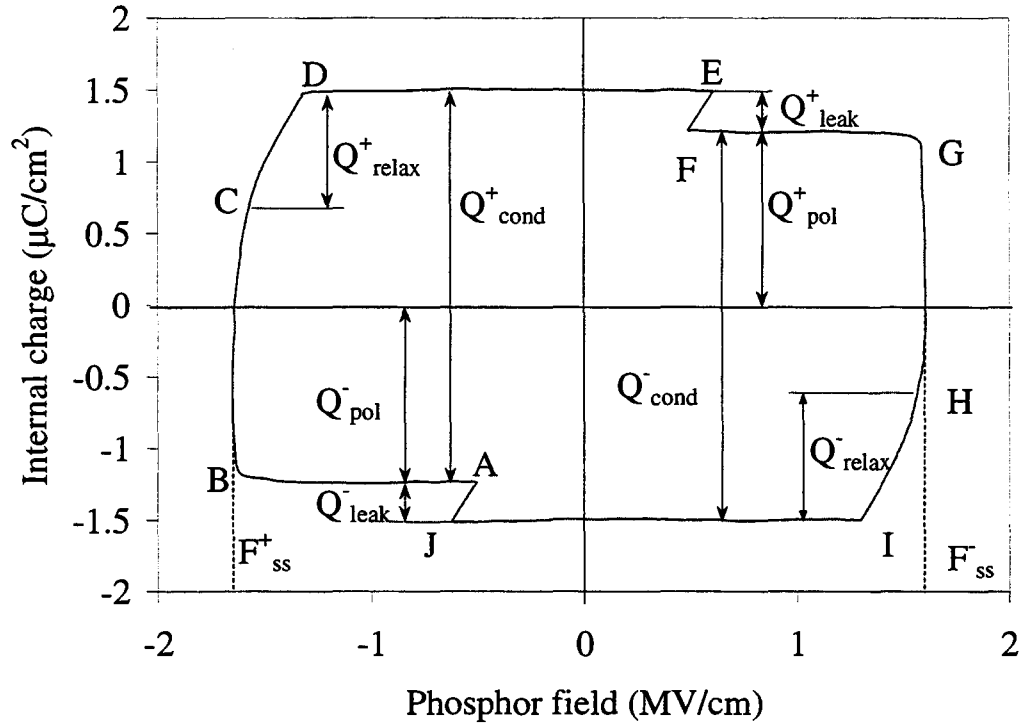


**Figure 3.4.** ACTFEL device  $Q_{int} - F_p$  plot.

i. e. internal current through the ACTFEL device phosphor layer is equal to the external current in the circuit. Conditions (3.9) and (3.10) are true in an ideal ACTFEL device at  $v_g(t) > V_{to}$ , when the increment of phosphor field caused by  $v_g(t)$  increase is fully compensated by the field created by the charge transferred between the two phosphor-insulator interfaces and the ACTFEL device phosphor layer operates as a conductor. This is the reason why the slope of sections  $BC$  and  $GH$  of an ideal ACTFEL device  $Q - V$  plot is equal to  $C_i$ . The constant phosphor field established in an ideal ACTFEL device at the  $BC$  and  $GH$  sections of the driving waveform is called “steady state field” ( $F_{ss}$ ).

A typical  $Q_{int} - F_p$  curve for an ideal ACTFEL device is shown in Fig. 3.4.  $Q_{int} - F_p$  plots provide the same information about an ACTFEL device as  $Q - V$  plots; however, the values of polarization, relaxation and leakage charges determined

from a  $Q - V$  plot in Sec. 3.2.1 are presented in a  $Q_{int} - F_p$  plot as values of respective internal charges. If an ACTFEL device achieves a steady state, the value of steady-state field,  $F_{ss}$ , can be determined from a  $Q_{int} - F_p$  plot.

Although  $Q - V$  and  $Q_{int} - F_p$  plots provide similar information about an ACTFEL device,  $Q_{int} - F_p$  plots are more convenient to read than  $Q - V$  plots, since phosphor-related phenomena are more evident in  $Q_{int} - F_p$  plots owing to compensation of the insulator capacitance effect. However, conclusions based on  $Q_{int} - F_p$  plots rely on how accurate  $C_t$  and  $C_i$  are known making experimental estimation of these values important. While it is always possible to estimate the total ACTFEL device capacitance, obtaining a reliable value for the insulator capacitance is not always easy and deserves a more detailed consideration.

### 3.2.4 *Transient current ( $i(t)$ ) and transient luminance ( $b(t)$ ) ACTFEL device characteristics*

In this thesis, transient current through the ACTFEL device is measured as

$$i(t) = \frac{dq_e(t)}{dt}. \quad (3.11)$$

Where  $q_e(t)$  is the external charge on the ACTFEL device measured at the sense capacitor (Eq. (3.1)). A resistor can be used in the experimental setup (Fig. 3.1) as a sense element to monitor the current directly; however, a sense capacitor is used for current measurements in order to perform all electrical measurements in a single automated run, without changing the setup.

A typical transient current plot for an ideal ACTFEL device is shown in Fig. 3.5. During the rise time portion of the driving waveform, there is a current between the ACTFEL device electrodes proportional to  $C(t)$  and to the time derivative of  $v_g(t)$ :

$$i(t) \equiv \frac{dq_e(t)}{dt} = \frac{dq_e(t)}{dt} \frac{dv_g(t)}{dv_g(t)} = C(t) \frac{dv_g(t)}{dt}. \quad (3.12)$$

During the hold time portion of the driving waveform, current through the ACTFEL device exponentially drops to zero, as  $\frac{dv_g(t)}{dt}$  drops to zero. During the fall time portion of the driving waveform, there is a current between the ACTFEL device electrodes

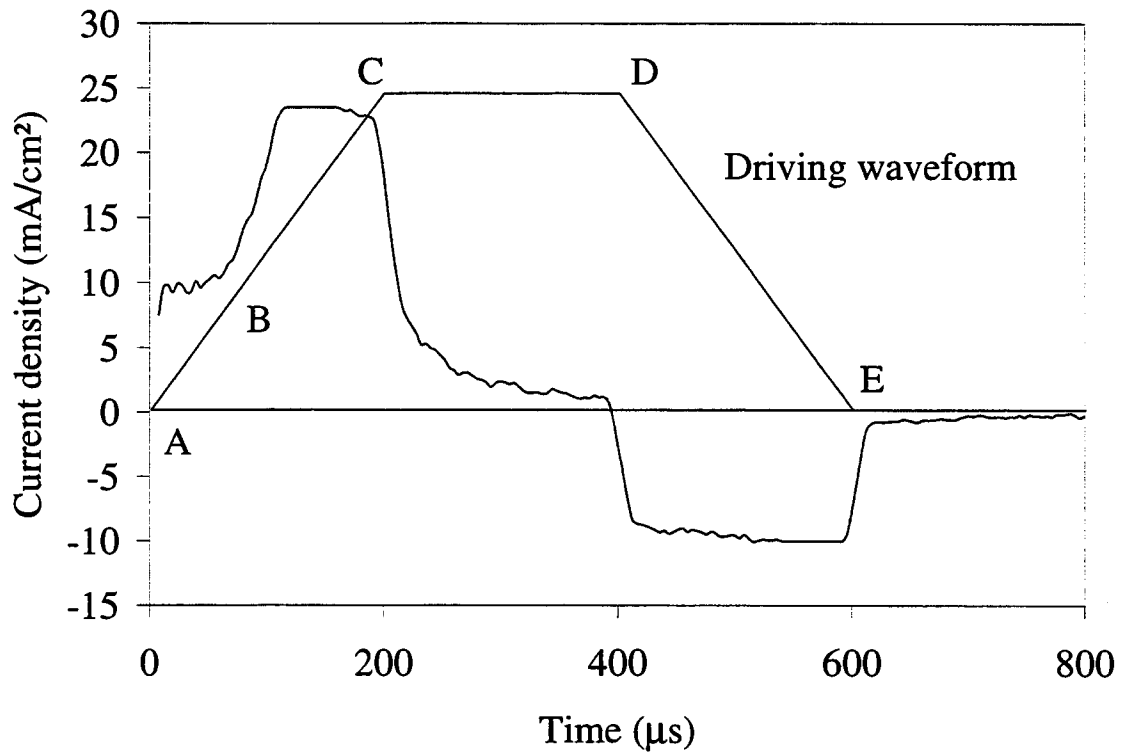


**Figure 3.5.** ACTFEL device  $i(t)$  plot.

opposite to the current flowing during the rise time portion of the driving waveform, as  $\frac{dv_g(t)}{dt}$  is negative during the fall time portion of the driving waveform. Finally, during the interpulse pause, the current between the ACTFEL device electrodes decreases to zero again.

Transient luminance plots are obtained by monitoring the current generated by the PMT, which is proportional to the number of photons emitted by the ACTFEL device.

### 3.3 ACTFEL device sample preparation

Electrical and optical characteristics of the ACTFEL devices used in this thesis change depending on the total time the ACTFEL device has been operated and the conditions of operation. This change is called “aging” and creates a problem for ACTFEL device characterization, since unrepeatable measurement results are not reliable. Fortunately, ACTFEL device aging slows down greatly after a few hours of operation at proper conditions. Therefore, it is possible to neglect the changes in ACTFEL device characteristics after a proper ACTFEL device aging procedure. The “proper” aging procedure must satisfy three conditions [59]: 1) the ACTFEL device must be in a testable condition after aging; 2) characteristics of the aged ACTFEL device must be stable; 3) the aging procedure must be repeatable. The first condition is met if the whole area of the aged ACTFEL device is able to emit light; otherwise, if only a portion of the ACTFEL device area operates, it is impossible to measure the external charge per unit area of the ACTFEL device. The second condition is met by choosing an appropriate aging duration and aging driving waveform. ACTFEL devices age faster at large frequency and slew rate of the driving waveform. The aging duration is chosen to provide stability of ACTFEL device characteristics for the duration of measurement, i. e. from a few minutes to an hour. The third condition is necessary to automate aging and to compare different ACTFEL devices.

In this thesis, ACTFEL device characteristics are stabilized by aging the ACTFEL device for more than 4 hours using a bipolar trapezoidal waveform having 5  $\mu$ s rise, 30  $\mu$ s hold, and 5  $\mu$ s fall time portions, a frequency 1000–2000 Hz, and a magnitude of about 40 V above the ACTFEL device threshold. A large ( $\sim 3000 \Omega$ ) current-limiting resistor,  $R_s$ , is used at the output of the amplifier (Fig. 3.1) to prevent the ACTFEL device from breaking down during aging.

### 3.4 Design of experiment

A designed experiment is a test or series of tests in which purposeful variations are made to the input variables of a process so that corresponding changes in the output response may be observed and identified. [60] Design of experiment (DOE) is extremely useful when it is necessary to optimize a response variable of a process controlled by many factors.

When a response variable depends on several control factors, a factorial DOE should be used. In a factorial design of experiment, all possible combinations of the levels of the control factors are investigated. Thus, if there are two control factors  $A$  and  $B$  with  $a$  levels for factor  $A$  and  $b$  levels for factor  $B$ , then each replication of the designed experiment contains all  $ab$  possible combinations of the levels, which is equal to the number of runs in each replication.

The number of runs in each replication of the designed experiment increases rapidly with the amount of control factors used and with the amount of levels of each control factor. To reduce the amount of runs in each replication of the designed experiment, the number of levels of each control factor is usually reduced to a minimum of two. These levels are usually referred to as “low” or “–” and “high” or “+”. In this case, each complete replication of the designed experiment contains  $2^k$  runs, where  $k$  is the number of control factors. An experimental design with two levels for each control factor is called “a  $2^k$  factorial design”.

When the number of control factors is too large, it is desirable to reduce the amount of runs in each replication of a  $2^k$  factorial designed experiment. In most cases, it is possible to use a  $1/2$ ,  $1/4$  or  $1/8$  fraction of runs to obtain information on the main effects of the control factors. The details on how to choose the runs for a fractional replication of a  $2^k$  design are given in [60]. Usually, after a fractional DOE, a detailed experiment is designed using fewer, the most significant, control factors.

A main effect of a factor is defined as the change in response produced by a change in the level of the factor. For example, the main effect of factor  $A$  is found as

$$A = \bar{y}_{A+} - \bar{y}_{A-}, \quad (3.13)$$

where  $\bar{y}_{A+}$  is the response variable mean value for the runs performed at high values of factor  $A$ , and  $\bar{y}_{A-}$  is the response variable mean value for the runs performed at low values of factor  $A$ .

In this thesis, using the two-sheet space charge model, the simulated  $Q_{int} - F_p$  curves are fit to the experimental data using the following procedure. First, a fractional  $2^k$  DOE procedure is undertaken in which the effect of the two-sheet space charge model parameters in determining various  $C-V$  and  $Q_{int}-F_p$  response variables is assessed. A commercially available statistical software package (*StatGraphics*) is used to establish which model parameters are statistically significant in determining a given response variable. Then, for each response variable of interest, a more detailed DOE is performed using fewer, the most significant for the specific variable, control factors so that optimal model parameters for the curve-fit can be deduced. Finally, the simulated  $Q_{int} - F_p$  curves are fit to the experimental data to verify the two-sheet space charge model.

## Chapter 4

### EXPERIMENTAL AND SIMULATION RESULTS

The first section of this chapter introduces two new methods for estimation of the insulator capacitance of ACTFEL devices with dynamic space charge. The second section presents results of simulation of SrS:Ce ACTFEL device electrical characteristics using the two-sheet space charge model. In the third section of this chapter, electrical characteristics of SrS:Ce, SrS:Cu, and SrS:Cu,Ag ACTFEL devices are compared.

#### 4.1 Estimation of the insulator capacitance for an ACTFEL device with dynamic space charge

The insulator capacitance ( $C_i$ ) is an important parameter for characterization and device physics assessment of ACTFEL devices. For example, insulator capacitance is used in calculations of the internal charge and phosphor field of an ACTFEL device (Sec. 3.2.3). For ACTFEL devices which exhibit a large amount of dynamic space charge, it is difficult to estimate the insulator capacitance from electrical measurements. In ideal ACTFEL devices, the insulator capacitance is usually determined from  $Q - V$  plots as the slope of the after-turn-on linear section of the  $Q - V$  plot which corresponds to the rise time portion of the driving waveform. (Sec. 3.2.1, 3.2.3) In ACTFEL devices with dynamic space charge, the after-turn-on section of the  $Q - V$  plot is non-linear, which makes it difficult to estimate  $C_i$ . Insulator capacitance values obtained from estimation of insulator layer thicknesses and dielectric constants are often unreliable. A poor estimate of  $C_i$  leads to the calculation of distorted  $Q_{int} - F_p$  plots and to misleading conclusions about ACTFEL device properties and physics.

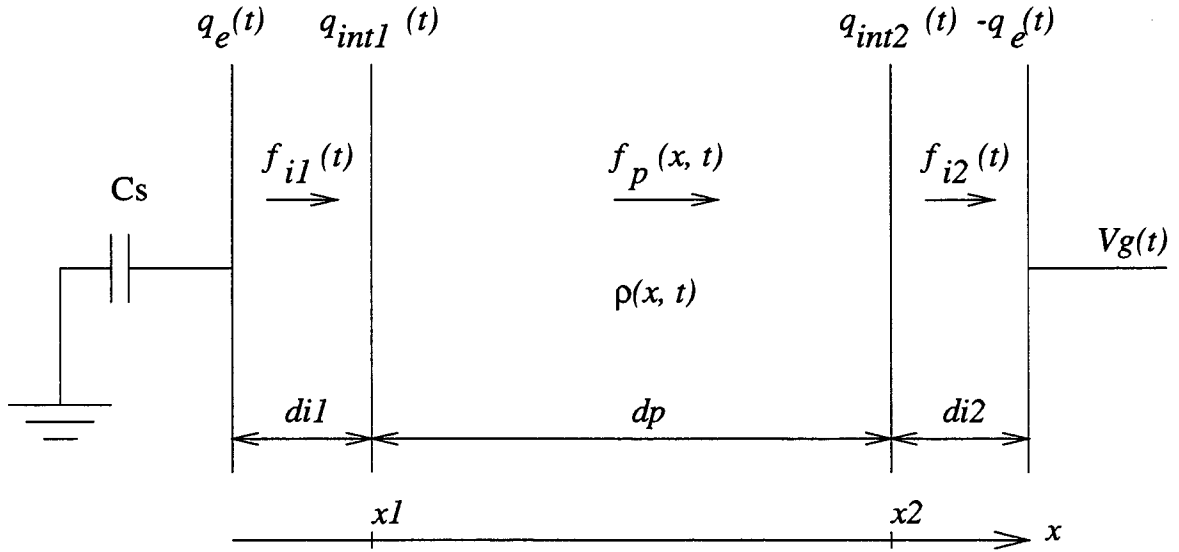


**Figure 4.1.** Diagram of an ACTFEL device with continuous phosphor space charge distribution.

The purpose of the present section is to introduce two new methods of insulator capacitance estimation of ACTFEL devices with dynamic space charge. The first method allows estimation of the insulator capacitance as the ACTFEL device static capacitance,  $C^{stat}(t_0) \equiv \frac{q_e(t_0)}{v_g(t_0)}$ , provided that  $C^{stat}(t_0) = C_i$  at some specific  $t_0$ . The second method allows estimation of the insulator capacitance as the ACTFEL device dynamic capacitance,  $C^{dyn}(t) \equiv \frac{dq_e(t)}{dv_g(t)}$ , provided that  $C^{dyn}(t) = C_i$  under certain conditions.

#### 4.1.1 Static capacitance $C_i$ estimation

In order to determine the condition when  $C_i$  can be estimated as a static capacitance,  $C^{stat}(t_0)$ , consider an ACTFEL device with a continuously distributed phosphor space charge layer with volume density  $\rho(x)$  (Fig. 4.1). Electrostatic equations for the ACTFEL device shown in Fig. 4.1 may be written using Kirchhoff's voltage

law, Gauss' law, and charge balance as follows:

$$d_{i1}f_{i1}(t) + \int_{x_1}^{x_2} f_p(x, t)dx + d_{i2}f_{i2}(t) = -v_g(t) \quad (4.1)$$

$$\epsilon_{i1}f_{i1}(t) = \epsilon_{i2}f_{i2}(t) = -q_e(t) \quad (4.2)$$

$$-\epsilon_{i1}f_{i1}(t) + \epsilon_p f_p(x_1, t) = q_{int1}(t) \quad (4.3)$$

$$\epsilon_{i2}f_{i2}(t) - \epsilon_p f_p(x_2, t) = q_{int2}(t) \quad (4.4)$$

$$\epsilon_p [f_p(x_1, t) - f_p(x_2, t)] = \int_{x_1}^{x_2} \rho(x, t)dx \quad (4.5)$$

$$q_{int1}(t) + \int_{x_1}^{x_2} \rho(x, t)dx + q_{int2}(t) = 0, \quad (4.6)$$

where  $d_n$  is the thickness of layer  $n$ ,  $\epsilon_n$  is the dielectric permittivity of layer  $n$ ,  $f_n(t)$  is the electric field within layer  $n$ ,  $q_n(t)$  is the charge per unit area at interface  $n$ , and  $\rho(x, t)$  is the phosphor space charge volume density. Subscripts  $i1$  and  $i2$  denote the two ACTFEL device insulator layers, subscript  $p$  denotes the phosphor layer, subscripts  $int1$  and  $int2$  denote the two ACTFEL device phosphor-insulator interfaces, and subscript  $e$  denotes the ACTFEL device electrodes.  $x_1$  and  $x_2$  are the coordinates of the ACTFEL device phosphor-insulator interfaces. Equations (4.1) and (4.2) yield

$$d_p \bar{f}_p(t) = \frac{1}{C_i} q_e(t) - v_g(t), \quad (4.7)$$

where

$$\bar{f}_p(t) \equiv \frac{1}{d_p} \int_{x_1}^{x_2} f_p(x, t)dx \quad (4.8)$$

is the average field across the phosphor layer, and  $C_i$  is the total insulator capacitance per unit area given by

$$\frac{1}{C_i} \equiv \frac{d_{i1}}{\epsilon_{i1}} + \frac{d_{i2}}{\epsilon_{i2}}. \quad (4.9)$$

It follows from Eq. (4.7) that static capacitance  $C_i$  estimation,

$$C_i = \frac{q_e(t_0)}{v_g(t_0)}, \quad (4.10)$$

can be accomplished when

$$\bar{f}_p(t_0) = 0 \quad (4.11)$$

at some time,  $t_0$ , when  $v_g(t_0) \neq 0$ . Equations (4.7) through (4.10) show that the static capacitance  $C_i$  estimation requires that the average phosphor field is equal

to zero. This requirement is satisfied at some time,  $t_0$ , during the fall time portion of the driving waveform. It is shown in Sec. 2.2 and Fig. 4.2 (c) that the average phosphor field changes its sign and, hence, becomes zero during the voltage pulse fall time, when condition specified by Eq. (4.11) is satisfied. The time  $t_0$  may be estimated as corresponding to the ACTFEL device luminance transient minimum,  $b(t_0)$  (Fig. 4.2 (b)).

A static capacitance  $C_i$  estimate ( $C_i^{stat}$ ) can be obtained using the following procedure. First, the luminance transient minimum,  $b(t_0)$  (Fig. 4.2 (b)), during the voltage pulse fall time is detected using an oscilloscope, and  $v_g(t_0)$  and  $q_e(t_0)$  (Fig. 4.2 (a)) corresponding to this minimum are measured. The  $C_i^{stat}$  estimate is then obtained using Eq. (4.10). In order to obtain a distinct luminance transient minimum during the voltage pulse fall time, the voltage pulse magnitude must be large enough (e. g.  $V_{max} = V_{th} + 40$  V) that a fully developed luminance transient minimum is established. In order to measure  $v_g(t_0)$  and  $q_e(t_0)$  accurately, a long voltage pulse waveform is employed (e. g. 200  $\mu$ s is typically used for the rise time, fall time, and pulse width of the applied voltage waveform).  $q_e(t_0)$  is corrected for the DC offset which builds up in some ACTFEL devices. [61]

To validate this static capacitance  $C_i$  estimation procedure,  $C_i^{stat}$  values are obtained for several ACTFEL devices using different applied voltage pulse polarities and magnitudes. For each ACTFEL device measured, a 95%-confidence interval is obtained for  $C_i^{stat}$  values. The results of this validation are discussed in Sec. 4.1.3.

### 4.1.2 Dynamic capacitance $C_i$ estimation

In order to derive the second condition establishing when  $C_i$  can be found as ACTFEL device dynamic capacitance, consider time derivatives of Eqs. (4.1) through (4.7):

$$d_{i1} \frac{df_{i1}(t)}{dt} + \int_{x_1}^{x_2} \frac{\partial f_p(x, t)}{\partial t} dx + d_{i2} \frac{df_{i2}(t)}{dt} = -\frac{dv_g(t)}{dt}, \quad (4.12)$$

$$\epsilon_{i1} \frac{df_{i1}(t)}{dt} = \epsilon_{i2} \frac{df_{i2}(t)}{dt} = -\frac{dq_e(t)}{dt}, \quad (4.13)$$

$$-\epsilon_{i1} \frac{df_{i1}(t)}{dt} + \epsilon_p \frac{df_p(x_1, t)}{dt} = \frac{dq_{int1}(t)}{dt}, \quad (4.14)$$

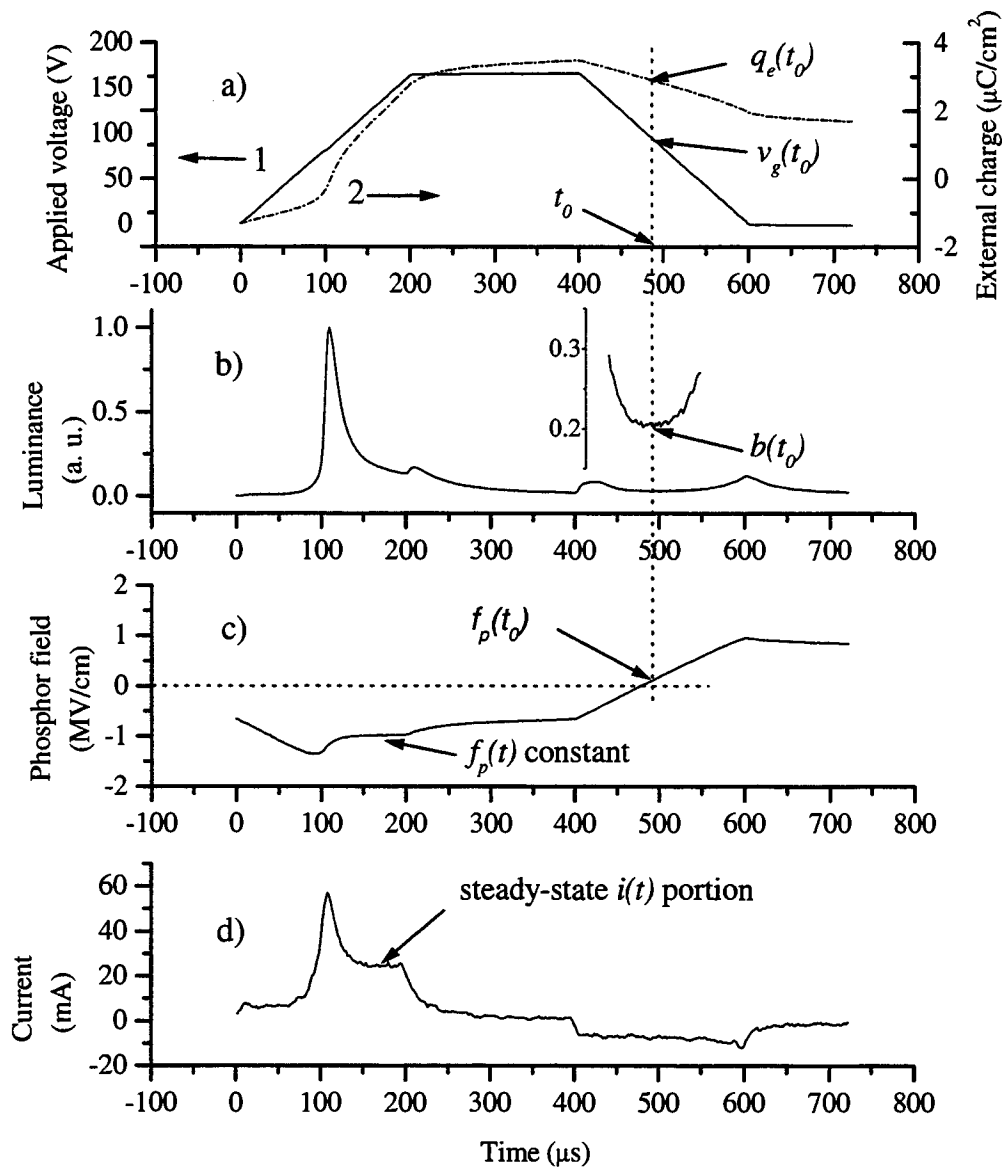


**Figure 4.2.** (a) Long voltage pulse waveform (curve 1) and external charge transient (curve 2), (b) luminance transient plot, (c) phosphor field transient plot calculated using the  $C_i^{dyn}$  estimate, and (d) current transient plot for a SrS:Ce ACTFEL device.

$$\epsilon_{i2} \frac{df_{i2}(t)}{dt} - \epsilon_p \frac{df_p(x_2, t)}{dt} = \frac{dq_{int2}(t)}{dt}, \quad (4.15)$$

$$\epsilon_p \left[ \frac{df_p(x_1, t)}{dt} - \frac{df_p(x_2, t)}{dt} \right] = \int_{x_1}^{x_2} \frac{\partial \rho(x, t)}{\partial t} dx, \quad (4.16)$$

$$\frac{dq_{int1}(t)}{dt} + \int_{x_1}^{x_2} \frac{\partial \rho(x, t)}{\partial t} dx + \frac{dq_{int2}}{dt} = 0, \text{ and,} \quad (4.17)$$

$$d_p \frac{d\bar{f}_p(t)}{dt} = \frac{1}{C_i} \frac{dq_e(t)}{dt} - \frac{dv_g(t)}{dt}. \quad (4.18)$$

It follows from Eq. (4.18) that dynamic capacitance  $C_i$  estimation,

$$C_i = \frac{dq_e(t)}{dv_g(t)}, \quad (4.19)$$

can be accomplished when

$$\frac{d\bar{f}_p(t)}{dt} = 0. \quad (4.20)$$

In an ideal ACTFEL device,

$$\rho(x) = 0, \quad (4.21)$$

and hence,

$$\frac{\partial \rho(x, t)}{\partial t} = 0. \quad (4.22)$$

Substitution of Eq. (4.22) into Eqs. (4.16) and (4.17) yields

$$\frac{\partial f_p(x_1, t)}{\partial t} = \frac{\partial f_p(x_2, t)}{\partial t} = \frac{d\bar{f}_p(t)}{dt} \quad (4.23)$$

and

$$\frac{dq_{int1}(t)}{dt} = -\frac{dq_{int2}(t)}{dt}. \quad (4.24)$$

Substitution of Eqs. (4.13) and (4.23) into Eqs. (4.14) and (4.15) yields

$$\frac{dq_e(t)}{dt} + \epsilon_p \frac{d\bar{f}_p(t)}{dt} = \frac{dq_{int1}(t)}{dt} = -\frac{dq_{int2}(t)}{dt}. \quad (4.25)$$

Equation (4.25) implies that in an ideal ACTFEL device  $\frac{d\bar{f}_p(t)}{dt} = 0$  when

$$\frac{dq_e(t)}{dt} = \frac{dq_{int1}(t)}{dt} = -\frac{dq_{int2}(t)}{dt}. \quad (4.26)$$

Equation (4.26) means, in conjunction with Eqs. (4.19) and (4.20), that in an ideal ACTFEL device, the insulator capacitance is equal to the measured dynamic capacitance when the internal current through the ACTFEL device phosphor layer is equal

to the external current in the circuit. In order for Eq. (4.26) to be valid, ACTFEL device phosphor-insulator interfaces must efficiently source electrons.

Equations (4.22) through (4.26) are still applicable to an ACTFEL device with  $\rho(x) \neq 0$  when  $\frac{\partial \rho(x,t)}{\partial t} = 0$ , i. e. when the phosphor space charge distribution is in steady state. The steady state may be achieved in many SrS-based ACTFEL devices, when a driving waveform with a long rise time (e. g. 200  $\mu\text{s}$ ) and sufficient voltage magnitude (e. g.  $V_{max} = V_{th} + 40$  V) is used (Fig. 4.2 (a)). When such driving waveform is used, the current density  $\frac{dq_e(t)}{dt}$  is constant in some SrS-based ACTFEL devices at the end of the rise time portion of the driving waveform. This constant portion of the  $i(t)$  curve at the end of the voltage pulse rise time is referred to as “steady-state  $i(t)$  portion” (Fig. 4.2 (d)). It is assumed here that during the time interval corresponding to the steady-state  $i(t)$  portion Eqs. (4.20) and (4.22) are satisfied so that dynamic  $C_i$  estimation can be accomplished using Eq. (4.19) provided that the phosphor-insulator interfaces efficiently source electrons.

A dynamic capacitance  $C_i$  estimate,  $C_i^{dyn}$ , can be obtained using the following procedure. The external charge transient,  $q_e(t)$  (Fig. 4.2 (a), curve 2), is measured and the current transient,  $i(t)$  (Fig. 4.2 (d)), is calculated. Then, the  $C_i^{dyn}$  estimate is calculated using Eq. (4.19) for the time interval corresponding to the steady-state  $i(t)$  portion (Fig. 4.2 (d)). In order to obtain a well-defined steady-state  $i(t)$  portion, the voltage pulse must have a long enough rise time (e. g. 200  $\mu\text{s}$ ) and a large enough magnitude (e. g.  $V_{max} = V_{th} + 40$  V). When the rise time portion of the driving waveform is much larger than the circuit  $RC$  time constant, the driving waveform is less distorted by the RC effects and is less sensitive to the value of the current-limiting series resistor. The large  $V_{max}$  is necessary to provide enough applied voltage pulse rise time at  $v_g(t) > V_{to}$  so that the steady state can be established.

To validate this dynamic capacitance  $C_i$  estimation procedure,  $C_i^{dyn}$  values are obtained for several ACTFEL devices using different applied voltage pulse polarities and magnitudes. For each ACTFEL device measured, a 95%-confidence interval is obtained for  $C_i^{dyn}$  values. The results of this validation are discussed in Sec. 4.1.3.

**Table 4.1.** Summary of the insulator capacitance estimation

#	Phosphor type	$C_i^{stat}$ (nF/cm <sup>2</sup> )	$C_i^{dyn}$ (nF/cm <sup>2</sup> )	$C_i^{phys}$ (nF/cm <sup>2</sup> )	Overshoot (%)
1	SrS:Ce	14.9 ± 0.9	14.3 ± 0.7	17.7	0
2	SrS:Ce	35 ± 3	30.9 ± 0.7	29	270 ± 70
3	SrS:Ce	38 ± 1	29 ± 1	29	1600 ± 900
4	SrS:Ce	41 ± 2	34 ± 1	29	900 ± 500
5	SrS:Cu	23 ± 2	32 ± 1	25	39 ± 15
6	SrS:Cu	21 ± 2	27.3 ± 0.7	25	38 ± 9
7	SrS:Cu	15 ± 2	22.7 ± 0.8	25	44 ± 15

### 4.1.3 Comparison of the two methods of insulator capacitance estimation

In this section, the two methods of  $C_i$  estimation are used to assess the insulator capacitance in three SrS:Cu and four SrS:Ce ACTFEL devices. These  $C_i$  estimates are compared to each other and to  $C_i$  estimates provided by the ACTFEL device fabricator ( $C_i^{phys}$ ). The results of these measurements are summarized in Table 4.1 and Figs. 4.2 and 4.3. The  $C - V$  overshoot in Table 4.1 is calculated as  $\frac{C_{max} - C_i^{dyn}}{C_i^{dyn}}$ , where  $C_{max}$  is the maximum dynamic capacitance averaged over several measurements at different maximum applied voltages and voltage pulse polarities.

The SrS:Ce ACTFEL device 1 (Table 4.1) is fabricated at OSU by electron-beam deposition. It has half of the glass substrate area with no phosphor layer, which allows a direct measurement of  $C_i$ .  $C_i^{phys}$ , therefore, presents the most reliable  $C_i$  estimate for this ACTFEL device. This SrS:Ce ACTFEL device, unlike most other SrS:Ce ACTFEL devices, exhibits a negligible amount of capacitance overshoot.  $C_i^{stat}$  and  $C_i^{dyn}$  for the ACTFEL device 1 (Table 4.1) are approximately equal to each other and  $\sim 12\%$  smaller than  $C_i^{phys}$ . Deviation of the two  $C_i$  estimates from the ACTFEL

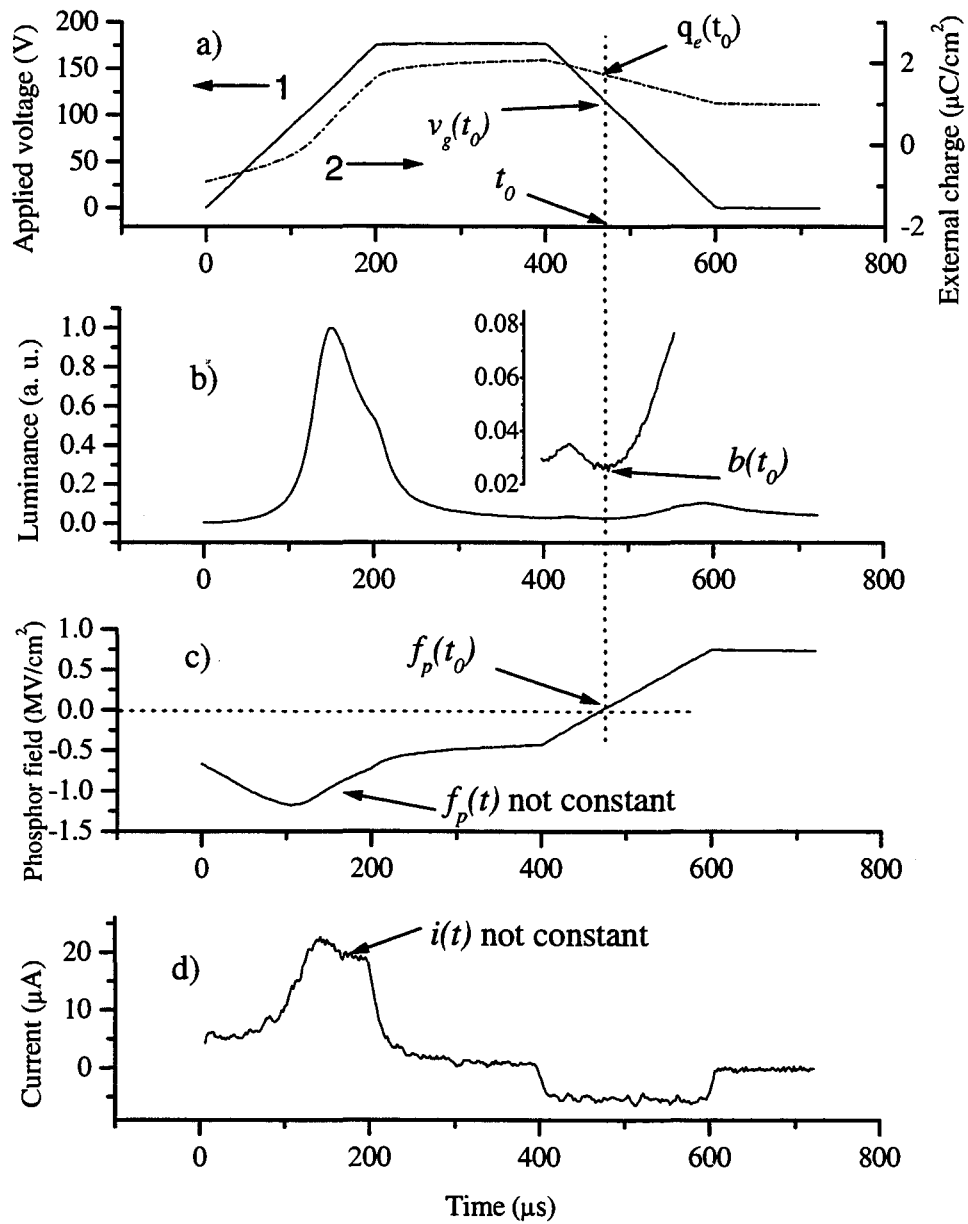


**Figure 4.3.** (a) Long voltage pulse waveform (curve 1) and external charge transient (curve 2), (b) luminance transient plot, (c) phosphor field transient plot calculated using the  $C_i^{stat}$  estimate, and (d) current transient plot for a SrS:Cu ACTFEL device.

device physical insulator capacitance can be partially attributed to a small reduction of the ACTFEL device active area due to self-healing breakdown. This result shows that both dynamic and static capacitance  $C_i$  estimation procedures can produce relatively accurate  $C_i$  estimates.

SrS:Ce ACTFEL devices 2-4 (Table 4.1) are fabricated at Planar America by ALE. For these devices, the measured current transients (Fig. 4.2 (d)) have a well-defined  $i(t)$  steady-state portion and the dynamic  $C_i$  estimates differ by only 4% from the  $C_i^{phys}$  estimates. Therefore, dynamic capacitance  $C_i$  estimates for these ACTFEL devices appear to be more reliable than static capacitance  $C_i$  estimates. The static capacitance  $C_i$  estimates in these ACTFEL devices are  $\sim 30\%$  larger than the dynamic capacitance  $C_i$  estimates. If  $C_i^{stat}$  is larger than the actual  $C_i$ , the minimum luminance transient does not accurately correspond to a situation in which the average field is zero (Fig. 4.2 (c)). Note that these SrS:Ce ACTFEL devices have large capacitance overshoot.

SrS:Cu ACTFEL devices 4-6 (Table 4.1) are fabricated at State University of New York in Albany by MOCVD. In these SrS:Cu ACTFEL devices,  $C_i^{dyn}$  assessment is difficult since a distinct steady-state  $i(t)$  portion is not obtained in these ACTFEL devices (Fig. 4.3 (d)). Also,  $C_i^{stat}$  estimation is problematic since the luminance transient is rather weak during the fall time portion of the applied voltage waveform so that it is hard to accurately determine  $b(t_0)$ . Difficulties with  $C_i^{dyn}$  and  $C_i^{stat}$  assessment may be related to the fact that these SrS:Cu ACTFEL devices have a small capacitance overshoot and conduct less current than SrS:Ce ACTFEL devices. Therefore,  $C_i^{stat}$  estimates for the SrS:Cu ACTFEL devices measured appear to be about as reliable as  $C_i^{dyn}$  estimates.

#### 4.1.4 Summary

This section introduces two methods for the insulator capacitance estimation of ACTFEL devices with dynamic space charge. In the static capacitance method,  $C_i$  is estimated as a static capacitance at a time  $t_0$  corresponding to when the phosphor field is zero. In the dynamic capacitance method,  $C_i$  is estimated as a dynamic capacitance

at the end of a voltage pulse rise time, provided that the voltage pulse rise time and the voltage magnitude are large enough to produce a constant steady-state current transient. The accuracy of these  $C_i$  estimation methods appears to be similar and both techniques appear to be more reliable when more charge is transported across the phosphor.

## 4.2 Simulation of electrical characteristics of SrS:Ce ACTFEL devices using a two-sheet space charge model

The purpose of this section is to use the two-sheet space charge model to simulate the electrical characteristics of SrS:Ce ACTFEL devices and to compare experimental measurements to simulated curves.

### 4.2.1 *Experimental procedure*

To assess the viability of the two-sheet space-charge model, experimental  $C - V$  and  $Q_{int} - F_p$  characteristics of a SrS:Ce ACTFEL device are measured. Then, simulated curves are generated by fitting to the experimental data using a design of experiment (DOE) methodology for parameter optimization.

A SrS:Ce ACTFEL device, obtained from Planar America, Inc., is used for experimental measurements. The basic parameters of this device are shown in Table 4.2. To stabilize the performance of the device for measurements, it is preliminarily aged for more than one day with a bipolar trapezoidal voltage waveform with rise, hold, and fall time portions of  $5 \mu\text{s}$ ,  $30 \mu\text{s}$ , and  $5 \mu\text{s}$ , respectively, at frequency of 1 kHz.

The experimental device characteristics being simulated are  $C - V$  and  $Q_{int} - F_p$  curves, measured using techniques described in Sec. 3.2.3.

For both the measurement and the simulation, a bipolar trapezoidal voltage waveform with  $200 \mu\text{s}$  rise, hold, and fall time portions of the pulse at a frequency of 100 Hz is used to drive the device. This pulse shape, with relatively long voltage pulses, provides a small slew rate during the rise and fall time portions of the pulse to

**Table 4.2.** The device specifications for two-sheet space-charge modeling.

Sample composition		SrS:Ce
Phosphor deposition method		ALE
Phosphor thickness	Å	7569
Physical total capacitance ( $C_t$ )	nF/cm <sup>2</sup>	9.3
Physical insulator capacitance ( $C_i$ )	nF/cm <sup>2</sup>	28.5
Active device area	cm <sup>2</sup>	0.079
Electron effective mass		$0.53m_0$ [28]

minimize pulse distortion due to series resistance and amplifier artifacts, and allows the recombination time constant at the interfaces to be neglected.

The simulation results are obtained from a numerical solution of Eqs. (2.11) through (2.13) realized in the  $C$  programming language with a fourth/fifth order Runge-Kutta-Fehlberg algorithm using a Hewlett-Packard 9000 type computer.

## 4.2.2 Results and discussion

### 4.2.2.1 Screening DOE results

A quarter fraction screening DOE procedure is employed to study the effects of six parameters of the two-sheet space charge model on the shape of the simulated curves. These parameters, called also “control factors”, are listed in Table 4.3 along with their low and high values used for the DOE procedure. Other parameters of the model affecting the shape of the simulated curves (applied voltage pulse shape, magnitude, frequency, device active area, phosphor and insulator thicknesses, phosphor and insulator dielectric permittivities, and SrS electron effective mass) are either controlled experimentally or known for a given ACTFEL device, and are kept invariant in this DOE procedure.

**Table 4.3.** Control factors for the two-sheet space charge model screening DOE.

Factors	Description	Units	Low	High
$E_{sc}$	space charge trap depth	eV	0.9	1.2
$E_{it}$	phosphor-insulator interface trap depth	eV	0.9	1.2
$\sigma$	capture cross-section for thermal emission (for both space charge and phosphor-insulator interfaces)	cm <sup>2</sup>	$1 \times 10^{-21}$	$1 \times 10^{-16}$
$N_0 f_0^{it}$	no-field occupancy of phosphor-insulator interface traps	cm <sup>-2</sup>	$1 \times 10^{13}$	$5 \times 10^{13}$
$N_0 f_0^{sc1} = N_0 f_0^{sc2}$	no-field occupancy of bulk traps	cm <sup>-2</sup>	$1 \times 10^{13}$	$1 \times 10^{17}$
$d_{sc1} = d_p - d_{sc2}$	location of the space charge sheets	Å	50	2000

**Table 4.4.** Response variables for the two-sheet space-charge model screening DOE.

Variables	Description
$V_{to}$	turn-on voltage
$C_{max}$	maximum dynamic capacitance
$Q_{int}^{max}$	maximum internal charge
$F_p^{max}$	maximum phosphor field
$F_p^{Vmax}$	steady-state phosphor field
$Q_{int}^{leak}$	internal leakage charge
$Q_{int}^{relax}$	internal relaxation charge

**Table 4.5.** Results of the screening DOE.

	$Q_{int}^{max}$	$F_p^{V_{max}}$	$F_p^{max}$	$Q_{int}^{leak}$	$Q_{int}^{relax}$	$C_{max}$	$V_{to}$
	$\mu\text{C}/\text{cm}^2$	$\text{MV}/\text{cm}$	$\text{MV}/\text{cm}$	$\mu\text{C}/\text{cm}^2$	$\mu\text{C}/\text{cm}^2$	$\text{nF}/\text{cm}^2$	$\text{V}$
$E_{it}$	-0.19	0.04	0.14	0.30	-0.07	2.6	30
$E_{sc}$	-1.39	0.40	0.38	-0.40	-0.14	-3.5	60
$\sigma$	1.32	-0.38	-0.37	0.22	0.12	0.9	-54
$N_0 f_0^{it}$	1.05	-0.23	-0.11	0.34	0.32	-0.4	-26
$N_0 f_0^{sc}$	0.70	-0.13	0.01	-0.06	0.29	4.4	-19
$d_{sc}$	-0.19	0.11	0.09	-0.10	0.15	-4.3	0.9

The shape of the simulated curves is characterized by the seven response variables listed in Table 4.4.  $V_{to}$  is determined from the simulated  $C - V$  curves as the value of the applied voltage,  $v_g(t)$ , at which the ACTFEL device dynamic capacitance reaches approximately  $1.5 C_t$  (15 nF/cm<sup>2</sup>).  $C_{max}$  is determined as the peak value of the simulated  $C - V$  curve.  $Q_{int}^{max}$  is determined from the  $Q_{int} - F_p$  plots as the maximum absolute value of internal charge reached during either positive or negative pulse of the driving waveform ( $|Q(D)|$  or  $|Q(I)|$ , Fig. 2.2).  $F_p^{max}$  is determined from the  $Q_{int} - F_p$  plots as the phosphor field at the onset of charge transfer through the phosphor layer during the rise time portion of the driving waveform ( $|Q(B)|$  or  $|Q(G)|$ , Fig. 2.2).  $F_p^{V_{max}}$  is determined as the phosphor field at the beginning of the hold time portion of the pulse ( $|F(C)|$  or  $|F(H)|$ , Fig. 2.2).  $Q_{int}^{leak}$  is determined as the charge “leaking” from the anodic interface during the interpulse interval ( $|Q(E) - Q(F)|$  or  $|Q(J) - Q(A)|$ , Fig. 2.2).  $Q_{int}^{relax}$  is determined as the charge transferred through the phosphor layer during the hold time portion of the pulse ( $|Q(D) - Q(C)|$  or  $|Q(I) - Q(H)|$ , Fig. 2.2).

The results of this screening DOE are presented in Table 4.5, showing the estimated effects of each control factor on each response variable. These estimated effects represent the average variation of a response variable in the corresponding

column of Table 4.5 as the control factor in the corresponding row changes from its low to high value (Table 4.3). The factor interactions could not be reliably estimated by this quarter-fraction screening DOE procedure and, thus, are not included in Table 4.5.

Table 4.5 shows that the largest estimated effects for the most important characteristics of a  $Q_{int} - F_p$  curve,  $Q_{int}^{max}$ ,  $F_p^{max}$ ,  $F_p^{Vmax}$  and  $Q_{int}^{leak}$  are those of two factors,  $E_{sc}$  and  $\sigma$ . Increasing the bulk trap depth significantly reduces the amount of transferred charge and increases  $F_p^{max}$  and  $F_p^{Vmax}$ . On the contrary, increasing the thermal capture cross-section significantly increases the amount of transferred charge and reduces  $F_p^{max}$  and  $F_p^{Vmax}$  at  $T = 300$  K.

Table 4.5 shows that  $C_{max}$  is affected primarily by the space charge parameters  $N_0 f_0^{sc}$ ,  $d_{sc}$ , and  $E_{sc}$ , confirming the conclusion made in [54] that the dynamic capacitance overshoot is due to space charge effects. The negative estimated effect of  $d_{sc}$  on  $C_{max}$  is also consistent with an important conclusion made in [54] that the dynamic capacitance overshoot is larger when more of the space charge is created near the phosphor-insulator interfaces. Table 4.5 shows that none of the control factors used in this DOE procedure has an estimated effect on  $C_{max}$  larger than  $5 \text{ nF/cm}^2$ , implying that the two sheet space charge model in its present realization is unable to produce the dynamic capacitance overshoot of  $\sim 30 \text{ nF/cm}^2$  observed experimentally in SrS:Ce ACTFEL devices. As  $C_{max}$  is affected mostly by the space charge parameters, it is expected that adding the impact ionization space charge creation mechanism to the model, in a similar manner as how it was employed in the single-sheet space charge model [2], will improve the fit of the simulated dynamic capacitance overshoot to the experimental data.

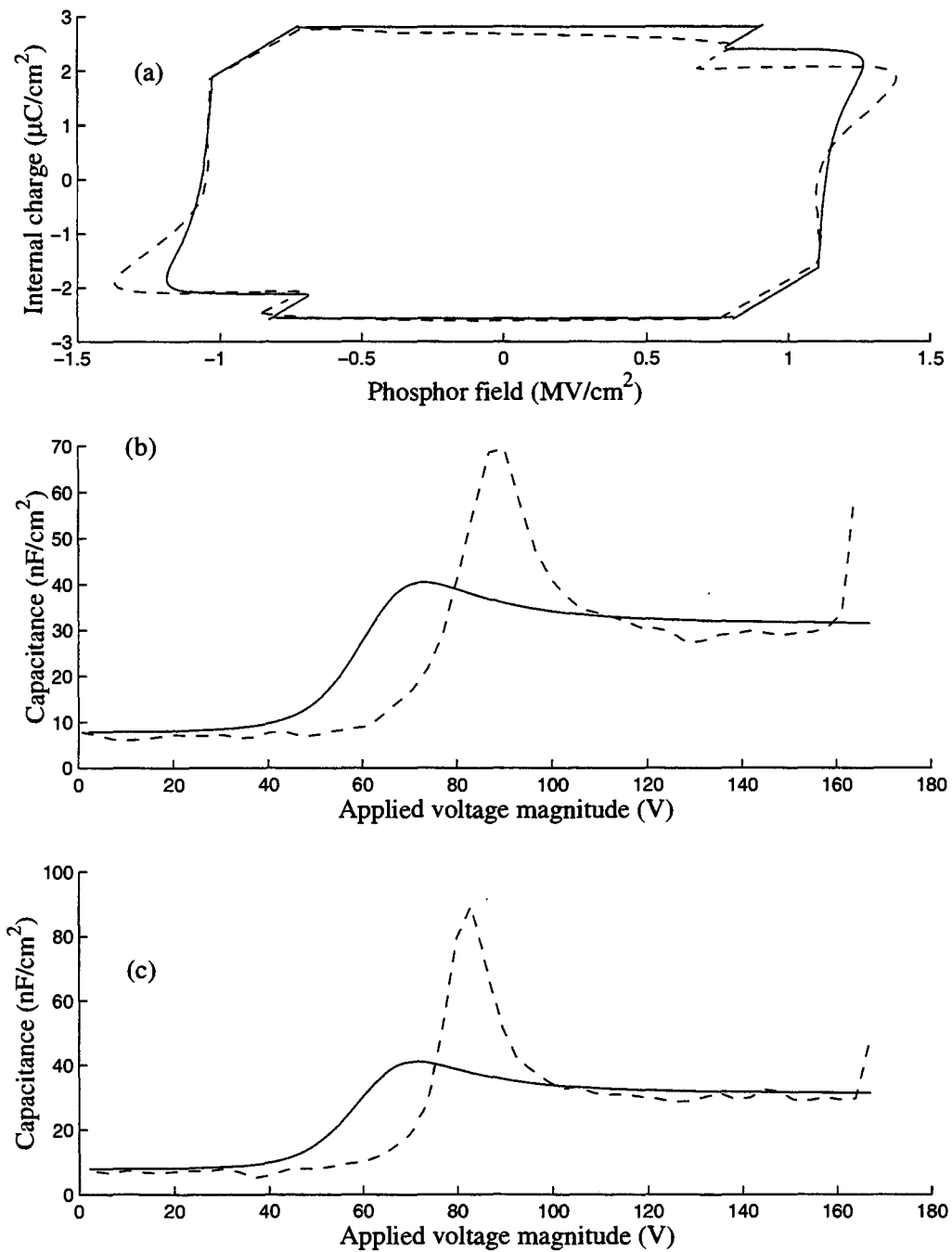
Data from Table 4.5 are used in Section 4.2.2.2 as a basis for a set of response surface DOE procedures to optimize the simulation parameters for the best fit of the simulated  $Q_{int} - F_p$  curves to the SrS:Ce ACTFEL device experimental data.

**Table 4.6.** The optimized two-sheet space-charge simulation parameters.

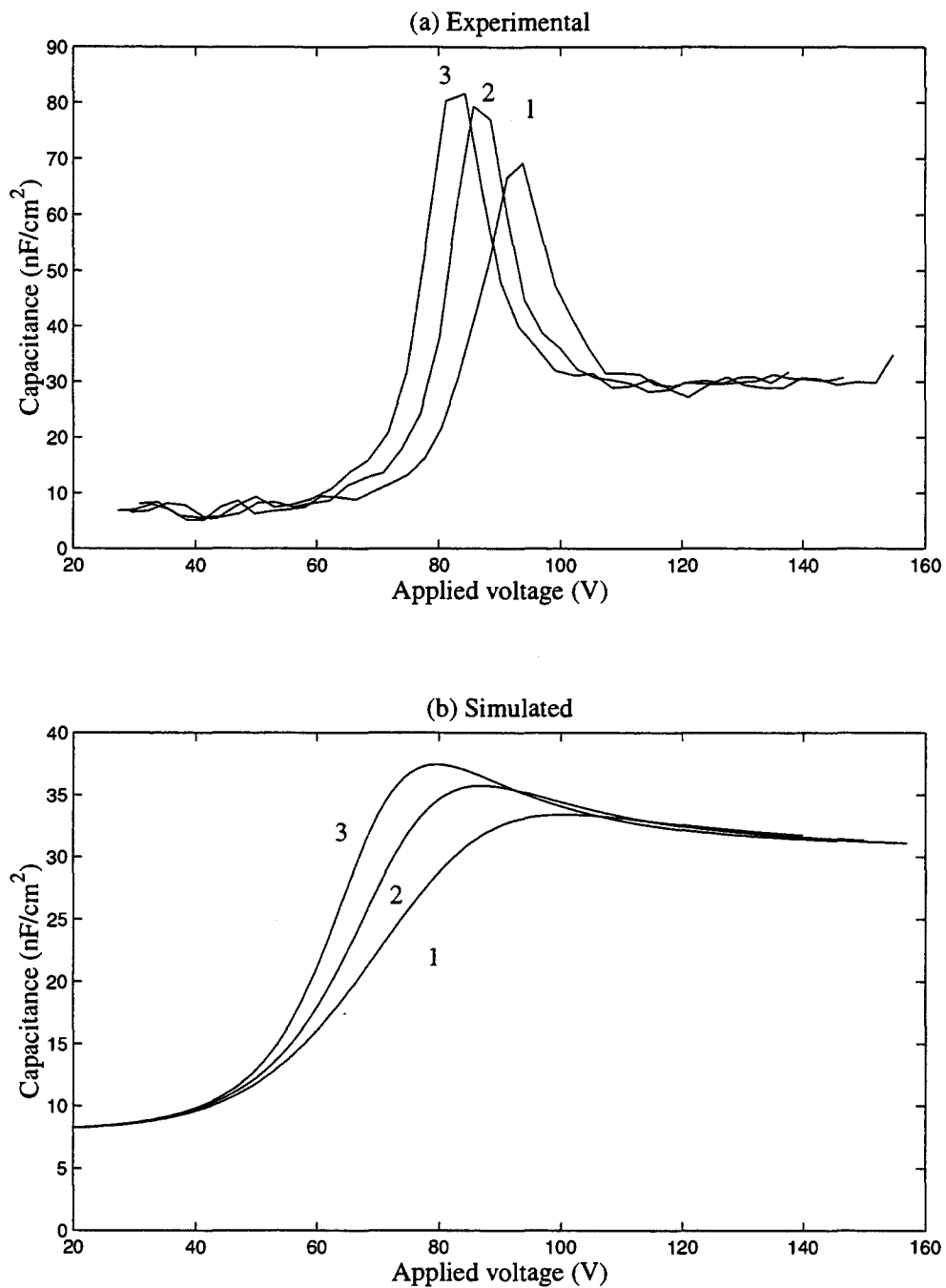
Parameter	Description	Units	Values
$N_0 f_0^{it}$	no-field occupancy of interface traps	$\text{cm}^{-2}$	$5 \times 10^{13}$
$N_0 f_0^{sc1}$	no-field occupancy of bulk traps (sheet 1)	$\text{cm}^{-2}$	$5 \times 10^{13}$
$N_0 f_0^{sc2}$	no-field occupancy of bulk traps (sheet 2)	$\text{cm}^{-2}$	$2 \times 10^{13}$
$d_{sc1} = d_p - d_{sc2}$	location of the space charge sheets	$\text{\AA}$	50
$E_{it}$	interface trap depth	eV	1.5
$E_{sc}$	bulk trap depth	eV	0.76
$\sigma$	capture cross-section for thermal emission	$\text{cm}^2$	$1 \times 10^{-21}$

#### 4.2.2.2 Fitting of SrS:Ce simulated curves to experimental data

The fit of the simulated  $Q_{int} - F_p$  curve to the experimental  $Q_{int} - F_p$  data of the SrS:Ce ACTFEL device using the simulation parameters listed in Table 4.6 is shown in Fig. 4.4. To increase the simulated  $V_{to}$ ,  $\sigma$  is set to its low value from Table 4.3. The simulated values of  $F_p^{V_{max}}$  and  $Q_{int}^{max}$  are adjusted to correspond to their experimental values by variation of  $E_{sc}$  using response surface plots obtained in the *StatGraphics* software package. Finally, the simulated  $Q_{int} - F_p$  curve shape is fit to the experimental data by changing the rest of the screening DOE control factors. A relatively large  $E_{it}$  of 1.5 eV is used to increase the simulated  $V_{to}$  and  $C_{max}$ . To increase the simulated  $C_{max}$ ,  $d_{sc}$  is set to its low value from Table 4.3. The extremely small value for  $d_{sc}$  (50  $\text{\AA}$ ) is used to show that the two-sheet space-charge model involving field-assisted emission of electrons as the only mechanism of space-charge generation fails to explain the large capacitance and phosphor field overshoot observed in SrS:Ce ACTFEL devices, no matter how freely the simulation parameters are chosen. A slight difference between trap occupancy values for the two space charge sheets accounts for an asymmetry of the experimental  $Q_{int} - F_p$  curve with respect to the applied voltage polarity. All other simulation parameters are kept constant throughout the fitting procedure.



**Figure 4.4.** Simulated (solid line) and experimental (dashed line)  $Q_{int} - F_p$  (a) and  $C - V$  (b, c) curves of SrS:Ce ACTFEL device. (b) – for positive, (c) – for negative applied voltage pulse.



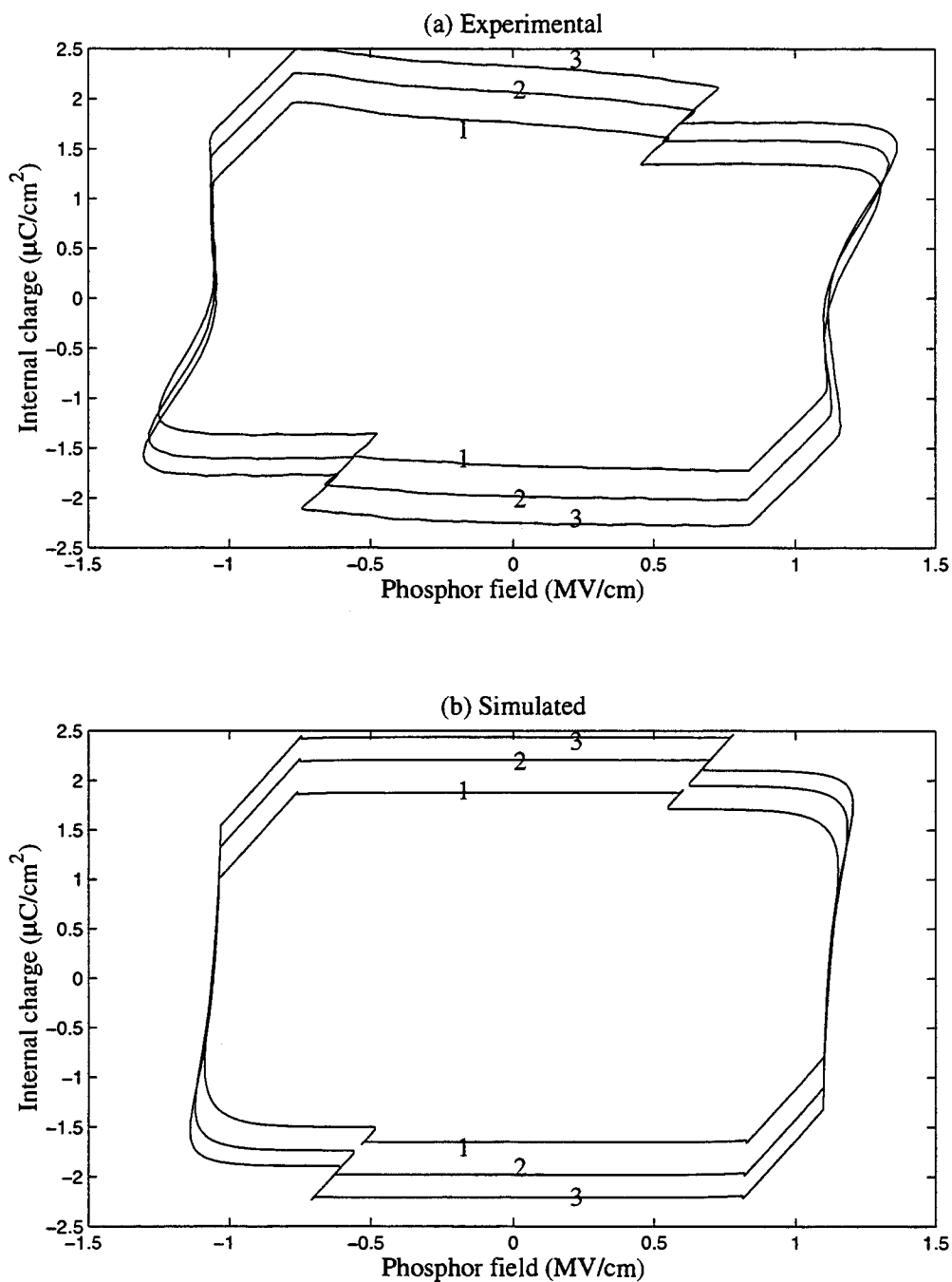
**Figure 4.5.** Experimental (a) and simulated (b)  $C - V$  curves for SrS:Ce ACTFEL device at variable applied signal magnitude measured for a positive applied voltage pulse. 1 -  $V_{max} = 140$  V, 2 -  $V_{max} = 150$  V, 3 -  $V_{max} = 157$  V.

Figure 4.4 shows that the two-sheet space charge model allows realistic simulation of  $Q_{int} - F_p$  curves for SrS:Ce ACTFEL devices with a deviation of simulated  $Q_{int}^{max}$ ,  $Q_{int}^{leak}$ ,  $Q_{int}^{relax}$ , and  $F_p^{Vmax}$  from experimental values of less than 4%. As shown in Fig. 4.6 and Fig. 4.5, there is also good agreement between simulated and experimental  $Q_{int} - F_p$  and  $C - V$  trends when the maximum applied voltage is varied, with all other simulation parameters fixed.

Some of the simulated characteristics of the  $Q_{int} - F_p$  curve shown in Fig. 4.4, however, disagree with experimental data for the SrS:Ce ACTFEL device. The turn-on voltage ( $V_{to}$ ) and dynamic capacitance overshoot ( $C_{max}$ ) are more than 30% smaller than the experimental values for the SrS:Ce ACTFEL device, no matter how freely the simulation parameters are chosen, which is consistent with the screening DOE results presented in Section 4.2.2.1. The two-sheet space charge model is also unable to explain “charge collapse”, defined as an abrupt decrease in the internal charge during the fall time portion of the applied voltage pulse, which is initiated in the experimental data concomitant with the applied voltage decrease. A noticeable amount of charge collapse is present in the experimental  $Q_{int} - F_p$  curves shown in Fig. 4.6; this is evident from the negative slope of the uppermost portion of the  $Q_{int} - F_p$  curves shown in Fig. 4.6 (a). Attempts to simulate  $Q_{int} - F_p$  characteristics of the same device using a “short” voltage pulse waveform with 5  $\mu s$  rise, 30  $\mu s$  fall, and 5  $\mu s$  fall time portions was unsuccessful. Experimental dynamic capacitance overshoot and phosphor field overshoot observed in a SrS:Ce ACTFEL device driven with a “short” waveform is much larger than when the device is driven with a “long” waveform. The most probable reason for this is that current through the ACTFEL device is much larger for driving waveforms with shorter rise and fall time portions. Large current facilitates impact ionization of bulk impurities not included in the space-charge model used for these simulations.

### 4.2.3 Summary

It has been shown by fitting simulated  $C - V$  and  $Q_{int} - F_p$  curves to experimental data that the two-sheet space charge model allows for realistic simulation of  $Q_{int} - F_p$



**Figure 4.6.** Experimental (a) and simulated (b)  $Q_{int}-F_p$  curves for SrS:Ce ACTFEL device at variable applied signal magnitude. 1 -  $V_{max} = 140$  V, 2 -  $V_{max} = 150$  V, 3 -  $V_{max} = 157$  V.

curves for SrS:Ce ACTFEL devices with accurate values of  $Q_{int}^{max}$ ,  $Q_{int}^{leak}$ ,  $Q_{int}^{relax}$ , and  $F_p^{Vmax}$ .

In its present realization, however, the two-sheet space charge model fails to explain the large experimental phosphor field overshoot, experimental turn-on voltage, and capacitance overshoot that is observed in SrS:Ce ACTFEL devices.

Using a DOE methodology, it has been shown that the values of maximum internal charge, turn-on phosphor field, and steady-state phosphor field obtained by the two-sheet space charge model simulation all depend primarily on the space charge parameters — bulk trap depth and space charge thermal capture cross-section.

The screening DOE procedure confirms conclusions obtained from the single-sheet space charge model [54], that the dynamic space charge is responsible for the capacitance overshoot observed experimentally in ACTFEL devices and that the capacitance overshoot is larger when most of the space charge is created near the phosphor-insulator interfaces.

### 4.3 Electro-optical characterization of SrS:Ce, SrS:Cu, and SrS:Cu,Ag ACTFEL devices

The purpose of this section is to compare the electro-optical performance of ACTFEL devices with SrS phosphor layers doped with three types of impurities – Ce, Cu, and (Cu, Ag). Technology for SrS:Ce ACTFEL device fabrication is well established. SrS:Ce ACTFEL devices have good luminance and efficiency. However, the color of SrS:Ce luminescence needs to be improved for use as a blue phosphor in full-color displays. SrS:Cu and SrS:Cu,Ag ACTFEL device luminescence has better blue CIE color coordinates than those of SrS:Ce luminescence. However, the technology for SrS:Cu and SrS:Cu,Ag ACTFEL device fabrication is still under development. Luminance, efficiency, and longevity of SrS:Cu and SrS:Cu,Ag ACTFEL devices still need to be improved in order to use these phosphors in commercial displays.  $C - V$  and  $Q_{int} - F_p$  characteristics, as well as the dependence of maximum, polarization, leakage, and relaxation charges, luminance and luminous efficiency on the applied

**Table 4.7.** ACTFEL devices characterized

#	Phosphor type	Phosphor thickness (Å)	Phosphor deposition method	Phosphor manufacturer
1-6	SrS:Ce	~7800	ALE	Planar America
7-11	SrS:Cu	~10000	MOCVD	SUNY, Albany
12,13	SrS:Cu	~10000	Sputtering	Planar America
14,15	SrS:Cu,Ag	~10000	Sputtering	Planar America

voltage magnitude of SrS:Ce, SrS:Cu, and SrS:Cu,Ag ACTFEL devices are presented in this section.

Six SrS:Ce, seven SrS:Cu, and two SrS:Cu,Ag ACTFEL devices are used for this study. These ACTFEL devices are listed in Table 4.7.

#### 4.3.1 $Q_{int} - F_p$ characteristics

$Q_{int} - F_p$  plots are obtained using an applied voltage magnitude of about 40 V above the threshold voltage for each ACTFEL device studied. For ACTFEL devices with different threshold voltages, equal overvoltage allows for a reasonable comparison of the phosphor charge and phosphor field. An overvoltage of 40 V has been chosen for several reasons. First, 40 V above threshold is a small enough voltage to minimize ACTFEL device burn-out. Second, commercial ACTFEL devices usually operate at 40 V above threshold.

$Q_{int} - F_p$  plots are obtained using two types of bipolar trapezoidal driving waveform – one with “long” pulses having 200  $\mu$ s rise, hold, and fall time portions and the other with “short” pulses having 5  $\mu$ s rise and fall time portions and a 30  $\mu$ s hold time portion. The “long”-pulse waveform is used because it allows for a better estimate of the insulator capacitance of a SrS-based ACTFEL device than the “short”-pulse waveform (Sec. 4.1). The “short”-pulse waveform is traditionally used to drive com-

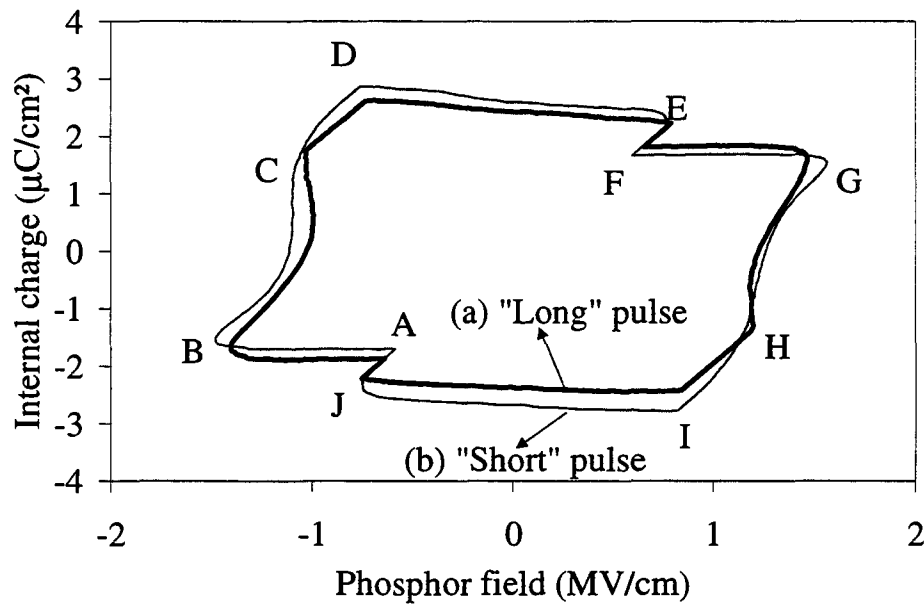


**Figure 4.7.** Internal charge versus phosphor field plots for a SrS:Ce ACTFEL device at  $V_{max} = V_{th} + 40$  V. (a) – using the “long”-pulse driving waveform, (b) – using the “short”-pulse driving waveform.

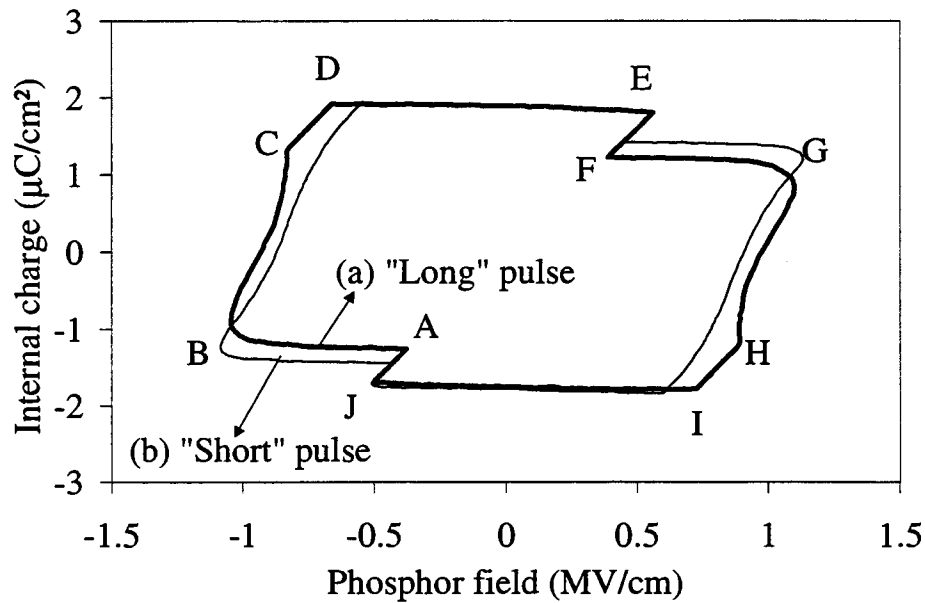
mercial ACTFEL devices, and thus, ACTFEL device characterization using this driving waveform is desirable. A frequency of 1000 Hz is used for the “short”-pulse driving waveform, whereas the “long”-pulse driving waveform frequency is 60 Hz.

Figure 4.7 shows  $Q_{int} - F_p$  plots measured at  $V_{max} = V_{th} + 40$  V for one of the SrS:Ce ACTFEL devices studied. A maximum phosphor field magnitude of 1.3–1.5 MV/cm is typical for all of the SrS:Ce ACTFEL devices studied. At the end of the rise time portion of the driving waveform (point C, Fig. 4.7), the phosphor field in the SrS:Ce ACTFEL devices studied is 1–1.2 MV/cm. Relaxation of the ACTFEL device phosphor field during the rise time portion of the driving waveform

is often referred to as “phosphor field overshoot”. Phosphor field overshoot is caused by electron multiplication in the phosphor layer during ACTFEL device operation. The multiplied electrons are driven by the field to the phosphor-insulator interface where they accumulate and reduce the phosphor field. Electron multiplication also creates positive space charge in the phosphor. Since its distribution changes during a single period of the driving waveform, this space charge is called “dynamic”. In the SrS:Ce ACTFEL devices studied, the maximum phosphor field is 30–40% larger than the phosphor field at the end of the rise time portion of the driving waveform. This phosphor field overshoot can be used to estimate the amount of dynamic space charge present in an ACTFEL device.

The maximum internal charge in SrS:Ce ACTFEL devices studied is 2.5 – 3.0  $\mu\text{C}/\text{cm}^2$ . This value is achieved at the end of the hold time portion of the driving waveform (points D and I, Fig. 4.7). During the fall time portion of the driving waveform, the internal charge in the SrS:Ce ACTFEL devices studied relaxes to 2.0–2.2  $\mu\text{C}/\text{cm}^2$ . This relaxation, common for most of the SrS:Ce ACTFEL devices studied, is referred to as “charge collapse”. Charge collapse and phosphor field overshoot in the SrS:Ce ACTFEL devices tested are larger for a positive than for a negative applied voltage pulse. The origin of the charge collapse is still unclear, but appears to be associated with the back injection of electrons from shallow trap states or with electrons present in the conduction band during the fall time portion of the applied voltage waveform.

There are some differences between the SrS:Ce ACTFEL device  $Q_{int} - F_p$  curves obtained using the “short” and the “long”-pulse driving waveform (Fig. 4.7 (a) and (b)). In particular, the maximum phosphor field, maximum internal charge, and the leakage charge (Sec. 3.2.3), are slightly larger when the “short”-pulse driving waveform is used. The dependence of the leakage charge on the driving waveform is interesting, because one might expect the opposite behavior of the leakage charge, since the “long”-pulse driving waveform at a frequency of 60 Hz has a longer interpulse pause than the “short”-pulse driving waveform at a frequency of 1 kHz. This dependence of the leakage charge on the driving waveform suggests that the leakage charge



**Figure 4.8.** Internal charge versus phosphor field plots for a SrS:Cu ACTFEL device at  $V_{max} = V_{th} + 40$  V. (a) – using the “long”-pulse driving waveform, (b) – using the “short”-pulse driving waveform.

in SrS:Ce ACTFEL devices depends on the applied voltage pulse duration more than on the duration of the interpulse pause. Because of the larger leakage charge, the polarization charge in SrS:Ce ACTFEL devices is smaller when the “short”-pulse driving waveform is used compared to that measured using the “long”-pulse driving waveform (Fig. 4.7).

Figure 4.8 shows  $Q_{int} - F_p$  plots measured at  $V_{max} = V_{th} + 40$  V for one of the SrS:Cu ACTFEL devices studied. Depending on the particular SrS:Cu ACTFEL device, the maximum phosphor field magnitude varies from 1 to 1.3 MV/cm when the “short”-pulse driving waveform is used and from 1 to 1.5 MV/cm when the

“long”-pulse driving waveform is used. The phosphor field overshoot for the SrS:Cu ACTFEL devices studied is less than 20%. The maximum internal charge measured at  $V_{max} = V_{th} + 40$  V varies, depending on the particular SrS:Cu ACTFEL device, from 1.3 to 1.9  $\mu\text{C}/\text{cm}^2$ . Charge collapse is negligible in the SrS:Cu ACTFEL devices studied.

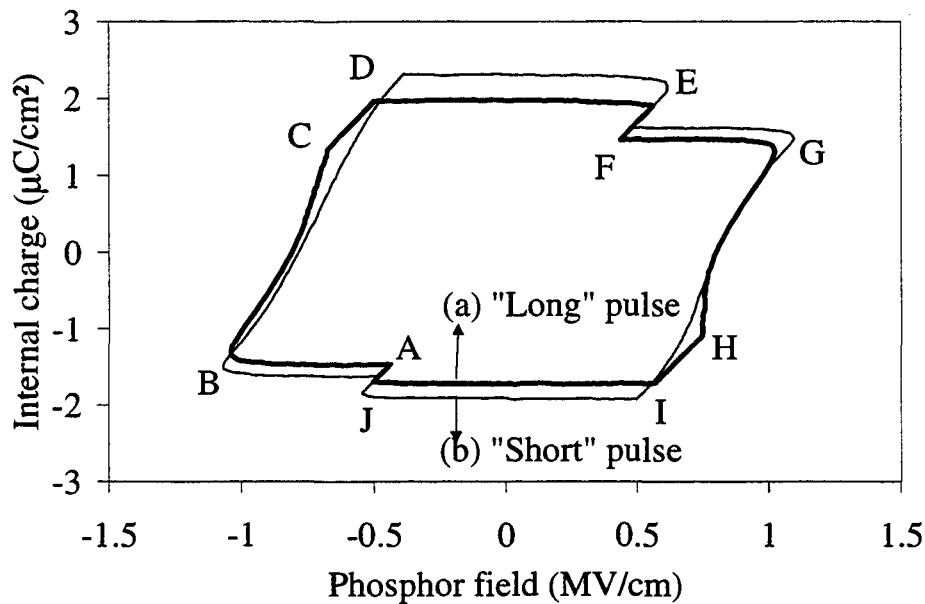
Figure 4.8 shows that when the “long”-pulse driving waveform at a frequency of 60 Hz is used, the leakage charge is larger than when the “short”-pulse driving waveform at a frequency of 1 kHz is used. This implies that the leakage charge in SrS:Cu ACTFEL devices depends mostly on the duration of the interpulse pause. This dependence of the leakage charge in SrS:Cu ACTFEL devices on the driving waveform is different from that observed in SrS:Ce ACTFEL devices.

Figure 4.9 shows  $Q_{int} - F_p$  plots for one of the SrS:Cu,Ag ACTFEL devices studied. At  $V_{max} = V_{th} + 40$  V, the maximum phosphor field magnitude in the SrS:Cu,Ag ACTFEL devices studied in this work is 0.9 to 1.1 MV/cm. The phosphor field overshoot in SrS:Cu,Ag ACTFEL devices is about 20–25%. The maximum internal charge in SrS:Cu,Ag ACTFEL devices is 1.8–2.3  $\mu\text{C}/\text{cm}^2$ . No charge collapse is found in SrS:Cu,Ag ACTFEL devices.

Comparing the  $Q_{int} - F_p$  plots measured using the “short” and the “long”-pulse driving waveform one notices that the maximum phosphor field and the maximum internal charge are larger when the “short”-pulse driving waveform is used.

### 4.3.2 $C - V$ characteristics

Figures 4.10 and 4.11 show  $C - V$  plots for a SrS:Ce, a SrS:Cu, and a SrS:Cu,Ag ACTFEL device measured using the “long”-pulse driving waveform with  $V_{max} = V_{th} + 40$  V for positive and negative applied voltage pulses, respectively. The feature of interest in these plots is the amount of  $C - V$  overshoot, which depends primarily on the ACTFEL device phosphor type and, thus, can be reasonably compared in the three ACTFEL devices. Other features of the  $C - V$  plots, like the turn-on voltage and the capacitance values, depend primarily on the thicknesses of the ACTFEL



**Figure 4.9.** Internal charge versus phosphor field plots for a SrS:Cu,Ag ACTFEL device at  $V_{max} = V_{th} + 40$  V. (a) – using the “long”-pulse driving waveform, (b) – using the “short”-pulse driving waveform.

device layers and other device-specific parameters, rather than on the phosphor type, and thus, cannot be reasonably compared in the ACTFEL devices measured.

Several observations can be made about the  $C - V$  overshoot in the ACTFEL devices studied. First, it is common for all SrS:Ce ACTFEL devices studied that the  $C - V$  overshoot is larger for a positive than for a negative pulse of the driving waveform. However, for the SrS:Cu,Ag ACTFEL tested, the  $C - V$  overshoot is larger for a negative than for a positive applied voltage pulse. No consistent asymmetry in  $C - V$  overshoot with respect to the applied voltage pulse polarity is observed for SrS:Cu ACTFEL devices. This asymmetry with respect to the applied voltage

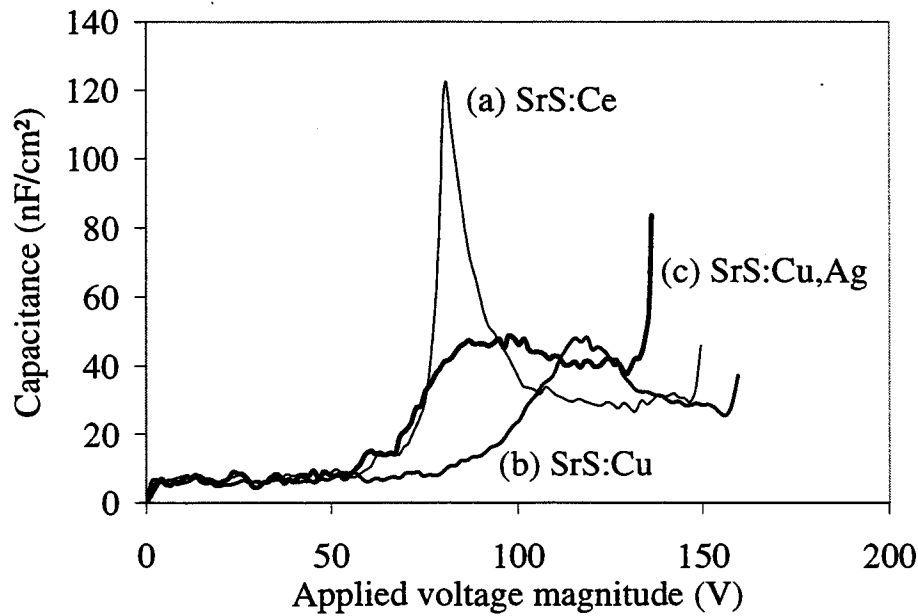


**Figure 4.10.** Capacitance versus applied voltage plots measured using a positive pulse of the “long”-pulse driving waveform with  $V_{max} = V_{th} + 40$  V. (a) – for a SrS:Ce ACTFEL device, (b) – for a SrS:Cu ACTFEL device, (c) – for a SrS:Cu,Ag ACTFEL device.

polarity, most probably, is due to the asymmetry of the two phosphor-insulator interfaces of the SrS:Ce and SrS:Cu,Ag ACTFEL devices. Second, for a positive pulse, the  $C - V$  overshoot in SrS:Ce ACTFEL devices is almost always larger than in SrS:Cu and SrS:Cu,Ag ACTFEL devices. For a negative pulse, the  $C - V$  overshoot for all ACTFEL devices tested has a similar order of magnitude. Third, the amount of  $C - V$  overshoot in a SrS:Cu ACTFEL device is very similar to that in a SrS:Cu,Ag ACTFEL device.

The capacitance of the SrS:Ce ACTFEL devices tested increases very abruptly at  $v_g(t) = V_{to}$ , especially for the positive applied voltage pulse. This abruptness

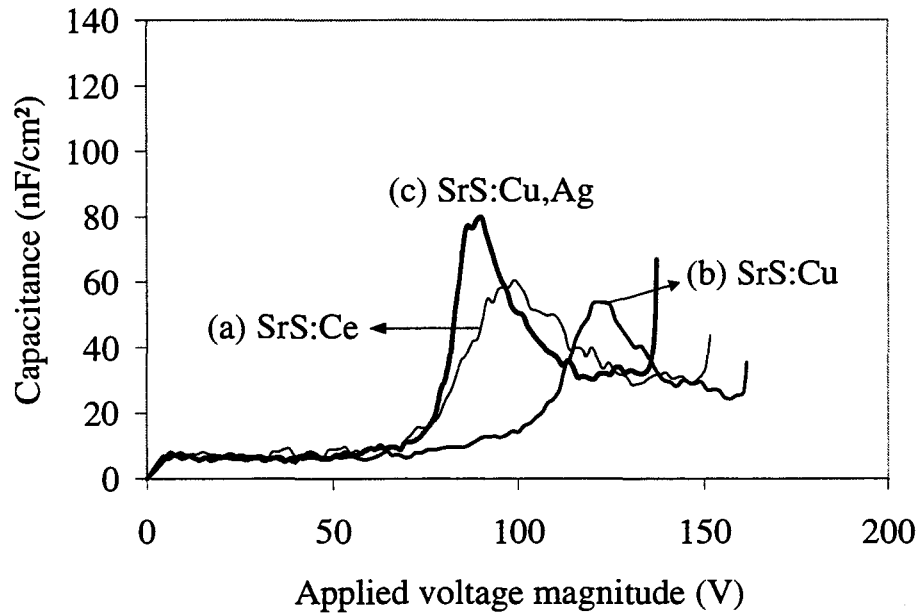


**Figure 4.11.** Capacitance versus applied voltage plots measured using a negative pulse of the “long”-pulse driving waveform with  $V_{max} = V_{th} + 40$  V. (a) – for a SrS:Ce ACTFEL device, (b) – for a SrS:Cu ACTFEL device, (c) – for a SrS:Cu,Ag ACTFEL device.

is caused by a large current flowing through the ACTFEL device at  $v_g(t) = V_{to}$ . The power supply fails to instantaneously supply the required amount of current, which leads to a “dip” in the slope of the rising  $v_g(t)$ . The capacitance increases dramatically because the large increase of the charge transferred through the ACTFEL device is associated with the decrease in the  $v_g(t)$  slope.

#### 4.3.3 $Q_{max} - V_{max}$ characteristics

Figure 4.12 shows maximum internal charge versus the maximum applied voltage curves measured for a positive applied voltage pulse for a SrS:Ce, a SrS:Cu, and a

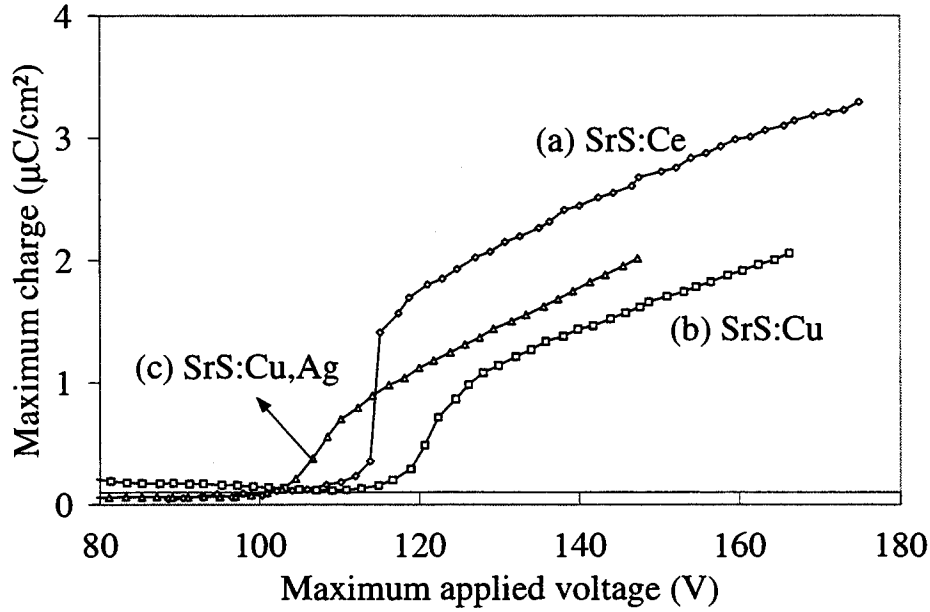


**Figure 4.12.** Maximum internal charge versus maximum applied voltage for a positive pulse of the “long”-pulse driving waveform. (a) – for a SrS:Ce ACTFEL device, (b) – for a SrS:Cu ACTFEL device, (c) – for a SrS:Cu,Ag ACTFEL device.

SrS:Cu,Ag ACTFEL device.  $Q_{max} - V_{max}$  curves measured using a negative applied voltage pulse are not shown, since these curves have similar trends. At  $V_{max} \ll V_{th}$ , the charge transferred through the ACTFEL device phosphor layer is essentially zero. At  $V_{max} \approx V_{th}$ , the maximum internal charge rapidly increases with increasing  $V_{max}$  in all of the ACTFEL devices tested. At  $V_{max} > V_{th}$ , the maximum internal charge keeps increasing linearly with increasing  $V_{max}$ , but the slope of the  $Q_{max} - V_{max}$  plot at  $V_{max} > V_{th}$  is smaller than near threshold.

The  $Q_{max} - V_{max}$  slope at  $V_{max} > V_{th}$  is approximately equal to the insulator capacitance for the ACTFEL devices measured. The most noticeable difference in the  $Q_{max} - V_{max}$  plots for the three ACTFEL devices is the  $Q_{max} - V_{max}$  slope at

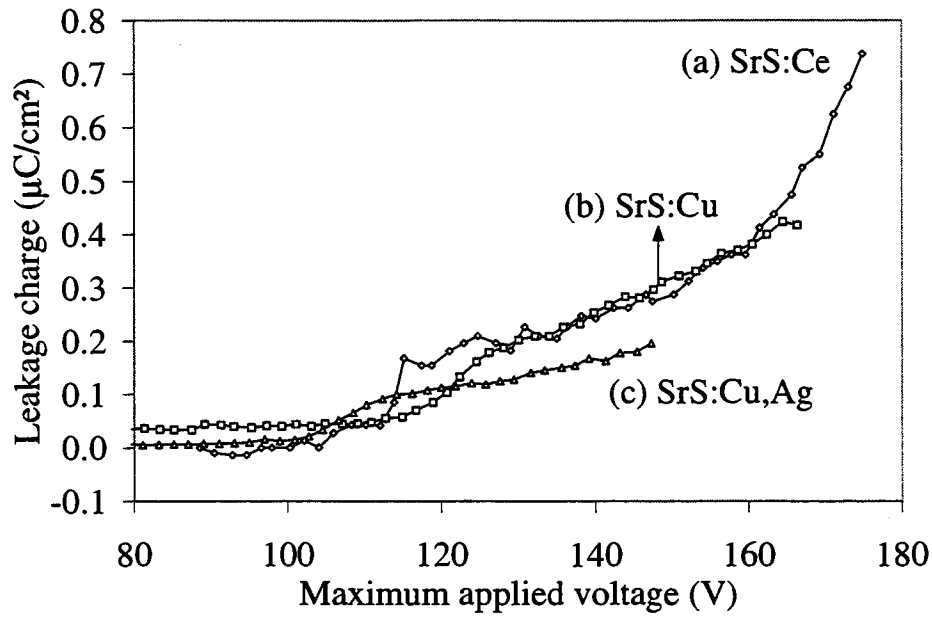


**Figure 4.13.** External leakage charge versus maximum applied voltage for a positive pulse of the “long”-pulse driving waveform. (a) – for a SrS:Ce ACTFEL device, (b) – for a SrS:Cu ACTFEL device, (c) – for a SrS:Cu,Ag ACTFEL device.

$V_{max} \approx V_{th}$ . SrS:Ce ACTFEL devices turn on very abruptly (Fig. 4.12 (a)), i. e.  $Q_{int}^{max}$  of a SrS:Ce ACTFEL device jumps by  $\sim 1.3 \mu\text{C}/\text{cm}^2$  over a change in  $V_{max}$  of less than 1 V. SrS:Cu and SrS:Cu,Ag ACTFEL devices turn on more gradually (Fig. 4.12 (b) and (c)), i. e.  $Q_{int}^{max}$  of these ACTFEL devices increase by  $\sim 0.7 \mu\text{C}/\text{cm}^2$  over a change of  $V_{max}$  of  $\sim 8$  V before the  $Q_{max} - V_{max}$  slope becomes constant.

#### 4.3.4 $Q_{leak} - V_{max}$ , $Q_{pol} - V_{max}$ , and $Q_{relax} - V_{max}$ characteristics

Figures 4.13 and 4.14 show, respectively, the leakage and the polarization charges plotted versus  $V_{max}$  for a SrS:Ce, a SrS:Cu, and a SrS:Cu,Ag ACTFEL device. At  $V_{max} < V_{th}$ , the leakage charge is zero in all of the ACTFEL devices measured in

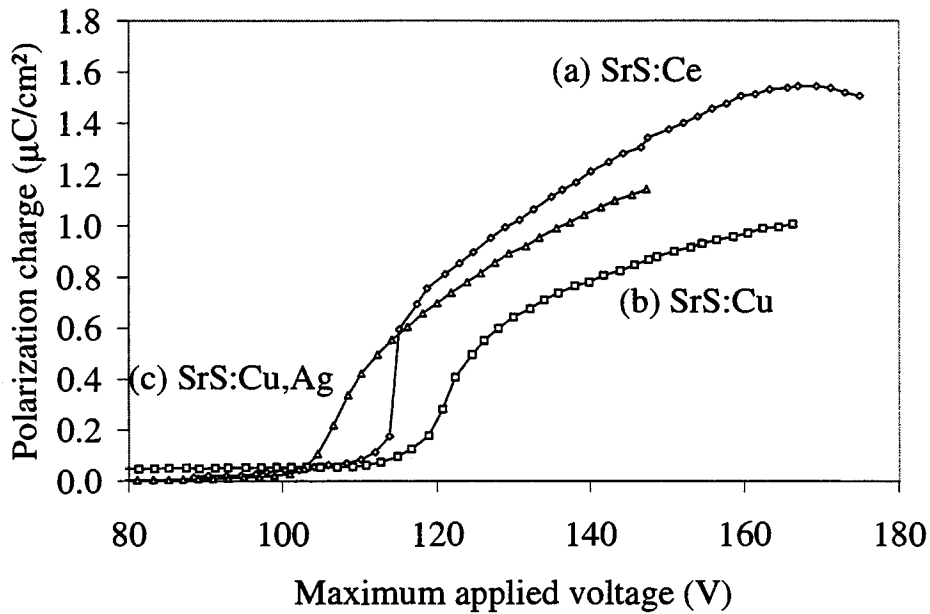


**Figure 4.14.** External polarization charge versus maximum applied voltage for a positive pulse of the “long”-pulse driving waveform. (a) – for a SrS:Ce ACTFEL device, (b) – for a SrS:Cu ACTFEL device, (c) – for a SrS:Cu,Ag ACTFEL device.

this work. At  $V_{max} > V_{th}$ , the leakage charge increases with increasing  $V_{max}$ . The rate at which the leakage charge increases above threshold is similar for all of the ACTFEL devices measured in this work. However, for SrS:Ce ACTFEL devices at  $V_{max} > V_{th} + 50$  V, the slope of the  $Q_{leak} - V_{max}$  plot (Fig. 4.13 (a)) increases significantly. This increase of the  $Q_{leak} - V_{max}$  slope is concomitant with an increase in the current transient at the end of the applied voltage pulse which is attributed to the back injection of electrons.

The shapes of the  $Q_{pol} - V_{max}$  plots shown in Fig. 4.14 are similar to those of the  $Q_{max} - V_{max}$  plots shown in Fig. 4.12. At  $V_{max} < V_{th}$ ,  $Q_{pol}$  is zero. At  $V_{max} \approx V_{th}$ ,  $Q_{pol}$

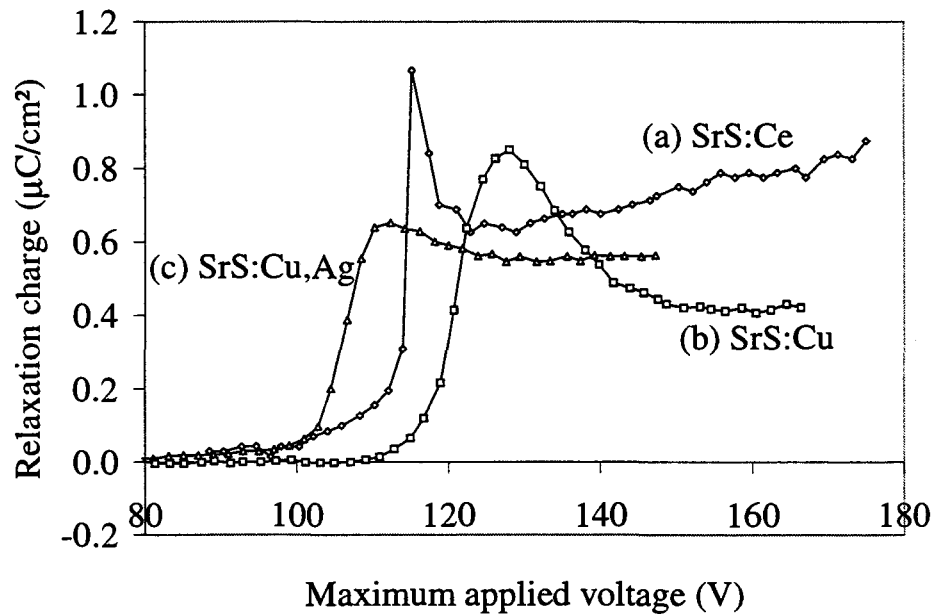


**Figure 4.15.** External relaxation charge versus maximum applied voltage for a positive pulse of the “long”-pulse driving waveform. (a) – for a SrS:Ce ACTFEL device, (b) – for a SrS:Cu ACTFEL device, (c) – for a SrS:Cu,Ag ACTFEL device.

rapidly increases with increasing  $V_{max}$ . As  $V_{max}$  increases above  $V_{th}$ ,  $Q_{pol}$  continues to increase. Similar to the  $Q_{max} - V_{max}$  curves in Fig. 4.12, the increase of  $Q_{pol}$  with increasing  $V_{max}$  at  $V_{max} \approx V_{th}$  is more abrupt in SrS:Ce than in SrS:Cu or SrS:Cu,Ag ACTFEL devices. The similarity between the shape of  $Q_{max} - V_{max}$  and  $Q_{pol} - V_{max}$  curves is not surprising, since an increase of the transferred charge causes an increase in  $Q_{pol}$ , and an increase in  $Q_{pol}$  facilitates an increase in the transferred charge by increasing the phosphor field at the beginning of each pulse.

There is a difference between the shapes of  $Q_{max} - V_{max}$  (Fig. 4.12) and  $Q_{pol} - V_{max}$  (Fig. 4.14) curves. The  $Q_{pol} - V_{max}$  slope gradually decreases with increasing  $V_{max}$

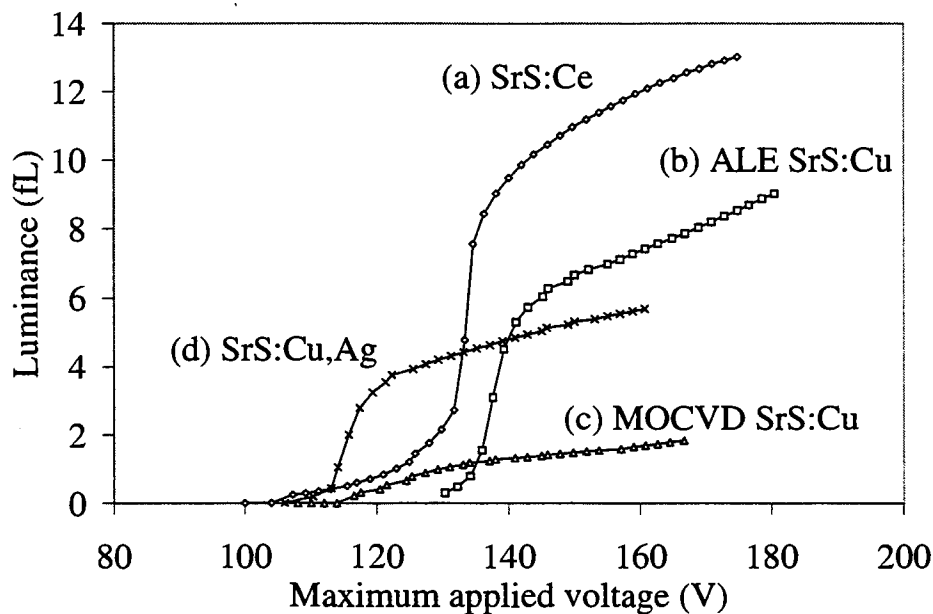
at  $V_{max} > V_{th}$ , while the  $Q_{max} - V_{max}$  slope is constant. For the SrS:Ce ACTFEL devices studied, at  $V_{max} > V_{th} + 50$  V,  $Q_{pol}$  decreases slightly with increasing  $V_{max}$ . The decrease of the  $Q_{pol} - V_{max}$  slope above threshold is attributed to a concomitant increase of the leakage charge.

Figure 4.15 shows the external relaxation charge plotted versus  $V_{max}$  for all types of ACTFEL devices studied. At  $V_{max} < V_{th}$ , the relaxation charge is zero. At  $V_{max} \approx V_{th}$ , the relaxation charge rapidly increases and reaches a maximum. Similar to  $Q_{max} - V_{max}$  and  $Q_{pol} - V_{max}$  trends,  $Q_{relax}$  increases abruptly in SrS:Ce ACTFEL devices and more gradually in SrS:Cu and SrS:Cu,Ag ACTFEL devices. At  $V_{max} > V_{th}$ , the relaxation charge drops and then changes very little as  $V_{max}$  increases. A maximum is observed in the  $Q_{relax} - V_{max}$  plots because at  $V_{max} \approx V_{th}$ ,  $V_{to} \approx V_{max}$ , so that most of the charge transfer through the ACTFEL device phosphor layer takes place during the hold time portion of the applied voltage pulse. When  $V_{max} > V_{th}$ , the relaxation charge drops below its maximum because  $V_{to} < V_{max}$ , and most of the charge transfer takes place during the rise time portion of the applied voltage pulse. The maximum in the  $Q_{relax} - V_{max}$  curve correlates with the abrupt increase of  $Q_{int}^{max}$  at  $V_{max} \approx V_{th}$ . The shape of a  $Q_{relax} - V_{max}$  curve is similar to the derivative of a  $Q_{max} - V_{max}$  curve.

### 4.3.5 Optical characteristics

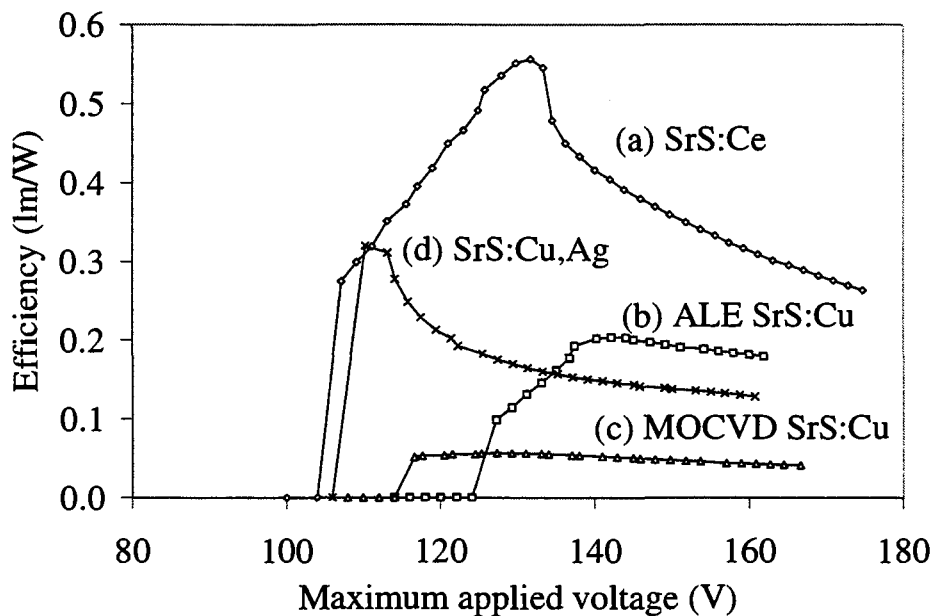
Figure 4.16 shows the ACTFEL device luminance plotted versus the maximum applied voltage ( $L - V_{max}$  plot) for four different SrS ACTFEL devices. When  $V_{max}$  is slightly smaller than  $V_{th}$ , a pre-threshold glow is typically observed. At  $V_{max} \approx V_{th}$ , the ACTFEL device luminance increases with decreasing slope as  $V_{max}$  increases. At  $V_{max} = V_{th} + 40$  V, depending on which ACTFEL device is measured, the luminance is 10 to 18 fL for the SrS:Ce ACTFEL devices, about 7 fL for the SrS:Cu ACTFEL devices obtained from Planar, 0.4 to 1.8 fL for MOCVD SrS:Cu ACTFEL devices fabricated in SUNY, and about 5 fL for the SrS:Cu,Ag ACTFEL devices (Fig. 4.16).

Figure 4.17 shows ACTFEL device luminous efficiency plotted versus the applied voltage magnitude. The luminous efficiency plots for all ACTFEL devices studied



**Figure 4.16.** Luminance versus maximum applied voltage measured using the “long”-pulse driving waveform. (a) – for a SrS:Ce ACTFEL device, (b) – for a SrS:Cu ACTFEL device from Planar, (c) – for a SrS:Cu MOCVD device from SUNY, (d) – for a SrS:Cu,Ag ACTFEL device.

here have a maximum at  $V_{max} \approx V_{th}$ . At  $V_{max} < V_{th}$ , the luminous efficiency increases with increase of  $V_{max}$  due to an increase of the pre-threshold glow. At  $V_{max} > V_{th}$ , the luminous efficiency decreases with increasing  $V_{max}$ . At  $V_{max} = V_{th} + 40$  V, depending on which ACTFEL device is measured, the luminous efficiency is 0.25 to 0.4 lm/W for the SrS:Ce ACTFEL devices, about 0.2 lm/W for the SrS:Cu ACTFEL devices obtained from Planar, 0.01 to 0.05 lm/W for the MOCVD SrS:Cu ACTFEL devices from SUNY, and 0.1-0.15 lm/W for the SrS:Cu,Ag ACTFEL devices tested (Fig. 4.17).



**Figure 4.17.** Luminous efficiency versus maximum applied voltage measured using the “long”-pulse driving waveform. (a) – for a SrS:Ce ACTFEL device, (b) – for a SrS:Cu ACTFEL device from Planar, (c) – for a SrS:Cu MOCVD device from SUNY, (d) – for a SrS:Cu,Ag ACTFEL device.

In order to compare  $L - V_{max}$ , luminous efficiency, and  $Q_{max} - V_{max}$  curves to each other, these curves are normalized and plotted in Fig. 4.18 for one of the SrS:Ce ACTFEL devices tested. Figure 4.18 shows that the shapes of the  $Q_{max} - V_{max}$  and  $L - V_{max}$  curves are similar. At  $V_{max} \ll V_{th}$ , both  $Q_{int}^{max}$  and  $L$  are zero. At  $V_{max} \approx V_{th} - 10$  V, pre-threshold glow of the ACTFEL device starts, and  $Q_{int}^{max}$  increases proportionally to the increase in luminance with increasing  $V_{max}$ . At  $V_{max} \approx V_{th}$ , both  $Q_{int}^{max}$  and luminance increase abruptly as  $V_{max}$  increases. At  $V_{max} > V_{th}$ , both  $Q_{int}^{max}$  and luminance keep increasing with increasing  $V_{max}$ . The difference between

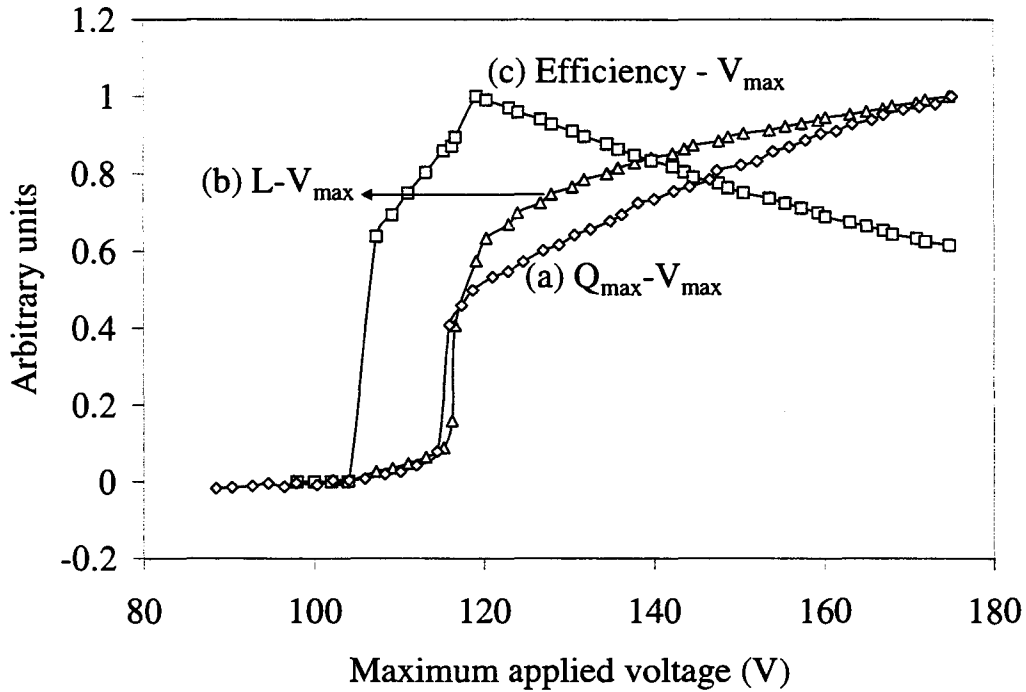


**Figure 4.18.** Normalized  $Q_{max} - V_{max}$  (a),  $L - V_{max}$  (b), and luminous efficiency (c) of a SrS:Ce ACTFEL device.

the shapes of  $Q_{max} - V_{max}$  and  $L - V_{max}$  curves is that the  $L - V_{max}$  slope decreases, while the  $Q_{max} - V_{max}$  slope changes very little as  $V_{max}$  increases above  $V_{th}$ .

Comparing luminous efficiency versus  $V_{max}$  to  $Q_{max} - V_{max}$  and  $L - V_{max}$  curves in Fig. 4.18, one notices that as the pre-threshold glow increases with increasing  $V_{max}$ , efficiency increases and reaches its maximum at  $V_{max} \approx V_{th}$ . At  $V_{max} > V_{th}$ , efficiency decreases with increasing  $V_{max}$ . These trends in  $Q_{max} - V_{max}$ ,  $L - V_{max}$ , and efficiency versus  $V_{max}$  curves are common for all ACTFEL devices tested in this work.

Figure 4.19 shows CIE coordinates measured at various  $V_{max}$ 's for all of the ACTFEL devices studied in this work. In Figure 4.19, the linear fits to the loci

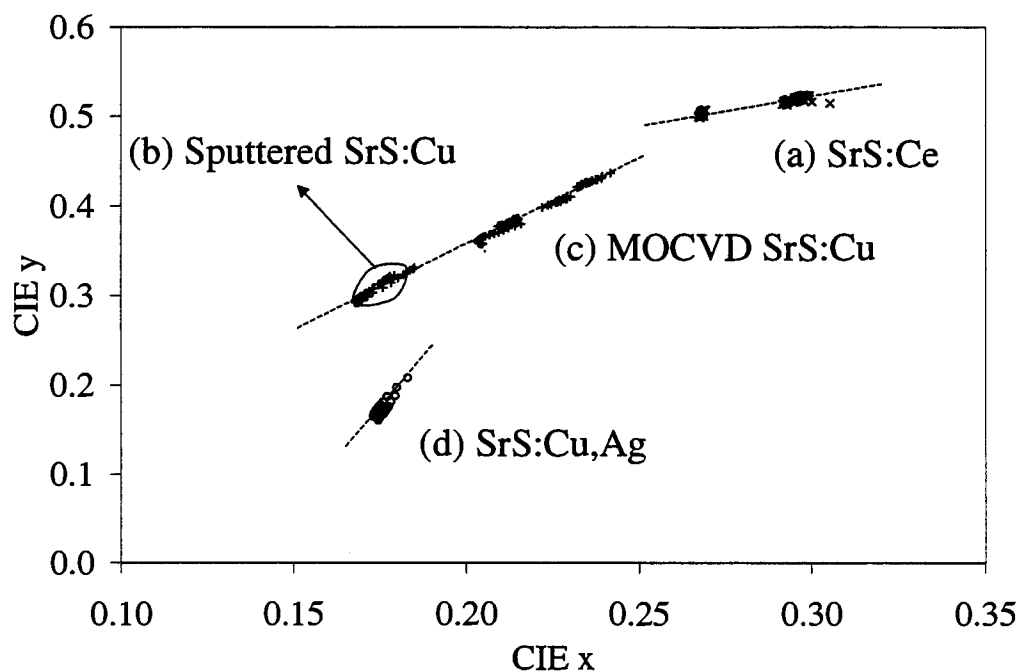


**Figure 4.19.** CIE coordinates of all of the SrS ACTFEL devices studied. (a) – for SrS:Ce ACTFEL devices, (b) – for sputtered SrS:Cu ACTFEL devices, (c) – for MOCVD SrS:Cu ACTFEL devices, (d) – for SrS:Cu,Ag ACTFEL devices.

of points corresponding to each type of ACTFEL device tested are shown with a dashed line. Within each locus, points corresponding to a single ACTFEL device form a small cluster. Each cluster corresponds to a variation of CIE coordinates of an ACTFEL device with variation of  $V_{max}$ . CIE coordinates of SrS:Cu and SrS:Cu,Ag ACTFEL devices tested decrease by  $\sim 0.01$  as  $V_{max}$  increases from  $V_{th} - 10$  V to  $V_{th} + 60$  V, which corresponds to a dominant emission wavelength variation of few nanometers. CIE coordinates of SrS:Ce ACTFEL devices are almost independent on  $V_{max}$ . The mechanism responsible for the  $V_{max}$ -dependence of the CIE coordinates

is unclear. Li [47] has shown that isolated Cu centers in SrS emit blue light while Cu centers complexed to sulfur vacancies emits green light (Sec. 2.5). This suggests that more isolated Cu centers may be emitting blue light at larger  $V_{max}$ 's.

The CIE coordinates of SrS:Ce ACTFEL devices differ somewhat from one device to another. SrS:Cu ACTFEL devices exhibit an even larger variation in CIE coordinates. The dominant SrS:Cu emission wavelength varies from  $\sim 490$  to  $\sim 510$  nm, depending on which SrS:Cu ACTFEL device is tested.

It is interesting that the loci of points obtained by plotting the CIE coordinates for ACTFEL devices of each type follow a straight line. For each type of the ACTFEL device tested, the slope of the line is different. The slope of the line decreases as the CIE color coordinate changes from blue to green.

Figure 4.19 shows that in the series of SrS:Ce – SrS:Cu – SrS:Cu,Ag ACTFEL devices tested, CIE coordinates change from green to blue.

#### 4.3.6 Summary

Table 4.8 summarizes the results of Sections 4.3.1 through 4.3.5. Table 4.8 shows that sorted by luminance and luminous efficiency from large to small, the ACTFEL devices studied form a series of (i) SrS:Ce, (ii) SrS:Cu, and (iii) SrS:Cu,Ag. In this series, the emission color changes from green to blue. One reason why the SrS:Ce ACTFEL devices appear brighter than SrS:Cu and SrS:Cu,Ag ACTFEL devices is that luminance is determined relative to human perception and a human eye is most sensitive to green light.

Table 4.8 shows that space charge-related effects, as monitored by phosphor field, capacitance, and  $\frac{dQ_{max}}{dV_{max}}$  overshoot, are observed in all of the ACTFEL devices studied. These effects are asymmetrical with respect to the applied voltage polarity. This asymmetry is especially pronounced in the SrS:Ce ACTFEL devices, where the space charge effects for the positive applied voltage pulse exceed those for the negative applied voltage pulse. This asymmetry is consistent with more space charge generation occurring near the bottom, ITO phosphor-insulator interface when electron injection occurs from here. This suggests that there is an enhanced concentration of

**Table 4.8.** SrS:Ce, SrS:Cu, and SrS:Cu,Ag ACTFEL device characteristics

	Units	SrS:Ce	SrS:Cu		SrS:Cu,Ag
			MOCVD	Sputtered	
Maximum phosphor field	MV/cm	1.3–1.5	1–1.5		0.9–1.1
Maximum internal charge	$\mu\text{C}/\text{cm}^2$	2.5–3.0	1.3–1.9		1.8–2.3
Luminance	fL	10–18	0.4–1.8	7	5
Luminous efficiency	lm/W	0.25–0.4	0.01–0.05	0.2	0.1–0.15
Phosphor field overshoot					
positive pulse	%	40	18	38	20
negative pulse	%	30	16	26	21
Maximum capacitance					
positive pulse	nF/cm <sup>2</sup>	> 100	35–65	50–65	50
negative pulse	nF/cm <sup>2</sup>	50–110	35–90	50–60	70–80
Charge collapse					
positive pulse	$\mu\text{C}/\text{cm}^2$	0.60	0		0
negative pulse	$\mu\text{C}/\text{cm}^2$	0.38	0		0
Maximum $\frac{dQ_{max}}{dV_{max}}$	nF/cm <sup>2</sup>	200–600	50–200		80
CIE $x$		0.27–0.31	0.17–0.24	0.17–0.18	0.17–0.18
CIE $y$		0.50–0.53	0.29–0.44	0.29–0.32	0.16–0.21

defects responsible for space charge creation present near the bottom, ITO phosphor-insulator interface. It is unclear whether these space charge defects are due to Ce, intrinsic defects, or impurities. Perhaps, this defect enhancement is associated with the poorer crystallinity of the first-to-grow portion of the phosphor layer.

The charge collapse observed in most of the SrS:Ce ACTFEL devices tested correlates with observed space charge-related trends. The more  $C - V$  and phosphor field overshoot observed in an ACTFEL device, the larger is the amount of charge collapse in this device observed. The amount of charge collapse observed is related to the number of electrons which reside in shallow traps or conduction band states,

which in turn depends on the amount of electron multiplication which occurs as electrons transit the phosphor.

For SrS:Ce ACTFEL devices, electrons injected from the bottom, ITO interface undergo very efficient electron multiplication, as manifest by the larger amount of  $C - V$  or  $Q_{int} - F_p$  overshoot for the positive applied voltage pulse. Because of the efficiency of this electron multiplication process, a very large number of electrons reach the top, Al phosphor-insulator interface where they first fill the deep trap states. The remaining transported electrons occupy shallow trap states or remain in the conduction band until the external voltage begins to be reduced, at which time back injection of these shallow trap or conduction band electrons manifests itself as charge collapse. Note that anomalously large  $C - V$  or  $Q_{int} - F_p$  overshoot and charge collapse are typically observed only in SrS:Ce ACTFEL devices.

In the ACTFEL devices tested, the CIE coordinates decrease as  $V_{max}$  increases from  $V_{th} - 10$  V to  $V_{th} + 60$  V. This decrease means that the dominant emission wavelength decreases with increasing  $V_{max}$ , suggesting that more centers emit blue light in these phosphors as  $V_{max}$  increases.

## Chapter 5

### CONCLUSIONS AND RECOMMENDATIONS FOR FUTURE WORK

Three main achievements are presented in this thesis. First, two new methods are developed for estimation of the insulator capacitance of ACTFEL devices possessing a large amount of dynamic space charge. Second, ACTFEL device operation is simulated using a two-sheet space charge model. Third, electro-optic characteristics of SrS:Ce, SrS:Cu, and SrS:Cu,Ag ACTFEL devices are compared.

#### 5.1 Estimation of the insulator capacitance for an ACTFEL device with dynamic space charge

Two new methods of insulator capacitance estimation of ACTFEL devices possessing large amounts of dynamic space charge are presented. Both of these insulator capacitance assessment methods employ applied voltage waveforms with long pulses (e. g. rise time, pulse width, and fall time of 200  $\mu$ s).

In the first method, the ACTFEL device insulator capacitance is calculated as a static capacitance using Eq. (4.10) at a time,  $t_0$ , when the average phosphor field,  $f_p(t_0)$ , is zero. The time  $t_0$  is assumed to correspond to the luminance transient minimum during the fall time portion of the driving waveform.

In the second method, the ACTFEL device insulator capacitance is calculated as a dynamic capacitance using Eq. (4.19), at a time interval when  $\frac{d\bar{f}_p(t)}{dt} = 0$  and the phosphor space charge spatial distribution is in steady state. It is necessary to use an applied voltage waveform with a long enough rise time to achieve the steady-state space charge distribution.

Insulator capacitance estimates obtained using the two methods are compared to physical insulator capacitance estimates obtained from the ACTFEL device manufacturer for several ACTFEL devices. The accuracy of these  $C_i$  estimation methods appears to be similar and both techniques appear to be more reliable when more charge is transported across the phosphor.

## 5.2 Simulation of electrical characteristics of SrS:Ce ACTFEL devices using a two-sheet space charge model

SrS:Ce ACTFEL device  $C - V$  and  $Q_{int} - F_p$  characteristics are simulated using a two-sheet space charge model. [2]

The two-sheet space charge model allows for realistic simulation of  $Q_{int} - F_p$  curves of SrS:Ce ACTFEL devices with accurate values of maximum internal charge, leakage charge, relaxation charge, and phosphor field at the end of the rise time portion of the driving waveform. However, since the present two-sheet space charge model employs field-assisted emission as the only mechanism of electron injection into the phosphor conduction band, it fails to explain the large experimentally observed phosphor field overshoot, turn-on voltage, and capacitance overshoot in SrS:Ce ACTFEL devices. Using a DOE methodology, it is shown that the values of maximum internal charge, turn-on phosphor field, and steady-state phosphor field obtained by the two-sheet space charge model simulation all depend primarily on the space charge parameters — bulk trap depth and capture cross-section. The screening DOE procedure confirms conclusions obtained from the single-sheet space charge model [54], that the dynamic space charge is responsible for the capacitance overshoot observed experimentally in SrS-based ACTFEL devices and that the capacitance overshoot is larger when most of the space charge is created near the phosphor-insulator interfaces.

More work is required to employ band-to-band impact excitation with hole trapping and trap-to-band impact ionization as space charge creation mechanisms in the

two-sheet space charge model to simulate the large dynamic space charge witnessed in SrS-based ACTFEL devices.

### 5.3 Electro-optical characterization of SrS:Ce, SrS:Cu, and SrS:Cu, Ag ACTFEL devices

Electro-optical characteristics of SrS:Ce, SrS:Cu, and SrS:Cu,Ag ACTFEL devices are studied and compared to each other. Sorted by luminance and luminous efficiency from large to small, the ACTFEL devices studied form a series of (i) SrS:Ce, (ii) SrS:Cu, and (iii) SrS:Cu,Ag. In this series, the emission color changes from green to blue.

Space charge-related effects, as monitored by phosphor field, capacitance, and  $\frac{dQ_{max}}{dV_{max}}$  overshoot, are observed in all of the ACTFEL devices studied. These effects are asymmetrical with respect to the applied voltage polarity. This asymmetry is especially pronounced in the SrS:Ce ACTFEL devices, where space charge effects for the positive applied voltage pulse exceed those for the negative applied voltage pulse. This asymmetry is consistent with more space charge generation occurring near the bottom, ITO phosphor-insulator interface when electron injection occurs from here. This suggests that there is an enhanced concentration of defects responsible for space charge creation present near the bottom, ITO phosphor-insulator interface. More work is required to establish the reason for this asymmetry between the two phosphor-insulator interfaces.

The charge collapse observed in most of the SrS:Ce ACTFEL devices tested correlates with observed space charge-related trends. The more  $C - V$  and phosphor field overshoot observed in an ACTFEL device, the larger is the amount of charge collapse observed. Anomalously large  $C - V$  or  $Q_{int} - F_p$  overshoot and charge collapse are typically observed only in SrS:Ce ACTFEL devices. The nature of the charge collapse is still unclear and is suggested as a topic for future research.

The space charge creation mechanism is unclear in SrS:Ce, SrS:Cu, and SrS:Cu, Ag ACTFEL devices. This mechanism may be different in SrS:Ce and SrS:Cu/

SrS:Cu,Ag ACTFEL devices because of the donor-like nature of Ce and the acceptor-like nature of Cu/Ag. Since the two-sheet space charge model, employing field-assisted electron emission from traps as the space charge generation mechanism, could not account for the large dynamic space charge witnessed in SrS:Ce ACTFEL devices, field-assisted emission can be eliminated as the operative space charge generation mechanism. This leaves band-to-band impact excitation with hole trapping and trap-to-band impact ionization as possible space charge generation mechanisms. More work is required to determine which of these mechanisms is applicable to SrS:Ce, SrS:Cu, and SrS:Cu,Ag ACTFEL operation.

In the ACTFEL devices tested, the CIE coordinates decrease as  $V_{max}$  increases from  $V_{th} - 10$  V to  $V_{th} + 60$  V. This decrease means that the dominant emission wavelength decreases with increasing  $V_{max}$ , suggesting that more centers emit blue light in these phosphors as  $V_{max}$  increases. More work is required to understand the nature of this emission wavelength dependence on  $V_{max}$ .

## BIBLIOGRAPHY

- [1] N. Yamashita, "Photoluminescence properties of  $\text{Cu}^+$  centers in MgS, CaS, SrS and BrS," *Jpn. J. Appl. Phys.*, vol. 30, pp. 3335–3850, Dec. 1991.
- [2] P. D. Keir, "Modeling phosphor space charge in alternating-current thin-film electroluminescent devices," Master's thesis, Oregon State University, Aug. 1995.
- [3] J. A. Castellano, "Flat Panel Impact on CRT Monitor Markets," *Solid State Technology*, vol. 41, pp. 67–70, Jan. 1998.
- [4] M. J. Russ, D. I. Kennedy, "The Effect of Double Insulating Layers on the Electroluminescence of Evaporated ZnS:Mn Films," *J. Electrochem. Soc.*, vol. 114, p. 1066, 1967.
- [5] T. Inoguchi, M. Takeda, Y. Kakiyama, M. Yoshida, "Stable High Luminance Thin-Film Electroluminescent Panels," *Digest of the 1974 SID Int'l Display Symposium*, p. 86, 1974.
- [6] W. A. Barrow, R. E. Coover, and C. N. King, "Strontium Sulfide: The Host for a New High Efficiency Thin Film EL Blue Phosphor," *Digest of the 1984 SID Int'l Display Symposium*, p. 249, 1984.
- [7] W. Lehmann, "Alkaline earth sulfide phosphors activated by copper, silver, and gold," *J. Electrochem. Soc.*, vol. 117, p. 1389, Nov. 1970.
- [8] G. Destriau, "Reserches sur les Scintillations des Zinc aux Rayons," *J. de Chime Physique*, vol. 33, pp. 587–625, 1936.
- [9] J. F. Wager, P. D. Keir, "Electrical Characterization of Thin-Film Electroluminescent Devices," in *Annu. Rev. Mater. Sci.*, vol. 27, pp. 223–248, 1997.
- [10] Y. A. Ono, "Electroluminescence," in *Encyclopedia of Applied Physics*, pp. 295–325, VCH Publishers, Inc., 1993.

- [11] K.-W. C. Yang and S. J. T. Owen, "Mechanisms of the negative-resistance characteristics in ac thin-film electroluminescent devices," *IEEE Trans. Electron Devices*, vol. ED-30, pp. 452–459, May 1983.
- [12] D. H. Smith, "Modeling a.c. thin-film electroluminescent devices," *J. Lumin.*, vol. 23, pp. 209–235, 1981.
- [13] W. E. Howard, "Memory in thin-film electroluminescent devices," *J. Lumin.*, vol. 23, pp. 155–173, 1981.
- [14] K. A. Neyts, D. Corlatan, P. De Visschere, and J. Van den Bossche, "Observation and simulation of space-charge effects and hysteresis in ZnS:Mn ac thin-film electroluminescent," *J. Appl. Phys.*, vol. 75, pp. 5339–5346, May 1994.
- [15] A. Abu-Dayah, J. F. Wager, and S. Kobayashi, "Electrical characterization of atomic layer epitaxy ZnS:Mn alternating-current thin-film electroluminescent devices subject to various waveforms," *J. Appl. Phys.*, vol. 74, pp. 5575–5581, Nov. 1993.
- [16] A. Abu-Dayah, S. Kobayashi, and J. F. Wager, "Internal charge – phosphor field characteristics of alternating-current thin-film electroluminescent devices," *Appl. Phys. Lett.*, vol. 62, pp. 744–746, Feb. 1993.
- [17] A. Abu-Dayah and J. F. Wager, "Aging studies of atomic layer epitaxy ZnS:Mn alternating-current thin-film electroluminescent devices," *J. Appl. Phys.*, vol. 75, pp. 3593–3598, Apr. 1994.
- [18] K. A. Neyts, "Simple model for the hysteretic behavior of thin-film electroluminescent devices," *IEEE Trans. Electron Devices*, vol. 38, pp. 2604–2611, Dec. 1991.
- [19] A. A. Douglas, J. F. Wager, D. C. Morton, J. B. Koh, and C. P. Hogh, "Evidence for space charge in atomic layer epitaxy ZnS:Mn alternating-current thin-film electroluminescent devices," *J. Appl. Phys.*, vol. 73, pp. 296–299, Jan. 1993.
- [20] E. Bringuier, "Electron multiplication in ZnS-type electroluminescent devices," *J. Appl. Phys.*, vol. 67, pp. 7040–7044, June 1990.
- [21] W. M. Ang, S. Pennathur, L. Pham, J. F. Wager, and S. M. Goodnick, "Evidence for band-to-band impact ionization in evaporated ZnS:Mn alternating-current thin-film electroluminescent devices," *J. Appl. Phys.*, vol. 77, pp. 2719–2724, Mar. 1995.

- [22] B. K. Ridley and F. A. El-Ela, "Space-charge anomalies in insulators caused by non-local impact ionisation," *J. Phys.: Condens. Matter*, vol. 1, pp. 7021–7031, 1989.
- [23] A. Goldenblum, A. Oprea, and V. Bogatu, "Time behavior of currents in ZnS:Mn metal - insulator - semiconductor - insulator - metal structures," *J. App. Phys.*, vol. 75, pp. 5177–5185, May 1994.
- [24] S. P. Keller, J. E. Mapes, and G. Cheroff, "Studies on some infrared stimuable phosphors," *Physical Review*, vol. 108, pp. 663–667, Nov. 1957.
- [25] D. A. Buchanan, M. V. Fischetti, and D. J. DiMaria, "Coulombic and neutral trapping centers in silicon dioxide," *Phys. Rev. B*, vol. 43, pp. 1471–1486, Jan. 1991.
- [26] P. K. Ghosh and B. Ray, "Luminescence in alkaline earth sulfides," *Prog. Crystal Growth and Characterization*, vol. 25, pp. 1–37, 1992.
- [27] Y. Kaneko and T. Koda, "New developments in iia–vib (alkaline-earth chalcogenide) binary semiconductors," *J. Crystal Growth*, vol. 86, pp. 72–78, 1988.
- [28] A. Hasegawa and A. Yanase, "Electronic structure of Sr monohalcogenides," *J. Phys. C: Solid State Phys.*, vol. 13, pp. 1995–1999, 1980.
- [29] R. Pandey, J. E. Jaffe, and A. B. Kunz, "Ab initio band-structure calculations for alkaline-earth oxides and sulfides," *Phys. Rev. B*, vol. 43, pp. 9228–9237, Apr. 1991.
- [30] M. Dür, M. Saraniti, and S. M. Goodnick, "First principles modeling of electronic transport in wide bandgap phosphor materials," in *Extended abstracts. The fourth international conference on science and technology of display phosphors*, (Bend, Oregon), pp. 207–210, Sep. 1998.
- [31] J. Rennie, E. Nakazawa, and T. Koda, "Trapping states in CaS and SrS single crystals, films, and powders as revealed using the technique of transient thermoluminescence," *Jpn. J. Appl. Phys.*, vol. 29, pp. 509–515, Mar. 1990.
- [32] B. Hüttl, U. Troppenz, K. O. Velthaus, C. R. Ronda, and R. H. Mauch, "Luminescence properties of SrS:Ce<sup>3+</sup>," *J. Appl. Phys.*, vol. 78, pp. 7282–7288, Dec. 1995.

- [33] W. L. Warren, K. Vanheusden, C. H. Seager, D. R. Tallant, J. A. Tuchman, S. D. Silliman, and D. T. Brower, "Local Ce environments and their effect on optical properties of SrS phosphors," *J. Appl. Phys.*, vol. 80, pp. 7036–7040, Dec. 1996.
- [34] W. L. Warren, C. H. Seager, S.-S. Sun, A. Naman, P. H. Holloway, K. S. Jones, and E. Soininen, "Microstructure and atomic effects on the electroluminescent efficiency of SrS:Ce thin film devices," *J. Appl. Phys.*, vol. 82, pp. 5138–5143, Nov. 1997.
- [35] W. L. Warren, K. Vanheusden, D. R. Tallant, C. H. Seager, S.-S. Sun, D. R. Evans, W. M. Dennis, E. Soininen, and J. A. Bullington, "Atomic level stress and light emission in Ce activated SrS thin films," *J. Appl. Phys.*, vol. 82, pp. 1812–1814, Aug. 1997.
- [36] K. Ohmi, S. Inoue, S. Tanaka, and H. Kobayashi, "Relaxation of phosphor field in SrS:Ce thin film electroluminescent devices," *Appl. Phys. Lett.*, vol. 64, pp. 3464–3466, Jun. 1994.
- [37] K. Ohmi, K. Ishitani, S. Tanaka, and H. Kobayashi, "Role of space charge in SrS:Ce thin film electroluminescent devices studied by the photoirradiation effect," *Appl. Phys. Lett.*, vol. 67, pp. 944–946, Aug. 1995.
- [38] K. Ohmi, K. I. Y. Kashio, S. Tanaka, and H. Kobayashi, "Characterization of the electrical properties of SrS:Ce thin-film electroluminescent devices," *Journal of the SID*, vol. 5/2, pp. 145–149, 1997.
- [39] K. Neyts and E. Soininen, "Space charge and light generation in SrS:Ce thin film electroluminescent devices," *IEEE Transactions on Electron Devices*, vol. 42, pp. 1086–1092, Jun. 1995.
- [40] S. Tanaka, H. Yoshiyama, Y. Mikami, J. Nishiura, S. Ohshio, and H. Kobayashi, "Excitation mechanism in red CaS:Eu and blue SrS:Ce,K TFEL films," *Proceedings of the SID*, vol. 29/1, pp. 77–81, 1988.
- [41] M. Peter, Y. Kashio, S. Nishimura, K. Ohmi, S. Tanaka, and H. Kobayashi, "Study of dynamic space charge in SrS:Ce thin-film electroluminescent devices by tunable laser excitation," in *Extended abstracts. The third international conference on the science and technology of display phosphors*, (Huntington Beach, California), pp. 61–64, Nov. 1997.

- [42] V. Singh and D. C. Morton, "Mechanism of electroluminescence in alkaline-earth sulfide actfel devices," *SID 88 Digest*, pp. 27–30, 1988.
- [43] V. P. Singh and D. C. Morton, "Luminescence response of SrS:CeF<sub>3</sub> ACTFEL devices to various pulse waveforms," *IEEE Trans. Electron Devices*, vol. 36, pp. 54–61, Jan. 1989.
- [44] J. Kane, W. Harty, M. Ling, and P. N. Yocom in *SID'85 Digest*, p. 163, 1985.
- [45] S.-S. Sun, E. Dickey, J. Kane, and P. Yocom in *Conference record '97 IDRC*, p. 301, 1997.
- [46] N. Yamashita, K. Ebisumori, and K. Nakamura, "Luminescence from aggregated Cu<sup>+</sup> centers in SrS:Cu<sup>+</sup>," *Jpn. J. Appl. Phys.*, vol. 32, pp. 3846–3849, Sep. 1993.
- [47] D. Li, *Phosphor development: synthesis, characterization and chromatic control*. PhD thesis, Oregon State University, Jun. 1999.
- [48] H. W. Etzel and J. H. Schulman, "Silver-activated alkali halides," *J. Chem. Phys.*, vol. 22, pp. 1549–1554, Sep. 1954.
- [49] B. Atoussi, C. Pedrini, B. Moine, and C. Madej, "Spectroscopic investigation and polarized luminescence of silver pair centers in sodium chloride," *Physica Status Solidi (b)*, vol. 128, pp. 683–692, 1985.
- [50] S.-S. Sun, "Blue emitting SrS:Ag,Cu TFEL devices," in *Extended abstracts of the fourth international conference on the science and technology of display phosphors*, (Bend, Oregon), pp. 183–186, Sep. 1998.
- [51] U. Troppenz, B. Hüttl, U. Storz, P. Kratzert, and K.-O. Velthaus, "Photoluminescence and electroluminescence studies on Cu and Ag doped SrS ACTFEL devices," in *Extended abstracts of the fourth international conference on the science and technology of display phosphors*, (Bend, Oregon), pp. 187–190, Sep. 1998.
- [52] W. Park, T. C. Jones, E. Mohammed, and C. J. Summers, "Luminescence properties of SrS:Cu,Ag thin film electroluminescent phosphors," in *Extended abstracts of the fourth international conference on the science and technology of display phosphors*, (Bend, Oregon), pp. 215–218, Sep. 1998.

- [53] Z. L. Denisova, Y. F. Kononets, L. I. Veligura, and N. A. Vlasenko, "New data concerning luminescence mechanism in SrS:Cu(Ag,Ga) TFEL devices," in *Extended abstracts of the fourth international conference on the science and technology of display phosphors*, (Bend, Oregon), pp. 247–250, Sep. 1998.
- [54] P. D. Keir, W. M. Ang, and J. F. Wager, "Modeling space charge in alternating-current thin-film electroluminescent devices using a single-sheet space charge model," *J. Appl. Phys.*, vol. 78, pp. 4668–4680, Oct 1995.
- [55] G. Vincent, A. Chantre, and D. Bois, "Electric field effect on the thermal emission of traps in semiconductor junctions," *J. Appl. Phys.*, vol. 50, pp. 5484–5487, Aug. 1979.
- [56] E. Rosencher, V. Mosser, and G. Vincent, "Transient-current study of field-assisted emission from shallow levels in silicon," *Phys. Rev. B*, vol. 29, pp. 1135–1147, Feb. 1984.
- [57] E. Bringuier, "Charge transfer in ZnS-type electroluminescence," *J. Appl. Phys.*, vol. 66, pp. 1314–1325, Aug. 1989.
- [58] C. B. Sawyer and C. H. Tower, "Rochelle salt as a dielectric," *Phys. Rev.*, vol. 35, pp. 269–273, Feb. 1930.
- [59] J. C. Hitt, "Static space charge in evaporated ZnS:Mn alternating-current thin-film electroluminescent devices," Master's thesis, Oregon State University, Jun. 1998.
- [60] D. C. Montgomery, *Introduction to statistical quality control*. John Wiley and Sons, Inc., 3rd ed., 1996.
- [61] R. L. Thuemler, "Characterization of alternating-current thin-film SrS:Ce electroluminescent devices," Master's thesis, Oregon State University, June 1998.